EMC Analysis of Electric Drives

Fadi Abdallah

LUND
UNIVERSITY

Licentiate Dissertation
Department of Measurement Technology and
Industrial Electrical Engineering

2012

Department of Measurement Technology and Industrial Electrical Engineering
Faculty of Engineering
Lund University
Box 118
221 00 LUND
SWEDEN

http://www.iea.lth.se

ISBN:978-91-88934-57-4
CODEN: LUTEDX/(TEIE-1065)/1-120/(2012)

Printed in Sweden by Tryckeriet i E-huset, Lund University
Lund 2012

To the purest, to the kindest and to the most wonderful human being I got to know..

To my mother

Abstract

In order to study conducted ElectroMagnetic Interference (EMI) emissions along a frequency band, circuit models of main components in the drive system are considered to be effective means to understand, predict, and control the phenomenon. These models should cover the capacitive and inductive coupling behaviour of the component along the frequency band of interest. Despite the dynamic behaviour of EMC-related issues, these detailed circuit models when used under generic SPICE simulation softwares, are very helpful for design-related and troubleshooting activities.

In this thesis the capacitive and inductive coupling for a winding on a laminated ferro-magnetic core prototype has been investigated and analysed with the aid of FEMM software package.

Capacitive coupling analysis resulted in the generation of complex capacitance network expressing a certain wiring arrangement. This is achieved by automatically generating a netlist file which contains capacitance values and structure to be represented under SPICE simulation software. In the netlist file the turn-to-turn capacitances (C_{tt}) and turn-to-ground capacitances (C_{tg}) are calculated from FEMM analysis through a MATLAB® code and linked back to MATLAB® by a Sparse Matrix Representation in order to control the accuracy and complexity of the resulting network.

Inductive coupling analysis has led to the proposal of a SPICE circuit model for a single turn of copper winding on iron core. This has been accomplished by the quantification of the magnetic analysis output from FEMM, creating zero-pole-gain models and transfer functions of the SPICE model components, and then making use of the pole-zero maps and Bode plots utilities under MATLAB® to analytically propose compensation factors for the complete SPICE circuit model components of a single copper turn, in order to fulfill low- and high- frequency behaviour.

Given the capacitive and inductive coupling of the winding turns, the resulting SPICE circuit model output is compared against measurements of the prototype taken by Hewlett Packard (hp) impedance analyzer 4194A where it showed very good agreement.

Acknowledgements

First and Foremost I would like to express my sincere thanks and gratitude to my supervisor Professor Mats Alaküla for giving me this opportunity and for making this thesis work possible. Mats has always been a source of inspiration and guidance to me. His brilliant ability of actualizing concepts and ideas into functional systems is something one can always be proud of and thrive for. I have indeed been privileged to be within Mats domain.

My thanks go to my co-supervisor Dr. Hans Bängtsson for the hours of supervision he devoted for me during his regular visits to IEA in order to review, assess and provide relevant feedback to my work. Thanks are also due to Dr. Avo Reinap for introducing me to the world of FEM simulation, for the time and effort he has given me despite his tight schedule usually. Without Avo's key insights, the magnetic modeling part of this thesis would not have been realized.

Special thanks go to my predecessor and mentor in the EMC field, Dr. Sabine Alexandersson. Sabine was my mentor when I started my research at IEA. She shared with me the cream of her experience and pointed me to key areas in the field including very helpful resources and references, and many software and hardware tools. Sabine helped me form my reference group. Sabine has been involved in my project since the start and been supportive all the way through by her follow ups, suggestions, regular visits and phone calls.

Dr. Per Karlsson is a key person in my research project, not least during his visits to IEA as a consultant. Per introduced me to the world of Power Electronics with both theory and applications in mind. Per's unique style of supervision made me realize the potential I have in order to search for the information, build up knowledge and make things happen in reality.

My reference group members represented by Jan Welinder (SP Technical Research Institute of Sweden), Kjell Attback and Håkan Berg (Volvo Cars Corporation), and Johan Nilsson (Electrical Measurement Department) have influenced the development of this work, not least the suggestion of building up the simple winding on core prototype by Jan Welinder. They did not hesitate in sharing their knowledge and experience with me which always added stimulus and momentum to the work, as well gave the chance for a broad scrutiny and feedback. Particularly Jan and Kjell; the time and effort you've devoted outside our meeting hours are deeply appreciated!

A special "Thank you!" goes to Lars Lindgren for his interest and engage-

ment in what I'm doing, for the time and effort he devoted to review my work, and for the valuable suggestions and tips he provided. Getachew Darge deserves a big and special "Thank you!" for all the help, time and effort he provided in the laboratory. Getachew's technical experience and problem-solving abilities are well acknowledged.

As well the effective organization and management of our department, represented by Dr. Ulf Jeppsson and the rest of the team, deserve an acknowledgement for keeping things in order and making everything smooth for us in order to focus on our research and teaching duties, not to mention the thoughtful gestures they always have in mind when it comes to private or public occasions.

Special thanks go to each and everyone of my colleagues and friends at IEA especially my roommates Yury Loayza (Abu Vincent) and Dan Hagstedt (Abu Oline) for making the work place a fun place to be at and for all the good and enjoyable time we had inside and outside the school.

I'm also indebted to all of my friends outside the academic world for reminding me of the enjoyable part of life outside the work domain and for helping me keep the balance. Many names should be mentioned here but I choose not to in case I forget any of you! My neighbours in Sakförarevägen-Lund are also included. I owe you all lots of thanks and appreciation, and because of you life can have a special and sweet taste.

Last but not least my family deserves the biggest thanks and credits for their sacrifice, patience and understanding. I wish I could trade all what I have with couple of days in my mother's life! My mother Nawal, who passed away while I was doing this project, my father Wajeeh and my brother Morsi have given me lots of support and encouragement. With all the love and appreciation to my family I end these lines.

Fadi Abdallah

P.S. This work is part of the *Integrated Charger* project which is funded by the Swedish Hybrid Vehicle Centre (SHC) under the thematic area Electrical Machines and Drives. This financial support is gratefully acknowledged.

Contents

List of Figures

List of Tables

Chapter 1

Introduction

1.1 Background

Introducing electric propulsion in a large scale to the automotive industry through hybrid and electrical vehicles, in addition to the associated development of charging techniques, creates a unique and challenging situation that was not a norm before. The relatively high-power electric drives on board along with already established small-power electrical loads make the co-existence between systems and components in the vehicle environment more challenging.

The switching process of semiconductor elements in high-power (10's of kiloWatts) electric drives and at relatively high frequency rates (few kHz of switching frequency), involve high voltage- and high current-derivatives. For example, semiconductor elements switching at 4 kHz in a 30 kW electric drive system which is supplied from a floating Energy Storage System (ESS) of 300 volts can produce a voltage derivative ($\frac{du}{dt}$) of more than a billion (10^9) [V/s], and a comparable current derivative ($\frac{di}{dt}$) in the order of 10^9 [A/s], a fact that can result in conducted and radiated emissions. The confined space and the surrounding magnetic/electrical media will make intervention between different systems/sub-systems/components easier and will place more challenges on an electromagnetically compatible vehicular system.

The importance of the ElectroMagnetic Compatibility (EMC) field in the

automotive industry comes from many key contributors among which are:

i. The pressing need and public awareness to cheaper, cleaner and more efficient mobility solutions which can be achieved through electrical propulsion,

ii. The nature of high-scale production in the automotive industry,

iii. The importance of modular design [2], and

iv. The desirable minimum development time with minimum design iterations [4][5].

Traditionally EMC optimization comes as a later stage after the functional and safe design in a way that will not compromise any, but being able to predict the EMC behavior of the system at an early stage will only contribute positively to the development time and hence productivity and cost.

Another interesting fact to mention is that there are no clear and definitive EMC standards developed for the individual electrical components used in building up the powertrain in a hybrid or electrical vehicle, despite the fact that standards exist for the vehicle as a whole unit [6]. This reflects the broadness and freedom in fulfilling EMC-related standards, but at the same time distinguishes between manufacturers interested in "getting under the skin" of EMC challenges in order to fulfill the standards, and those interested in quick-fix solutions.

1.2 Problem Formulation

Conducted and radiated ElectroMagnetic Interference (EMI) emissions is the downside of power electronics systems development towards increasing power density and decreasing size and losses. Unlike three phase grid power-supplied machines, Pulse-Width Modulation (PWM)-Inverter-Fed machines inherently result in Common-Mode (CM) voltage on the connection point of the machine phase windings, which has a value at any point in time as shown in figure 1.3 [25][32][3][28][1][26].

On the other hand, parasitic capacitances-to-ground exist literally all over the electric drive system [18][19], as shown in figure 1.1 and 1.2, starting from the battery pack's (ESS) positive and negative poles to ground, passing through power cables, each end of dc-link capacitor or line Differential-Mode (DM) filters

to ground, each junction module of switching elements to ground, and ending up in the electric machine parasitics to ground.

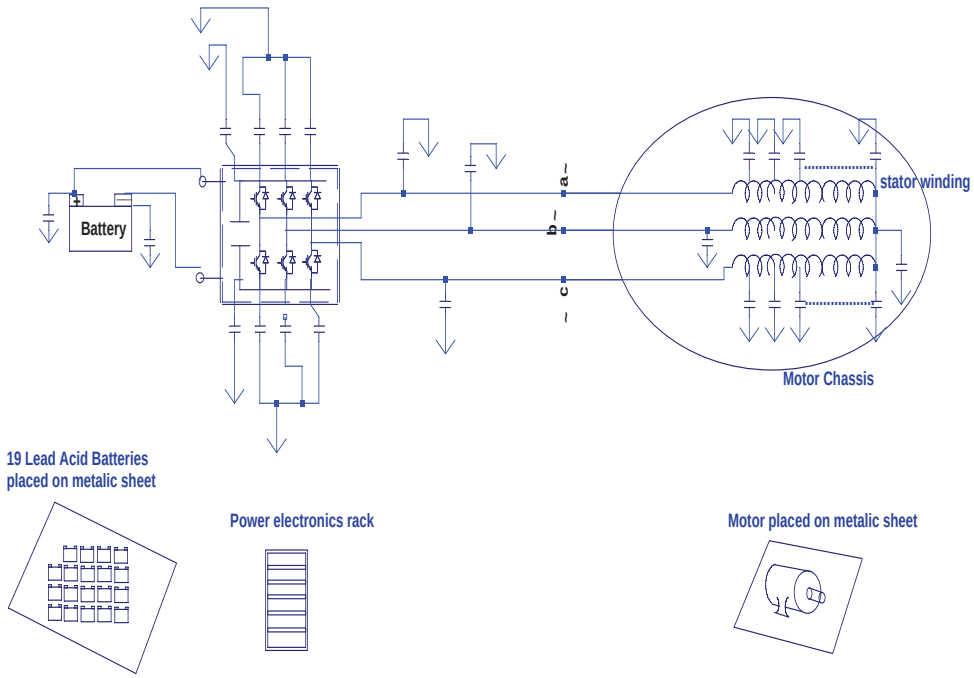

Figure 1.1: Parasitic capacitances in an electric drive system

Parasitic capacitances are usually of low orders of magnitude which make them negligible at low frequency analysis. Investigation out of the inhouse built electric drive labsetup showed a range from 100's of pico (p) Farads (Fs) up to few nano (n) Fs. However, with the development of Insulated Gate Bipolar Transistor (IGBT) technology and the increase of switching frequency and rated power, not least with Silicon Carbide (SiC)-based technology, these capacitances interact with the high-frequency CM voltage waveform and can provide a low-impedance path for the leakage current. Capacitive impedance path depends on the combination of capacitance value and CM voltage frequency. The high-frequency leakage current takes the the form of a damped sinusoid [28],

Figure 1.2: A photo of the second inhouse-built electric drive labsetup

at every instant a change in the varying 2-step/3-step CM voltage waveform occurs, which is estimated to be 4-6 times the carrier wave or CM voltage waveform frequency, as shown in figures 1.3 and 1.4, assuming carrier wave based modulation.

Depending on the machine type and size the parasitic capacitances of the machine can vary [8][13][9][27][22], but common and fundamental capacitances among all machines are capacitances among winding copper conductors in a stator slot, and capacitances between winding copper conductors in the slot and stator frame. Induction machines can have additional parasitic capacitances due to their construction [1].

The manifestation of this problem can take different forms among which many are allready spread in the industry. Examples are:

(a). Frequent Earth Leakage Protection (ELP) trip faults when connecting floating ESS powered electric drive to the power grid for charging.

(b). Electric Discharge Machining (EDM) currents causing premature motor bearings failure or what is known to the industry as bearing currents.

(c). Gradual degradation and breakdown of copper conductors' insulation within the first few turns of a machine stator winding.

Since many factors contribute to this phenomenon, many mitigation techniques can be used to control the problem, as summarized in [1]. They tend to be reactive measures and not proactive ones taken at an early stage.

1.3 Scope and Goal

The scope of this research project focuses on analysis and simulation of electric drive systems from an EMC perspective, in order to limit the conducted EMI emissions observed at high frequencies up to 30 MHz [15][33].

The ultimate goal of this work is to contribute to a detailed CM-model of an electric machine that is valid from dc up to 30 MHz, and can be used in a circuit simulation environment in order to predict high-frequency CM current. The Current at high frequencies can use parasitic capacitances to ground, which exist all over the electric drive system, as low-impedance paths to ground and back to its source in the power electronics converter.

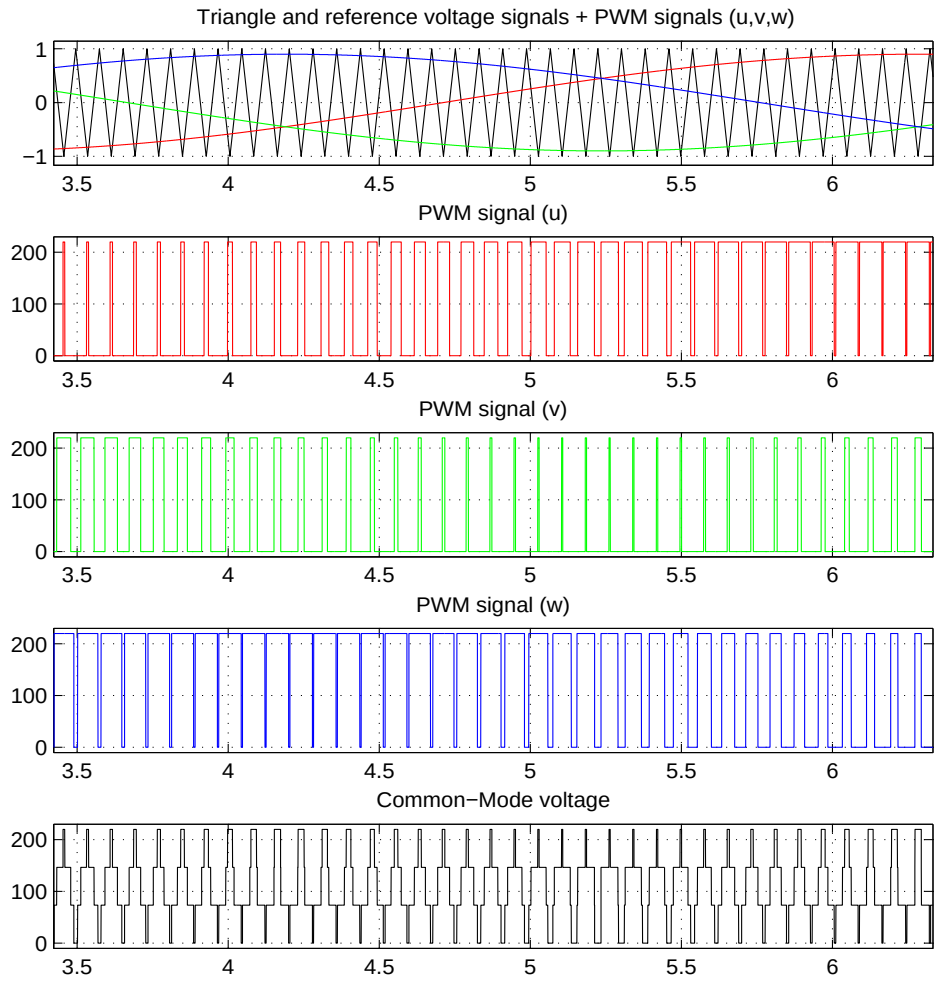

Figure 1.3: Triangular wave and reference voltages, generated PWM signals and a varying 2-step/3-step CM voltage waveform

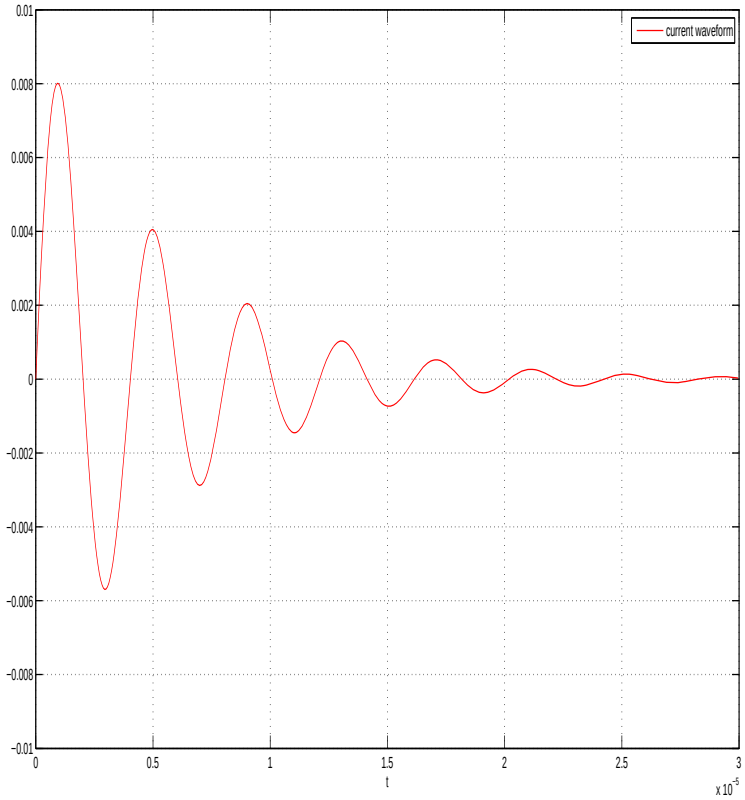

Figure 1.4: The resulting high-frequency damped-sinusoid CM current waveform occuring at each CM voltage step

The study aims at investigating capacitive and inductive coupling of a machine winding in order to characterize the high frequency behavior of the machine. The outcome of this study and the methodology adopted will represent an input to the slot level analysis of electrical machines along the frequency sweep of interest.

The developed knowledge and recommendations is expected to add value when integrated in a full-scale electric machine design environment which will enable the machine designer, at an early stage of the design, to predict and influence stray capacitances of the machine.

Defining the scope of this project should not be confused with the basic criteria about EMC behavior for any electric drive system, that is; EMC is a very dynamic field and EMC optimization is a system-based attribute in which any part of the system can contribute to its compatibility. By "attribute" one means the feature that cannot be tangibly sensed by the user, however it is necessary for safe and compliant functionality [6].

1.4 Study Roadmap and Thesis Structure

The study starts by investigating a heavy vehicle electrical system which includes a motor drive with an inverter connected to a floating ESS through a junction box. The system is studied and model drafts are developed in an LTspice simulation software. The target is to develop a detailed and comprehensive model of the electrical system in a "Simulation Program with Integrated Circuit Emphasis" (SPICE) environment where conducted emissions can be viewed and studied through "what if" scenarios.

Due to ease of access and in order to perform research-oriented activities, an experimental electrical system that mimics the above mentioned is built inhouse. Two laboration setups are made. They included two induction machines (1.5 kW & 2.2 kW), a power electronics converter (43 kW), a shielded power cable and a metalic sheet as a ground plane. In the first lab setup, the floating ESS is emulated by the direct connection to the power grid and then passing through a galvanic isolation stage of a 3-phase power transformer with a ratio primary-to-secondary of 1:1, and then amplitude variation stage by another 3-phase variable transformer and finally, rectification and filtering stage using 3-phase bridge rectifier and a parallel capacitor. In the second lab setup, the ESS is

built from 19 lead-acid battery cells, each rated at 12V, 20 Ah corresponding to ≈ 4.4 kWh.

The investigation reveals that low-order of magnitude capacitances existing between winding turns and between turns and stator frame in the electrical machine winding, are key elements in the analysis of high frequency current paths in the whole system, therefore lots of effort and attention is given to develop a detailed model of the machine winding including parasitic capacitances which covers a wide frequency band considering the complete conducted emission frequency range up to 30 MHz as per [15].

For that purpose, an induction machine of 1.5 kW is opened up and studied extensively, and a prototype of a winding-on-core model composed of 24 turns/3 layers (8 turns in each layer) in distanced and condensed arrangements, is built and investigated to study the turn-to-turn capacitance, layer-to-layer capacitance and the iron core impact on the inductance in high frequency. An impedance analyzer Hewlett Packard (hp) 4194A from the Electrical Measurement Department (Elmät) is used (and thankfully acknowledged) to perform tests and measurements for the required frequency range.

The study is supported by a steering group of professionals from the academia and industry. Besides my supervisor Professor Mats Alaküla and my co-supervisors Dr. Avo Reinap and Dr. Hans Bängtsson, the group consists of: Jan Welinder from SP Technical Research Institute of Sweden, Dr. Per Karlsson from Emotron then and currently an Associate Professor at IEA-Helsingborg Campus, Håkan Berg and Kjell Attback from Volvo Cars Corporation (VCC), Dr. Johan Nilsson from Electrical Measurement Department, Dr. Sabine Alexandersson and Jan-Olof Brink from Kockums. Their guidance, support and feedback are highly appreciated and have had a significant impact on the development of this project.

The Thesis structure proceeds as follows:

- Chapter 2: Analysis Tools.
- Chapter 3: Capacitive Coupling Matrix.
- Chapter 4: Inductive Coupling Matrix.
- Chapter 5: Model Validation.
- Chapter 6: Conclusions and Future work.

1.5 Contribution of This Study

This study offers knowledge and tools targeting electrical machine designers, personnel working in electrical system integration, and those fulfilling EMC requirements through:

- Highlighting the capacitive and inductive coupling paths which the CM current takes throughout its way back to the converter, and representing them in a circuit simulation software. The perspective is enhancing immunity of electrical machines against conducted EMI emissions.
- Generating a capacitance network with pre-determined accuracy (complexity) levels, for the turn-to-turn copper conductors of a winding-on-core. This helps understand and establish parasitic capacitance network for a winding inside a slot in electrical machines. Parasitic capacitances in electrical machines are viewed as major coupling paths that impact leakage current in motor drive systems of PWM input.
- Using freely available software tools, like FEMM and LTspice®, to quickly but accurately predict capacitive and inductive coupling in electrical machines, and the resulting high-frequency behavior.

Chapter 2

Analysis Tools

FEMM and LTspice® along with MATLAB® are used as a complete analysis package in this project. This combination is used for drawing the desired geometry, perform Finite Element Method (FEM) analyses, store results in arrays and structure arrays (structs), establish agreement between FEMM outcome and SPICE models and finally propose models and compare their validity and agreement to measurements performed using the impedance analyzer hp 4194A.

The application environment for the proposed models is LTspice®. As a time-domain circuit analysis tool, LTspice® can represent switching behaviour in detail. Proposed models demonstrating capacitive and inductive coupling paths of pre-assigned threshold limits in presence of power electronics converter (inverter), ESS, cables and other PWM-fed driven loads enables the prediction of CM circulating current.

In the power electronics converter model, transient analysis can be studied using either ideal switches or manufacturer's commercial models of switches available from the manufacturers' websites. In such a model, different features can be investigated like switching frequency, switching dead-time, slew rate (rise and fall times), modulation index and others.

Another alternative to the above-mentioned detailed representation of electric drive system, which only becomes significant when having access to a system or lab setup with the power electronics converter, is to record measurements at the terminals of the power converter in real-life conditions by Digital Storage

Oscilloscope (DSO). Then, these measurements can be configured as a voltage source that would drive the subsystem/component of interest under SPICE. This approach is simpler and optimized towards the subsystem/component of interest as it simulates "real-life" stationary conditions. The advantages are:

(i.) It saves simulation time substantially, especially when incorporating more than a single PWM-fed driven load of different ratings in the drive system.

(ii.) It gives the freedom of measuring high-frequency leakage currents without the need of having Rogowski coil or other specialized/expensive high-frequency current meters of a certain bandwidth.

2.1 Slot Analysis

On the way to develop the complete EMC machine model, the stator slot is taken as a basis for developing the model and highlighting the model's main parameters, namely the capacitances, resistances and inductances. The portion of the winding inside the stator slot represents the highest capacitance-to-ground contribution due to the proximity of copper conductors to the iron frame inside the slot, in presence of wire insulation and air. In the 1.5 kW openned Induction Machine (IM), the lumped value of one slot capacitance-to-iron frame (ground), with simple analytical approach, can range from $C_{sg} = 0.30 - 0.70$ nF. The outcome of the slot analysis can then be extended to the rest of stator slots taking in consideration the number of slots, number of phases, number of poles, end-turns layout and the winding arrangement. An Integral Slot (full-pitch) Single Layer Winding arrangement is considered for the current study where the winding is placed completely in two stator slots as shown in Figure 2.1 & Figure 2.2 below. The number of Slots per Pole per Phase (q) in this machine = 3, but from a slot perspective this does not make any difference as long as the winding arrangement is Integral Slot and Single Layer Winding, which means that the findings of the slot analysis for this particular machine are easily applicable to other machines holding the stated conditions.

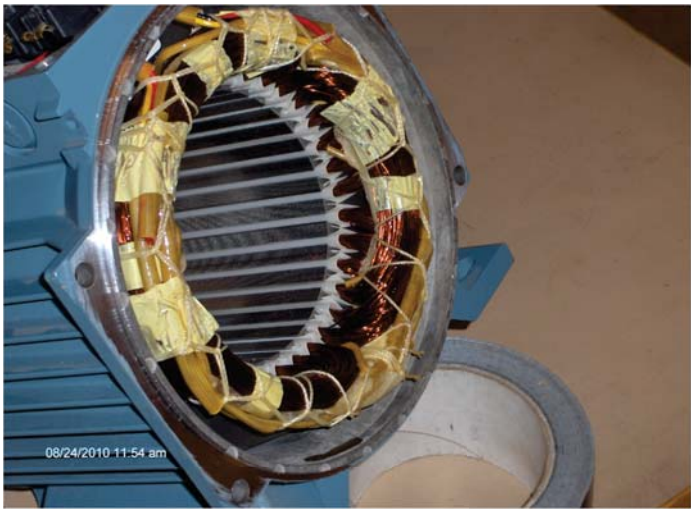

Figure 2.1: A photo of induction machine stator showing Integral Slot, Single Layer Winding of q=3 (36 slots, 3 phases & 4 poles) as well as the End Turns arrangement

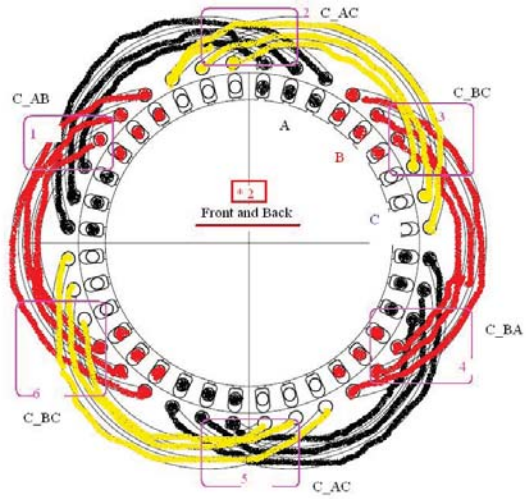

Figure 2.2: A side-view drawing of induction machine stator winding showing Integral Slot, Single Layer Winding of q=3 (36 slots, 3 phases & 4 poles) as well as its End Turns arrangement

2.2 "Macro Level" and "Micro Level" Machine Models

In order to link the slot level of analysis to the level of the complete EMC machine model, the so called "micro-level" analysis of the slot will represent a fundamental input to the "macro-level" model proposed in figure 2.3.

The model in Figure 2.3 represents an Integral Slot stator winding with $q = 3$. The associated capacitances-to-ground of the winding conductors inside the slots are expressed as lumped quantities on both sides of the coil winding inductance. The capacitances between phases in the End Turns region are approximated to capacitance values between "large conductors" of a width equivalent to the slot width, since each "large conductor" represents the total number of conductors inside a slot, as shown in Figure 2.4.

In this particular machine we have 4 electromagnetic poles, so the Pole Pitch (τ_p) is 90°. The interface area between the group of "large conductors" of adjacent phases will be expressed as follows:

$$InterfaceArea(A) = (\frac{5}{9} * \tau_p + \frac{3}{9} * \tau_p + \frac{1}{9} * \tau_p) * s_w = \tau_p * s_w \tag{2.1}$$

The Pole Pitch $\tau_p = \frac{\pi}{2} * r$; where r = 65.5 mm is the radius from the center up to the slot depth (yoke limit) of the stator in the radial direction, and $s_w = 4.5$ mm is the slot width. The capacitance can be expressed with the simple parallel-plate capacitance formula [10] as:

$$C = \frac{\epsilon_\circ * \epsilon_r * A}{d} \tag{2.2}$$

where $\epsilon_\circ$ is the permitivity constant of free space, ϵ_r is the relative permitivity (dielectric constant) for insulation paper and d=0.9 mm is the paper thickness between the two "large conductors".

$$= \frac{\frac{1}{36*\pi} * 10^{-9} * 3 * \frac{\pi}{2} * 65.5 * 10^{-3} * 4.5 * 10^{-3}}{0.9 * 10^{-3}} \approx 13.7pF \tag{2.3}$$

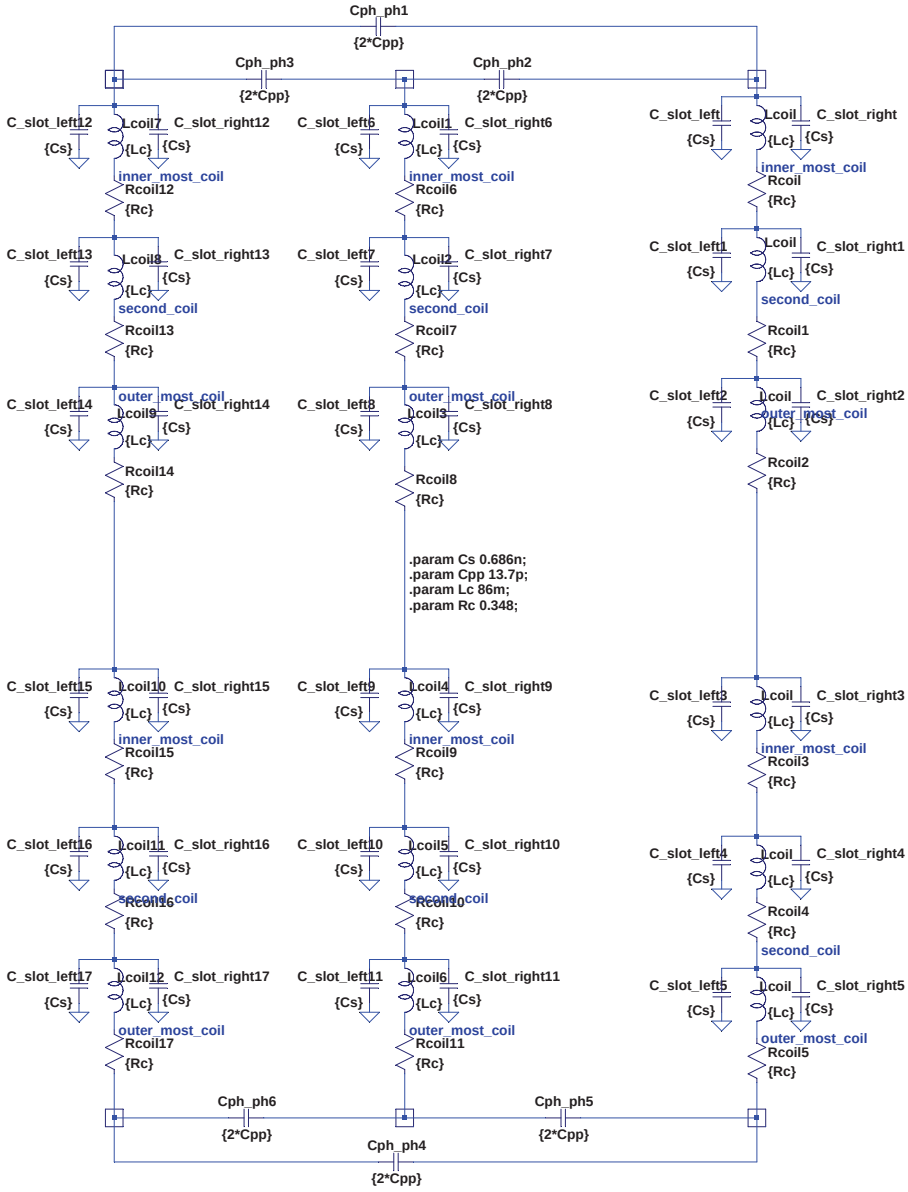

Figure 2.3: Macro(slot)-level circuit model of induction machine with Single Layer Winding of q=3

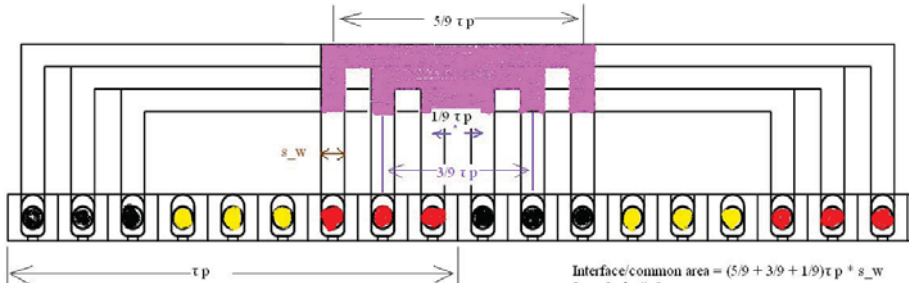

Figure 2.4: An unfolded view of the End Turns region approximating the interface between two adjacent phases in the machine stator

End Turns depend heavily on winding configuation and can be varied from one machine to another. For this machine one can notice from Figure 2.2 that two overlaps occur between any two adjacent phases in the End Turns region at each side of the stator. This is expressed by multiplying the capacitance value (13.7 pF) by a factor of "2". Then the capacitances between phases has to reflect the presence of End Turns in the front and back of the machine stator and that explains why we have the same capacitance representation at each end of the phases in the "macro-level" model in Figure 2.3.

It is worth noticing that "macro-level" modeling is based on established quantities in the machine design field like number of slots, number of phases, number of poles, winding arrangement, etc.; however the "micro-level" slot analysis, whose outcome is to be fed to the "macro-level" model, is analyzed according to the transmission line theory to reflect the frequency dependence phenomena of the conductors inside the slot.

2.3 Layer-to-Layer Approach for Slot Analysis

Considering a winding in a slot model on a layer-to-layer basis, the frequency-domain analysis in LTspice® can be considered as a rough and quick approach for developing transmission line models of low orders (few RLC-sections) as shown in Figure 2.5. Layer-to-layer approach has been adopted in [14]. With relatively fewer sections and standardised repeated parameters in each section, one can propose the parameter value based on rough analytical assumptions

and then perform sensitivity analysis while fixing the rest of parameters. Sensitivity analysis can be done by running the simulation for different values of the parameter of concern in both directions above and below the roughly estimated value. This can give the user an idea about the parameter value tendency and its influence on matching the model output with the measurement results; however this approach has limitations since it is based on rough assumptions and depends on trial-and-error methodology which is not very sound neither accurate. So manual representation in frequency-domain circuit analysis can be used as a comparison tool to measurement data, but generating the model and selecting its parameters has to be based on finer assumptions and performed in a systematic way which will be more scientifically motivated.

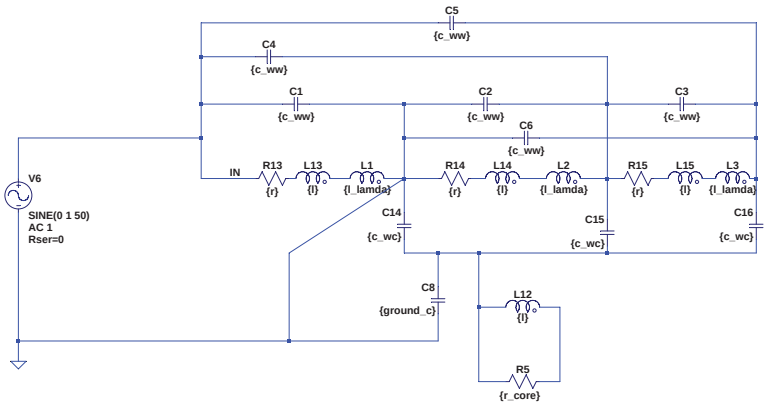

Figure 2.5: Layer-to-layer approach for sensitivity analysis in frequency domain for a 3-layer winding represented by 3 RLC-sections

2.4 Turn-to-Turn Approach for Slot Analysis

The turn-to-turn analysis level is adopted in modelling the winding portion in a stator slot. Turn-to-turn approach has been followed in [20][21][35][24]. As a result the transmission line model is of a high order due to the number of turns and this shows the significance of generating such a model automatically. The represented parameters concerning each turn in the model are proposed to be:

(i.) Resistance of each winding turn (R_t).

(ii.) Capacitances between the winding turns (C_{tt}),

(iii.) Capacitances between each winding turn and the ground (C_{tg}),

(iv.) Inductance of each winding turn (L_t),

(v.) Mutual inductance between winding turns represented by coupling factors.

Magnetic core losses composed of hysteresis and eddy current losses are represented in a so called "ladder diagram" that represents the frequency dependence behaviour of the turn resistance and inductance (see section *inductive coupling matrix* 4 later). The conductor insulation losses existing between adjacent turns and between each turn and the ground are not represented in the model.

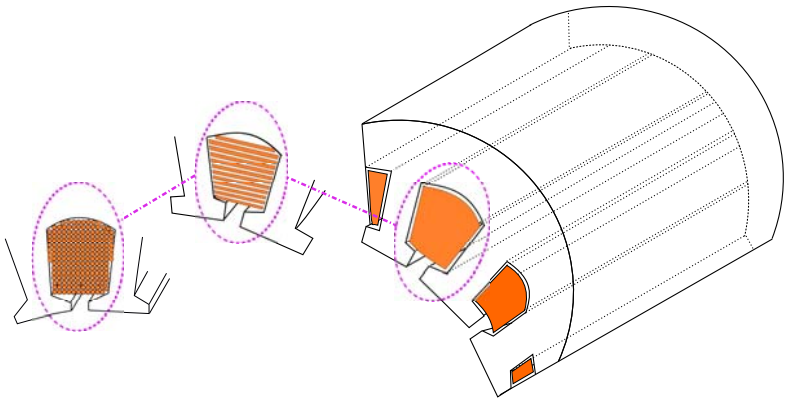

Figure 2.6: Analysis development of the winding portion modelling inside a slot. First the winding is considered as one complete unit, then it's divided into layers and finally is represented by turns

2.5 Simple Winding-on-Core Prototype

On the turn-to-turn level of modelling, the representation of a complete machine winding inside a slot becomes very complex and a tedious job to do, so a

simplification is proposed by one of the reference group members [31], to form a common starting point in order to develop the model and then test it and validate it for the frequency band of interest. A prototype of a simple winding on an iron core is built. It has 24 turns and 3 layers, in both distanced and condensed wire arrangements as shown in figure 2.8 below. In the condensed arrangement the conductors are wound close to each other as the case would be in a machine winding, while in the distanced arrangement the conductors are wound 3 mm apart, both on the layer level among the turns, and among the turns in different layers. The impedance of each arrangement at four different access points are measured and analysed along the frequency range of interest. Access points represent the start and end terminals of the winding, in addition to the start of each layer as per the following table 2.1.

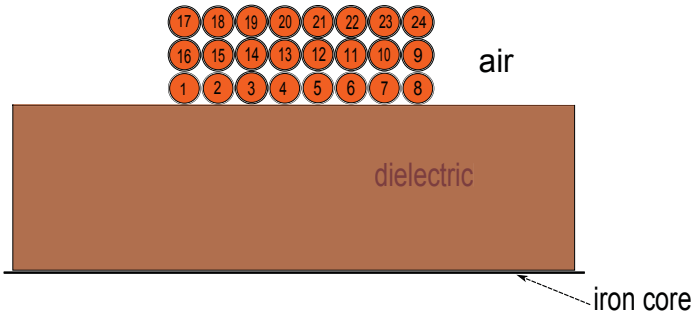

Figure 2.7: The 24 conductors arrangement for electrostatic FEMM analysis

Access Points	Location
1^{st}	Winding input
2^{nd}	Second Layer Input
3^{rd}	Third Layer Input
4^{th}	Winding output
5^{th}	Iron core

Table 2.1: Measurements access points in the 3-layer 24-winding-on-core prototype

As in sections 2.3 and 2.4 before, frequency-domain circuit analysis is used, but this time automatically, to generate and verify the validity of the proposed

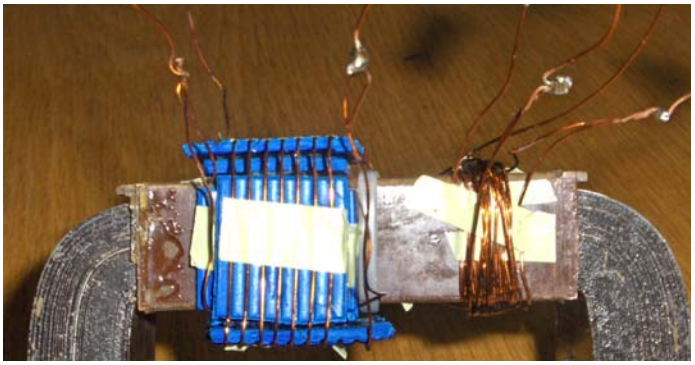

Figure 2.8: 3-layer 24 turns winding-on-core model in both distanced and condensed wiring arrangements

RLC transmission line model of the built prototype in comparison to the measurements from the impedance analyzer hp 4194A. The parameters are motivated from FEMM analysis. Capacitance (C) parameters are taken from the outcome of FEMM electrostatic analysis where a *Capacitive Coupling Matrix* is produced. Resistance and inductance (R & L) parameters are taken from FEMM magnetostatic and time-harmonic magnetic analysis where an *Inductive Coupling Matrix* is produced. The entire process is automated and centralised from MATLAB® as a single platform.

Chapter 3

Capacitive Coupling Matrix

This chapter explains the background and details behind FEM electrostatic analysis of the prototype model. It puts the reader in the steps of creating the *Capacitive Coupling Matrix*. It displays results and the link to the capacitance network in a circuit simulation environment.

3.1 Electrostatic FEMM Modelling

The built prototype model is modelled in FEMM electrostatic analysis as 24 copper conductors in a 2D planar problem for the condensed wiring arrangement, where one turn is represented as a conductor with depth of (44*2+25*2 = 138 mm) inside the plane, which is equivalent to one turn's length. The conductor diameter including insulation is measured to be 0.648 mm while the copper diameter itself is 0.589 mm [16].

Conductors are drawn with their insulation and placed close to each other in an orderly manner the same way they are wound in reality. Numbering the conductors start from left to right in odd layer numbers and from right to left in even layers numbers, just as it is done in reality; so conductor number one starts from bottom left closest to iron core and conductor number 8 is far right in the First Layer, conductor number 9 starts from the right side of Second Layer and continues till number 16 far left at the end of it and so on.

Besides the conductor insulation a dielectric of 3 mm high is drawn and configured above the iron core. A semi-circle of a radius of 30 mm is drawn on the iron core outside the Bobbin area, and used as mixed boundary condition where electric field lines tend to vanish. The iron core is considered as a ground and drawn with a single line that is assigned a zero voltage potential. The drawing process is done through MATLAB® code that uses the Lua Scripting language. The conductors arrangement is shown in figure 3.1 below.

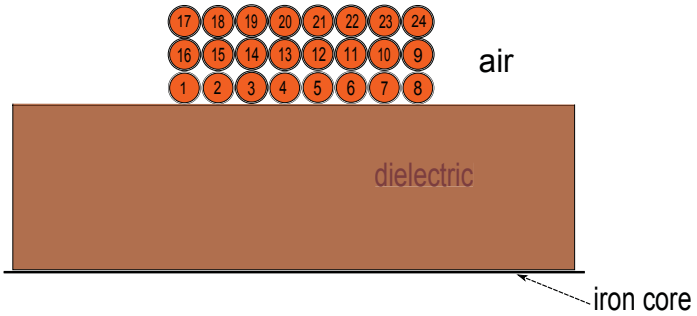

Figure 3.1: The 24 conductors arrangement for electrostatic FEMM analysis (repeated)

The problem boundary is configured with a "mixed" boundary condition according to equation 3.1

$$\epsilon_\circ * \epsilon r * \frac{\partial V}{\partial N} + c_\circ * V + c_1 = 0 \tag{3.1}$$

The "mixed" boundary condition can be achieved by setting $c_1 = 0$ and solving for $c_\circ$ in equation 3.1 above, the condition then would approximate an unbounded solution region inside the border it is assigned for, in a FEMM electrostatic problem [23].

3.1.1 Capacitance Matrix for Multi-Conductor System

The objective of the analysis is to find the capacitance matrix for the 24 conductors where mutual capacitances between any two conductors can be predicted, meanwhile it would be possible to express the capacitance-to-ground for each conductor.

Referring to Cheng's *Capacitances in Multi-conductor Systems* [10], the capacitance system matrix elements consist of diagonal elements (c_{ii}) and non-diagonal elements (c_{ij}) where ($i \neq j$ & $i, j = 1, 2, 3 \cdots n$, "n" is the number of conductors in the system).

Diagonal elements (c_{ii}) are called the *coefficients of capacitance* for the i^{th} conductor in the system. They are positive constants and represent, in physical terms, the total capacitances between the i^{th} conductor and every other conductor in the system, as well as between the i^{th} conductor and its ground. On the other hand, non-diagonal elements (c_{ij}) where ($i \neq j$) are called the *coefficients of induction* [10], and exist between the i^{th} and j^{th} conductor. They are negative constants that represent the mutual partial capacitance between the i^{th} and j^{th} conductor in the system.

Adding the negative constants representing mutual capacitances to the diagonal elements representing the total capacitances of a conductor gives the capacitance-to-ground value for the i^{th} conductor of concern.

3.2 How the *Capacitive Coupling Matrix* is created?

The electrostatic FEMM analysis for the prototype model is done by assigning a voltage value of 1 V as a circuit property to one conductor of the 24 conductors while the rest are assigned zero voltages, then the problem is analyzed and solved for the charge Q on each conductor in the system. Results are saved in a matrix and the same procedure is repeated, in an automated way by help of MATLAB®, for every conductor in the wiring arrangement. The result represents a capacitance system matrix of order 24 by 24, given that the capacitance value is the same as the charge value for a voltage of 1 V since $Q = C * V$.

The *Capacitive Coupling Matrix* is basically a post-processed capacitance matrix for a multi-conductor system where its diagonal elements are positive constants that represent the capacitance-to-ground for each conductor, while its non-diagonal elements are positive constants that represent the mutual capacitance for the corresponding conductors as shown in figure 3.4.

As can be observed from figure 3.2 above, the highest values for capacitance-to-ground (C_{tg}) occur in the First Layer interfacing the core, with maximum

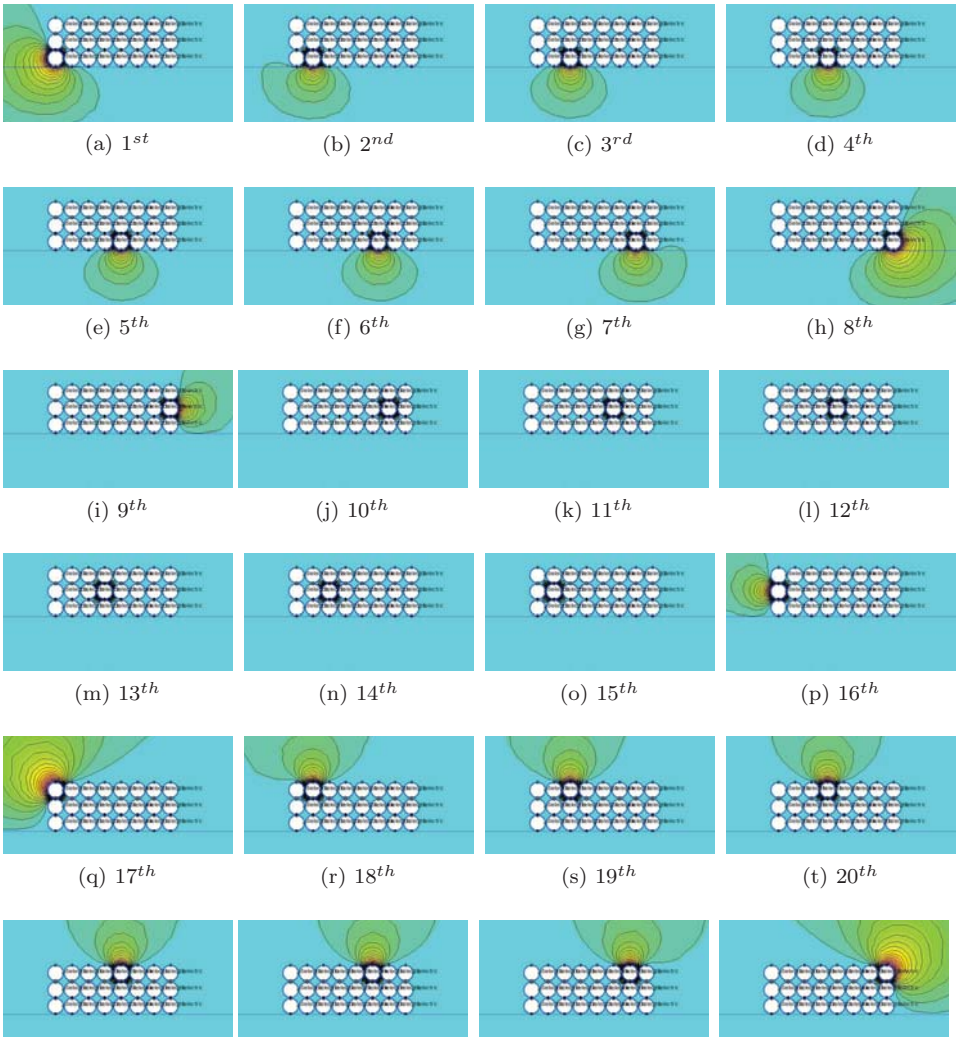

(a) 1^{st} (b) 2^{nd} (c) 3^{rd} (d) 4^{th}

(e) 5^{th} (f) 6^{th} (g) 7^{th} (h) 8^{th}

(i) 9^{th} (j) 10^{th} (k) 11^{th} (l) 12^{th}

(m) 13^{th} (n) 14^{th} (o) 15^{th} (p) 16^{th}

(q) 17^{th} (r) 18^{th} (s) 19^{th} (t) 20^{th}

(u) 21^{st} (v) 22^{nd} (w) 23^{rd} (x) 24^{th}

Figure 3.2: Electrostatic FEMM analysis of 24 conductors on core - condensed arrangement

values on the edges since the electric field lines can couple directly to the core without any barriers. Second Layer capacitance-to-ground (C_{tg}) is the lowest with absolute values in the order of 10^{-19} Fs which represent 7 orders of magnitude lower than the first layer's capacitance-to-ground (C_{tg}). This is due to the electric field being confined between two copper layers which represent electrostatic shields banning the electric field to couple to the core. This is not fully true for the conductors on the edges, conductor 9 & 16.

It can be also observed that the most intense electric field potential lines lie between two adjacent conductors, especially in the outer layers, i.e. the First and Third Layers, and that reflects on the adjacent turn-to-turn capacitance values (C_{tt}) to be the highest.

By comparing the effect of the same stimulus applied to the conductors of the Third Layer as shown in sub-figures 3.2q to 3.2x, to the one applied to the conductors of the Second Layer as shown in sub-figures 3.2i to 3.2p one can observe that in the Third Layer case, which is exposed to the air from one side, electric field lines are more distributed and spread linking larger interface areas of the conductors through the lossless medium of air, than the case of the Second Layer where electric field lines are mainly linked to the neighbouring conductor through smaller interface area between the two adjacent conductors. This will result in higher adjacent turn-to-turn capacitance between conductors in the Third Layer than the Second Layer. Considering the confined electric field between the Second Layer and the First and Third Layers, we can state that electric field lines between two adjacent conductors in the Second Layer does not exceed half the circumference of each conductor, as shown in the figure 3.3. The above mentioned observations can also be read from figure 3.4 and subfigures 3.8a & 3.8b.

The conclusion is that conductor layers represent electrostatic shields between inner and outer layers, consequently the First Layer interfacing the core would represent an electrostatic shield between inner layers of conductors and the ground.

When this behaviour is to be extended to a complete machine winding inside a slot, where iron core encircles the copper conductors from all sides, and following the same reasoning for the electric field lines, one needs only to consider the contribution of the First Layer of conductors interfacing the iron for calculating the capacitance-to-ground. For adjacent turn-to-turn capacitance considering the somewhat random process in forming the winding, the approach would be to develop the *Capacitive Coupling Matrix* for the conductors inside

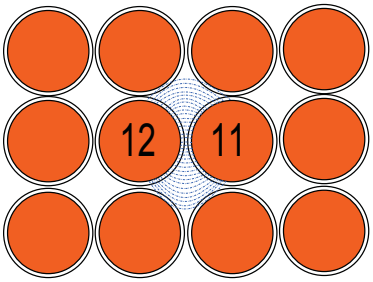

Figure 3.3: Electric field lines connecting conductors 11 and 12 in the inner most layer, the Second Layer

the slot considering an ideal situation where each turn is followed by the next in an orderly manner, and then multiply it by a permutation matrix expressing the unpredictable positioning of some turns in the slot. This implementation will be made in the next phase of the project.

Since the *Capacitive Coupling Matrix* for the simple winding prototype is of order 24 x 24 = 576 elements, the best way to view it is in a 3D plot and 2D image as shown in figure 3.4. Linear scale is used in figure 3.4 which reflects differences in absolute values of capacitances in the multi-conductor system. The two parallel red spike lines around the main diagonal in figure 3.4a correspond to the turn-to-turn capacitances of adjacent conductors while spike lines perpendiular to the diagonal represent the adjacancy between the layers; one between the First and Second Layers, and the other between the second and Third Layers. It should be noted that the matrix is symmetric around the diagonal so there is information redundancy above and below the diagonal elements.

Note the steep valley in figure 3.4 represented by the main diagonal elements which shows the difference between turn-to-ground and turn-to-turn capacitance values. Turn-to-ground capacitance values can also be seen in figure 3.5 while turn-to-turn capacitance values in figure 3.6.

The same behaviour can be seen in the 2D image of the matrix in figure 3.4b, with a clearer view about the difference in the magnitude between the elements. X & Y represent the position of the element in the matrix. First main diagonal element starting top left in the matrix corresponds to the first conductor in the wiring arrangement, while the last element ending bottom right correponds to the last conductor.

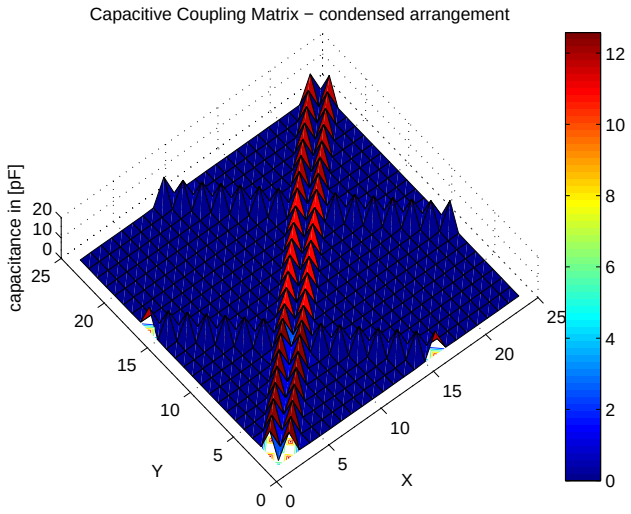

(a) 3D plot of the Capacitive Coupling Matrix

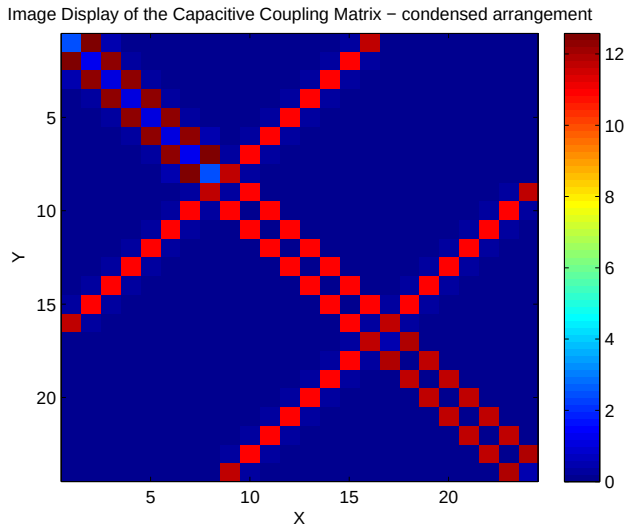

(b) 2D image of the Capacitive Coupling Matrix in (pF). Note the highest turn-to-turn capacitance values among the first 8 conductors (First Layer)

Figure 3.4: Linear scale representation of Capacitive Coupling Matrix for the system of 24 conductors on iron core - condensed arrangement

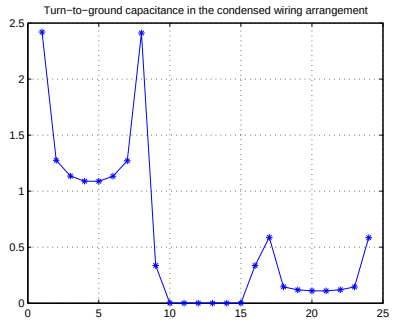

Figure 3.5: Turn-to-ground capacitance in pico farads [pF] for conductors in the condensed wiring arrangement, represented by the main diagonal elements in the *Capacitive Coupling Matrix*

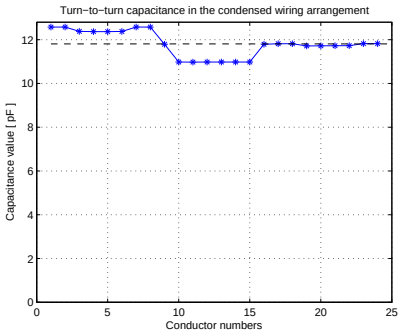

(a) Y-axis starts from zero

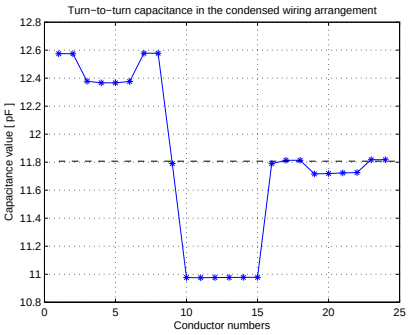

(b) zoomed to show the difference between values

Figure 3.6: Adjacant turn-to-turn capacitance in pico farads [pF] for conductors in the condensed wiring arrangement, represented by the first diagonal above (or below) the main one in the *Capacitive Coupling Matrix*

Note the highest values for turn-to-turn adjacent capacitance among the first 8 conductors (First Layer) followed by the last 8 conductors (Third Layer) compared to the rest. This can also be seen from figure 3.6. Values are higher in the First Layer than in the Third Layer due to the proximity of the First Layer to the iron core, which in turn is configured with ground potential where electric field is zero. This tends to force electric field lines to be more intense near the conductors facing the dielectric towards the core in the First Layer. On the other hand, conductors in the Third Layer face air and ultimately the outer boundary of the problem at farther distance, which will not influence the electric field lines distribution around the conductors of the Third Layer.

Note also that the highest turn-to-ground capacitance values are for conductors in the First Layer, however these values are significantly lower than turn-to-turn capacitance values due to the longer electric field path coupling the conductor to the core (ground) compared to the path coupling the conductor to the neighbouring conductor.

3D plot and 2D image for the *Capacitive Coupling Matrix* are represented in a logarithmic scale in figure 3.7 in order to cover all capacitance values in the system matrix meanwhile express the small differences. The logarithmic plot is the best in telling the relative difference among the plotted elements. In figure 3.7 there is more than 440 Decibels (dBs) difference between the values (For dB see Appendix A [34]) which corresponds to 22 orders of magnitude. Lowest values being for mutual capacitance between conductors surrounded totally by other conductors from all sides, like the capacitance between conductors 10 & 15 in the Second Layer, while the highest, as stated before, is between conductors in the First Layer.

3.3 Sparse Matrix Representation

To systematically link the outcome of the previous capacitance analysis to the transmission line modelling of the winding on an iron core, a sparse matrix is generated from the *Capacitive Coupling Matrix* by introducing a threshold according to the level of accuracy the designer wishes to represent. The sparse matrix only contains the values in the *Capacitive Coupling Matrix* which are above or equal to the stated threshold. All other elements are represented by zeros. Figure 3.8 below shows some examples of sparse matrix representations with different threshold values. It also indicates the number of nonzero elements

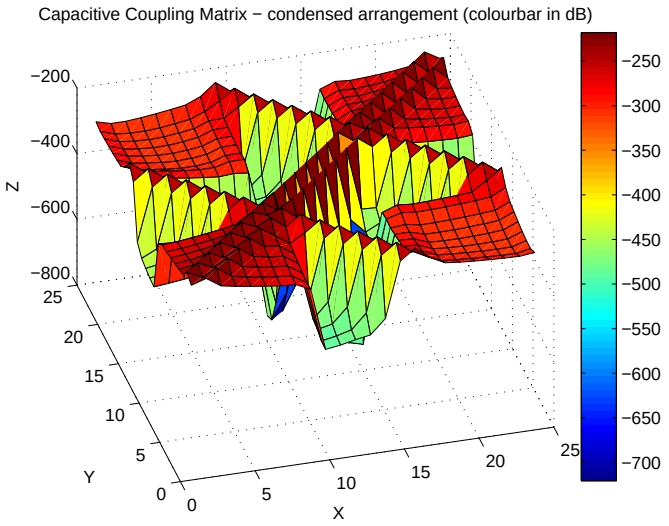

(a) 3D Logarithmic plot of the Capacitive Coupling Matrix

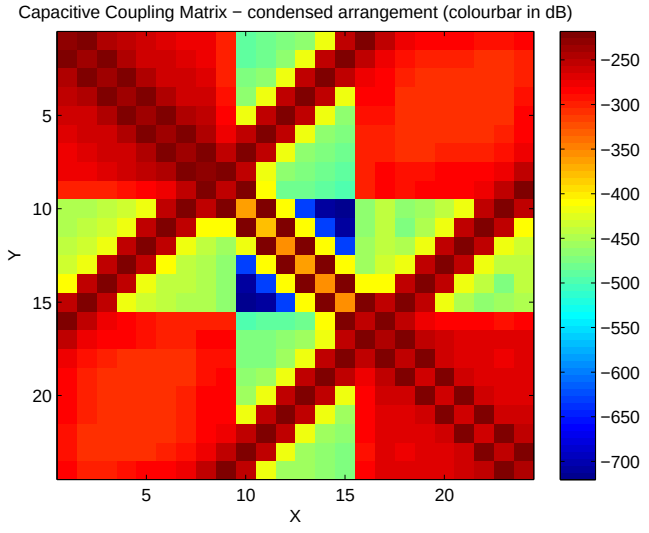

(b) 2D Logarithmic image of the Capacitive Coupling Matrix

Figure 3.7: Logarithmic scale representation of Capacitive Coupling Matrix for the system of 24 conductors on iron core - condensed arrangement

in each example. The different threshold values in figure 3.8 are derived from the maximum value in the *Capacitive Coupling Matrix*, which is 12.58 pF and corresponds for the adjacency capacitance between the first two conductors on each side of the first layer, i.e. capacitance value between conductors 1 & 2, and between conductors 7 & 8 as shown in figure 3.6b.

Figure 3.9 shows more examples of sparse matrices with substantially lower threshold values. These patterns show the outcome of finer limits set to the capacitance values to be modelled. Such accurate patterns would be impossible to predict without numerical modelling, i.e. with only anayltical techniques, or with analytical techniques coupled with trial-and-error sensitivity analysis mentioned earlier in sub-sub-section 2.3 "Layer-to-Layer Approach for Slot Analysis" and shown in figure 2.5. Threshold limits for capacitance values in the *Capacitive Coupling Matrix* can be looked at as the minimum capacitance value to be represented in the transmission line model.

3.4 From Sparse Matrix to Capacitance Network

For a given threshold value that reflects the level of accuracy desired, the sparse matrix is used to generate the LTspice® netlist that represents the capacitance values in the transmission line model of the winding. The transmission line model is subsequently analyzed under LTspice® frequency-domain analysis.

Below in figure 3.10 a threshold limit of 5% of the maximum value in the *Capacitive Coupling Matrix* is chosen. The pattern shows, and is used to model, the adjacent turn-to-turn capacitance for all conductors in the wiring arrangement, meanwhile it shows the First Layer conductor-to-ground capacitances.

As previous patterns with lower threshold levels have suggested, and according to the conclusion realized before that only the first copper conductor layer facing the core would count in the capacitance-to-ground values; it is not worthy to lower the threshold further and include the backward conductor layers in the model, since that only increases the complexity of the model without adding any substantial accuracy.

Since the matrix is symmetric around the main diagonal in figure 3.10, only one half of the matrix is considered when using it as an automatic input to the

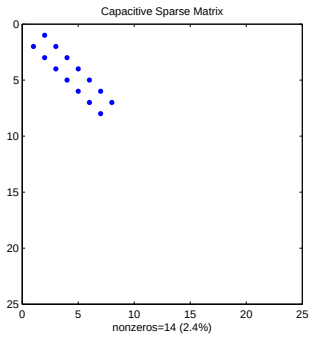

(a) Threshold is 94% of the matrix maximum value. Pattern is maintained from 94%-98% of maximum value

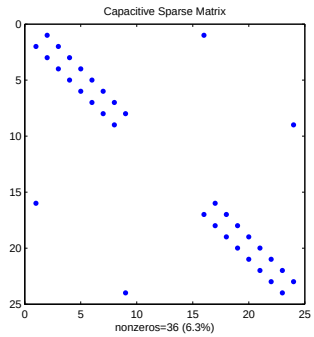

(b) Threshold is 88% of the matrix maximum value. Pattern is maintained from 88%-93% of maximum value

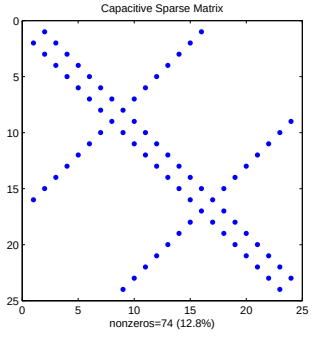

(c) Threshold 20% max. Maintained from 20%-87% of max value, the *broadest pattern*

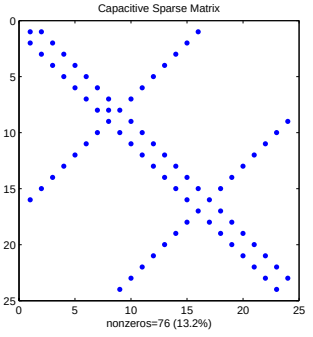

(d) Threshold is 11% of max value. Pattern is maintained from 11%-19% of max value

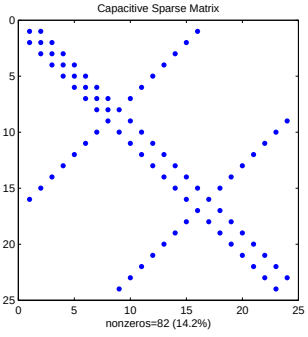

(e) Threshold is 5% of max value. Pattern is maintained from 05%-08% of max value

Figure 3.8: Examples of sparse matrices with different threshold values for the simple winding prototype - condensed arrangement

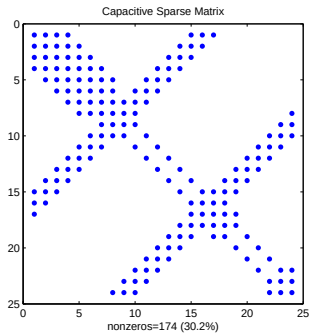

(a) Threshold is set to be of two orders of magnitude below the matrix maximum value

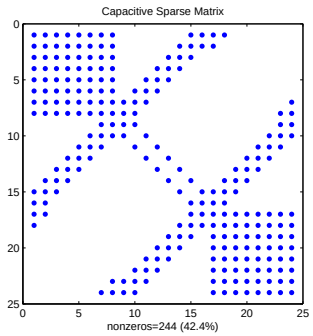

(b) Threshold is set to be of three orders of magnitude below the matrix maximum value

Figure 3.9: Sparse matrices with substantially lower threshold limits for the simple winding prototype, the condensed wiring arrangement

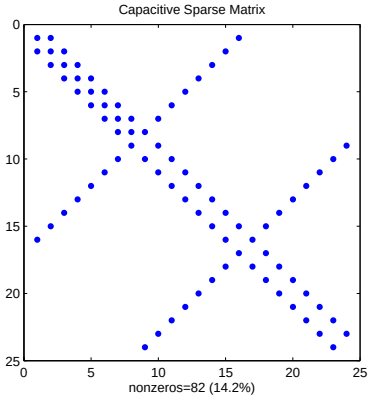

Figure 3.10: The sparse matrix chosen to be fed to the transmission line model in LTspice®

transmission line circuit model. As shown in figure 3.11 only the upper half is taken.

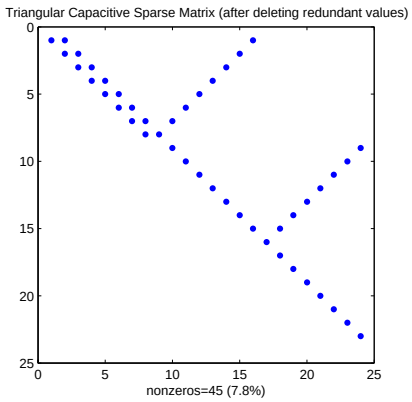

Figure 3.11: The upper half of the sparse matrix to be fed automatically to the transmission line model in LTspice®. No redundancy included

The resulting netlist file for the capacitance network in the transmission line model is shown below. It is generated automatically from the processed sparse matrix through a MATLAB® code.

```
C_1-0 N001 0 2.420272e-012
C_1-2 N001 N002 1.257473e-011
C_2-0 N002 0 1.274958e-012
C_2-3 N002 N003 1.237769e-011
C_3-0 N003 0 1.135148e-012
C_3-4 N003 N004 1.236700e-011
C_4-0 N004 0 1.088643e-012
C_4-5 N004 N005 1.236629e-011
C_5-0 N005 0 1.088575e-012
C_5-6 N005 N006 1.236658e-011
C_6-0 N006 0 1.133048e-012
C_6-7 N006 N007 1.237622e-011
C_7-0 N007 0 1.271504e-012
C_7-8 N007 N008 1.257776e-011
C_8-0 N008 0 2.411273e-012
C_8-9 N008 N009 1.176068e-011
C_7-10 N007 N010 1.097555e-011
C_9-10 N009 N010 1.097355e-011
```

```
19 C_6-11 N006 N011 1.097403e-011
20 C_10-11 N010 N011 1.097453e-011
21 C_5-12 N005 N012 1.097580e-011
22 C_11-12 N011 N012 1.097313e-011
23 C_4-13 N004 N013 1.097410e-011
24 C_12-13 N012 N013 1.097628e-011
25 C_3-14 N003 N014 1.097770e-011
26 C_13-14 N013 N014 1.097429e-011
27 C_2-15 N002 N015 1.097599e-011
28 C_14-15 N014 N015 1.097765e-011
29 C_1-16 N001 N016 1.176263e-011
30 C_15-16 N015 N016 1.097829e-011
31 C_16-17 N016 N017 1.178963e-011
32 C_15-18 N015 N018 1.097689e-011
33 C_17-18 N017 N018 1.181399e-011
34 C_14-19 N014 N019 1.097381e-011
35 C_18-19 N018 N019 1.171499e-011
36 C_13-20 N013 N020 1.097684e-011
37 C_19-20 N019 N020 1.171617e-011
38 C_12-21 N012 N021 1.097569e-011
39 C_20-21 N020 N021 1.171870e-011
40 C_11-22 N011 N022 1.097463e-011
41 C_21-22 N021 N022 1.172336e-011
42 C_10-23 N010 N023 1.097594e-011
43 C_22-23 N022 N023 1.172585e-011
44 C_9-24 N009 N024 1.179031e-011
45 C_23-24 N023 N024 1.181752e-011
```

After the row number on the left side, the first column in the netlist file represents the capacitance labels with subscripts indicating turn numbers. The second and third columns represent the first and second nodes (turns) numbers, respectively, which the capacitance links. The numbers are written in the format that LTspice® accepts (NXXX). The last column is the capacitance value in *Farads*.

Figure 3.12 below shows the capacitance network equivalent to the generated netlist file above, but drawn manually in LTspice®.It is observed from the capacitance network that turn-to-ground capacitance values in the First layer are lower than turn-to-turn capacitances. On average they are 13% lower; However they will represent the dominant path to ground from any turn in the arrangement. The equivalent of any series-connected capacitances is dominated by the lower capacitance value which corresponds to higher impedance as $X_c = \frac{1}{\omega C}$.

The significance of this method is appreciated more when applied to complex situations with excessive number of turns, like the stator slot case with high fill

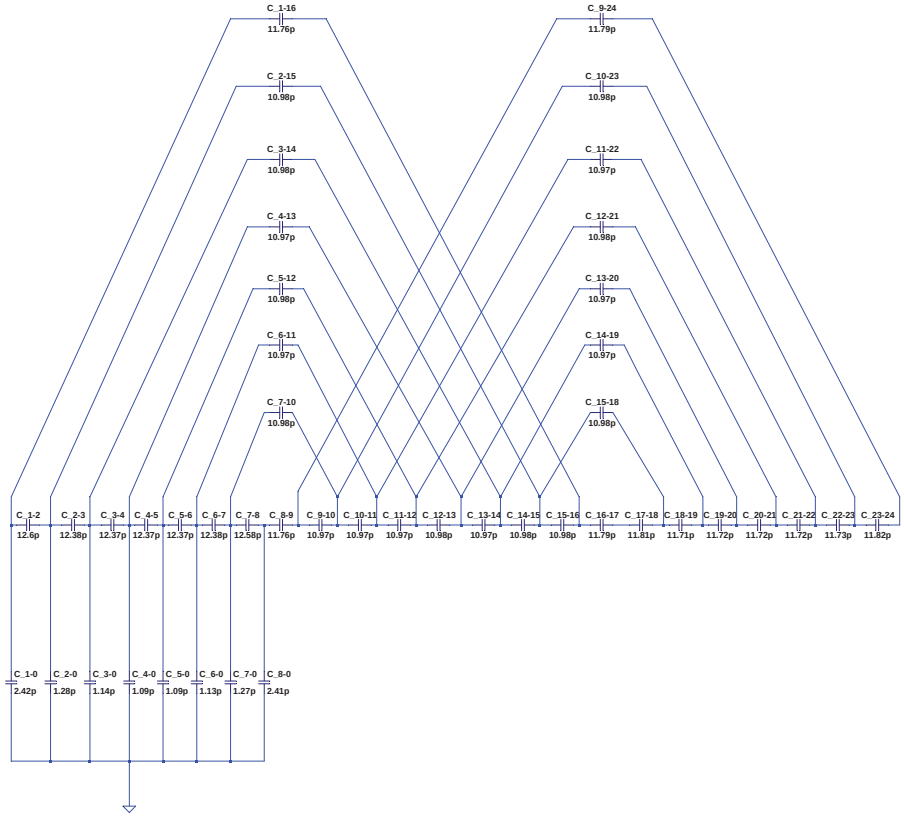

Figure 3.12: Capacitance network equivalent to the code in the netlist file above, drawn manually in LTspice®

factor. Automating the drawing process then, by generating the netlist file, becomes of high value since one is dealing with high-order transmission line model representing adjacent turn-to-turn capacitances.

By automatically generating the netlist file, one avoids the burden of manually drawing a complex capacitance network of high-order, which is a difficult task for humans to do, consume lots of time and effort, and is usually and easily prone to mistakes. A feeling of how complex the capacitance network from a stator slot case might get, can be sensed from figure 3.12 above, which only represents the case of 24 turns in the winding arrangement prototype after being subjected to a threshold limit of 5% of the maximum capacitance value in the corresponding multi-conductor system.

Chapter 4

Inductive Coupling Matrix

After being able to investigate capacitance-to-ground and mutual capacitance between conductors in a multi-conductor system from the previously introduced *Capacitive Coupling Matrix* in chapter 3, a similar approach is followed when investigating the inductance in the system.

The *Inductive Coupling Matrix* tells about self inductance for each conductor, as well as mutual inductance between any two conductors in the multi-conductor system.

Here a special attention is given to the fact that unlike capacitance, inductance is highly dependent on frequency, since the penetration depth of the magnetic field inside various materials and media is dependent on its frequency but also the properties of the medium being subjected to the field and penetrated, namely the medium's conductivity and permittivity according to the formula 4.1 below [10][12]:

$$\delta = \sqrt{\frac{1}{\pi f \mu \sigma}} \tag{4.1}$$

where δ is the penetration depth of the magnetic field in the material, in meters [m], π is the mathematical constant 3.142, f is the frequency in [Hz], μ is the permeability of the material in [H/m] and σ is the material conductivity in [S/m].

Figure 4.1 below shows the penetration depth (skin depth) in [mm] for different types of materials along a frequency sweep from 0 Hz to 1 MHz. Note the general behavior that penetration depth in these materials decreases as frequency increases. Note also that metal conductors like aluminum, gold and copper have relatively the highest penetration of magnetic fields while ferromagnetic materials like iron has the lowest. This is mainly due to the higher relative permeability (μ_r) for iron compared to other elements. Although the relative permeability (μ_r) is a desirable characteristic which contributes to superior magnetic behavior for the ferromagnetic material, it also contributes to lower penetration depth. This can even be seen for different relative permeability values within iron itself in figure 4.1. This fact makes us consider thin laminations and low-frequency effectiveness for high permeability iron.

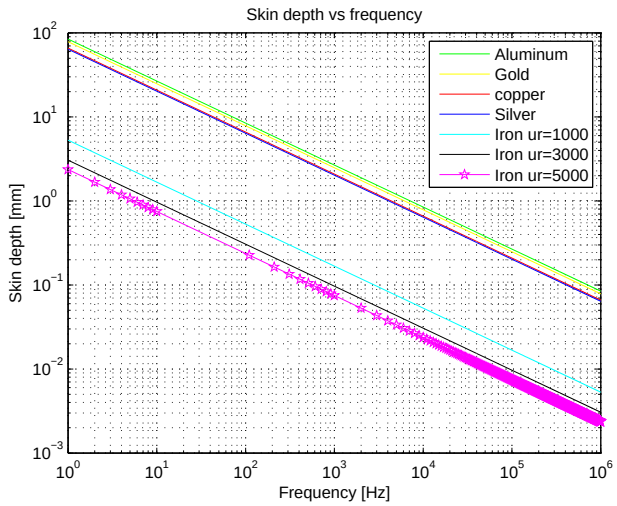

Figure 4.1: Penetration/Skin depth for different types of materials along a frequency sweep from 0 Hz - 1 MHz

The 24-turn winding arrangement prototype is being modeled under FEMM magnetostatic and time-harmonic magnetic analyses, in a way that application of static and quasi-static solvers is justified by maintaining the cross-sectional dimensions of the problem small compared to the wavelength of the analysis frequency. By 'small' one means the dimension is below ($\frac{\lambda}{4}$); the limit at which the reflection effect of the electromagnetic wave can be noticeably observed

[29][17]. A range for the dimension (d) where $\frac{\lambda}{10} < d < \frac{\lambda}{5}$ is acceptable in the modelling depending on accuracy and simulation time sought.

The wavelength (λ) of an electromagnetic wave at a certain frequency, is the distance in meters [m] which this wave travels in the medium (usually free space/air) in one period of its frequency. In free space, electromagnetic waves travel with the velocity of light $c \approx 3 * 10^8$ [m/s]. In power cables, the electromagnetic waves travel in the range of 40-60% of light speed [17], as the relative dielectric constant (permitivity) for typical cable insulations varies from 3 to 8 [12][10].

Given the frequency of the wave to be (f) and the free space as the traveling medium, then the wavelength (λ) in meters is expressed as:

$$\lambda = \frac{c}{f} \tag{4.2}$$

Table 4.1 and figure 4.2 below show some common frequencies versus their corresponding wavelength in free space [7]. It covers the frequency range from 0 Hz - 30 MHz over which the conducted emission problem is most severe [15].

Frequency [Hz]	(λ) in free space [m]
50	6 000 000
1 000	300 000
10 000	30 000
1 000 000 (1 MHz)	300 (AM radio band)
10 000 000 (10 MHz)	30
30 000 000 (30 MHz)	10

Table 4.1: Key frequencies versus their corresponding wavelength (λ) in free space

Given the converter output voltage rise time (t_r), and the electromagnetic wave propagation velocity in the conductor or cable of interest ($v_{propagation}$), then the wavelength corresponding to the critical conductor length ($\lambda_{critical}$) is expressed as [17]:

$$\lambda_{critical} = t_r \cdot v_{propagation} \tag{4.3}$$

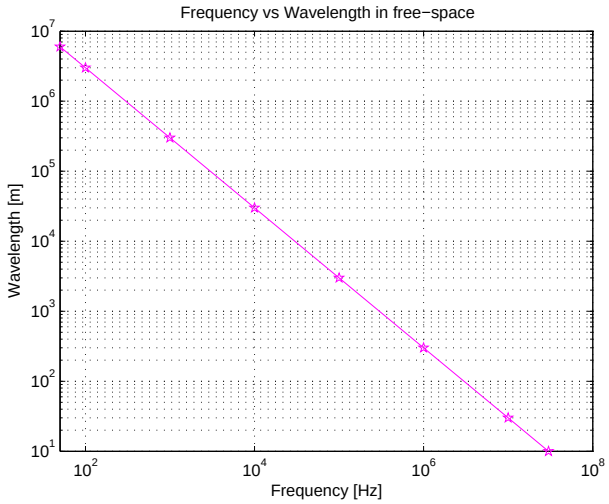

Figure 4.2: Frequency versus the corresponding wavelength (λ) in free space for frequency range from 50 Hz - 30 MHz

The built prototype model for the condensed wiring arrangements is modelled as 24 copper conductors in a 2D planar problem. As in the electrostatic analysis, the conductor (and core) depth inside the plane is 138 mm which is equivalent to one turn's length. The conductor diameter including insulation is 0.648 mm while copper diameter itself is 0.589 mm. Conductors are drawn with their insulation and placed close to each other where center of conductors of different layers lie on the same vertical axis. They are numbered in an orderly manner as they were wound in reality. See figure 3.1 in the previous section. They start from left to right in odd layer numbers and from right to left in even layer numbers. The Bobbin on which the winding is wound, is represented by a 3 mm high dielectric material above the iron core.

The iron core in the model is represented by two parallel lines with a length that is equal to the centerline length of the core's peripheral, and a thickness of 10 mm that corresponds to half its measured thickness due to magnetic symmetry. An iron lamination is approximated to be 250μm and modeled in the x-axis orientation under the magneto-static analysis, despite part of the core laminations are oriented in the y-direction, as can be seen from figure 2.8 shown

previously. The reason being is that x-axis oriented laminations represent the iron core part where the Bobbin and winding lie, in addition the approximation of unfolding the core length to be represented in the 2D plane is taken from the x-axis orientation perspective for the laminations sheets. The core depth inside the plane is the same as one turn's length which is 138 mm.

Between the two ends of the unfolded core, an arc with a radius of 160 mm is drawn to represent the outer boundary limit that is assigned "mixed" boundary condition to model an unbounded problem [23]. Both ends of the core are configured with "Periodic" boundary conditions [23] to reflect that they are connected in reality and the resulting magnetic field will be the same at both of them. The top line of the core is configured with local element size that is dependent on the analysis frequency, and the bottom line is configured with a prescribed zero boundary condition where the magnetic vector potential, A, has a zero value. As the normal flux component is equal to the tangential derivative of the magnetic vector A along the boundary, the magnetic flux lines vanish when they approach this prescribed boundary. A screenshot of the described FEMM magnetic problem is shown in figure 4.3 below.

The iron core is configured with an iron block property which has a linear B-H relationship, as a simple case is considered to start with, besides there was no reliable information available about this particular core. The relative permeability (μ_r) considered for iron is 5000 both in the x- and y- directions. The laminations are considered to be laminated in x-direction for magneto-static analysis and in into-the-plane direction for AC time-harmonic magnetic analysis as the solver could not solve the proplem when having laminations oriented in either x- or y- directions under time-harmonic magnetic analysis, the reason being that on-edge laminations are not supported by the AC analysis solver [23]. The iron block property details is shown in figure 4.4 belwo.

The analysis is performed by assigning each conductor in the system a circuit property with a current value of 1 A, while the rest of conductors are assigned circuit properties of zero current values. The problem is solved for the self-inductance value for the conductor of concern, i.e. the one which has the stimulus current of 1 A, meanwhile it is also solved for the mutual inductance between the conductor of concern and every other conductor in the system during the same analysis run.

For magneto-static problems the analysis frequency is zero and so an unlimited theoretical penetration depth is considered as per equation 4.1. For AC time-harmonic magnetic problems, the analysis frequency is reflected by mak-

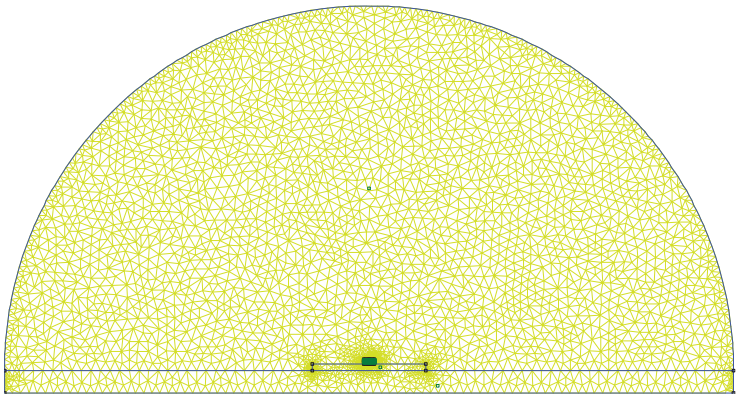

(a) A general meshed view of the FEMM magneto-static problem

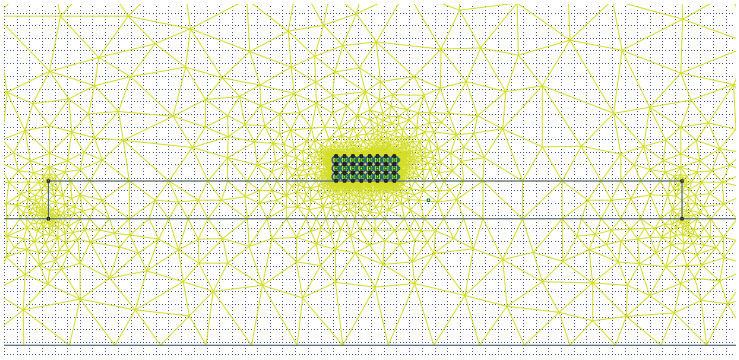

(b) A zoomed-in view of the same FEMM magneto-static problem

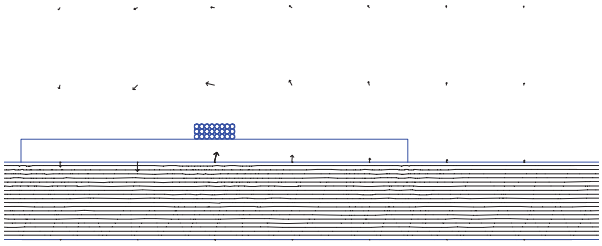

(c) A zoomed-in view of one post-processor analysis run for the same FEMM problem. The lines inside the core represent the magnetic flux lines (ϕ) or magnetic vector potential (A) while the arrows around the conductors represent the magnetic field intensity "H-field" vector plot

Figure 4.3: One of the magneto-static analysis runs for the FEMM model of the winding arrangement on iron core prototype

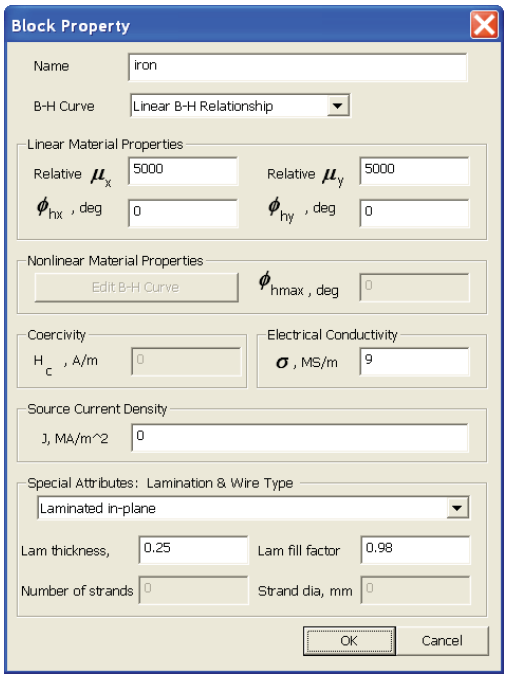

Figure 4.4: Iron block property details for AC time-harmonic magnetic analysis used for the core configuration

ing the element size defining a certain geometry, smaller than its corresponding magnetic field penetration depth (δ), not least when drawing the iron core. The same goal can be also achieved by making the mesh size of a certain geometrical area smaller than its corresponding (δ).

Sub-figure 4.5a below shows the outcome of magneto-static analysis while sub-figures 4.5b to 4.5h and figure 4.6 show the outcome of AC time-harmonic magnetic analysis of the winding on core arrangement prototype for the condensed wiring arrangement. Magnetic flux lines are shown inside the iron core. For magneto-static analysis the lines in the core represent the magnetic flux lines while in AC analysis the lines represent real part of the vector magnetic potential ($\mathbf{A}$), as a complex number of ($\mathbf{A}$) with both real and imaginary parts would result from the analysis.

The significance of using the *vector magnetic potential* ($\mathbf{A}$) in the analysis is that its line integral around any closed path equals the total magnetic flux passing through the area enclosed by that path as

$$\mathbf{\Phi} = \int_S \mathbf{B} \cdot \mathrm{d}\mathbf{s} \quad = \quad \int_S (\nabla \times \mathbf{A}) \cdot \mathrm{d}\mathbf{s} \quad = \quad \oint_C \mathbf{A} \cdot \mathrm{d}l \qquad [Wb] \tag{4.4}$$

The *vector magnetic potential* ($\mathbf{A}$) itself can be found knowing the current I which flows in a closed path in a conductor according to the equation [10]:

$$\mathbf{A} = \frac{\mu_0 I}{4\pi} \oint_C \frac{1}{\mathbf{R}} \mathrm{d}l \qquad [Wb/m] \tag{4.5}$$

where $\mathrm{d}l$ is the differential length element for the conductor and $\mathbf{R}$ is the distance from the conductor at which $\mathbf{A}$ is calculated.

The magnetic flux lines shown in figure 4.5 and 4.6 are generated by a stimulus current of 1 A in the last conductor of the condensed wiring arrangement, i.e. conductor number 24, for all the cases shown. The plot options are set to 19 contour plot lines with a lower limit of 0 [Wb] and an upper limit of 200 [μWb] in the case of magneto-static analysis, while in the AC magnetic analysis over 300 Hz a lower limit of -80 [μWb/m] and an upper limit of 200 [μWb/m] were considered for the real part plot of the *vector magnetic potential* ($\mathbf{A}$). The introduction of a minus sign to the lower limit of the ($\mathbf{A}$) plot is to include the contribution of the core losses in the analysis plot. Core losses result in complex

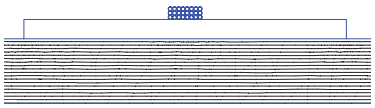

(a) Magnetostatic @ 0 Hz

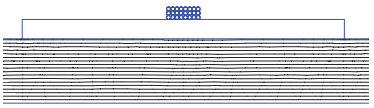

(b) AC time-harmonic magnetic @ 1 Hz

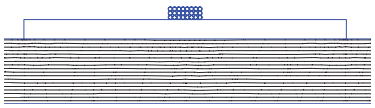

(c) AC time-harmonic magnetic @ 10 Hz

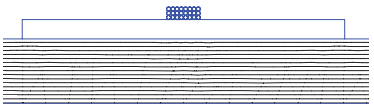

(d) AC time-harmonic magnetic @ 100 Hz

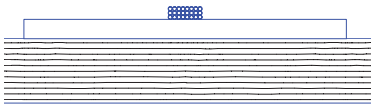

(e) AC time-harmonic magnetic 200 Hz

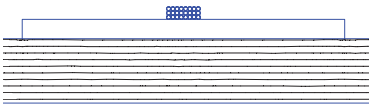

(f) AC time-harmonic magnetic @ 300 Hz

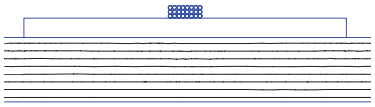

(g) AC time-harmonic magnetic @ 400 Hz

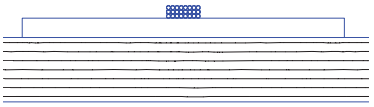

(h) AC time-harmonic magnetic @ 500 Hz

Figure 4.5: Zoomed-in post-processor views of magneto-static and AC time-harmonic magnetic FEMM analyses, for the 24 conductors on core - condensed arrangement - at different frequencies

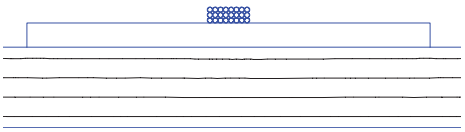

(a) AC time-harmonic magnetic @ 1 kHz

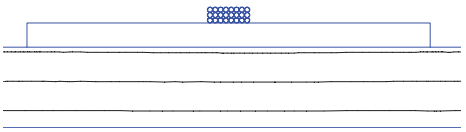

(b) AC time-harmonic magnetic @ 2 kHz

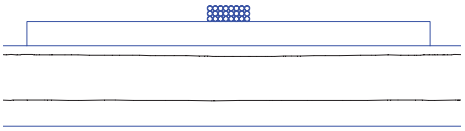

(c) AC time-harmonic magnetic @ 5 kHz

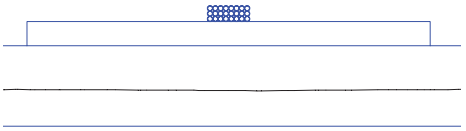

(d) AC time-harmonic magnetic @ 10 kHz

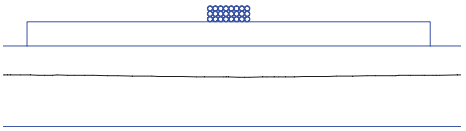

(e) AC time-harmonic magnetic @ 20 kHz

Figure 4.6: Zoomed-in post-processor views of AC time-harmonic magnetic FEMM analysis for the 24 conductors on core - condensed arrangement - at several “high” frequencies

number solution for (**A**) and a decrease of the resultant absolute value of (**A**) as frequency increases.

In general terms, the magnetic field flux lines are highest in magnitude and more intense within the upper part of the core, closer to the current-carrying conductor, for each analysis case. Flux lines tend to vanish when they approach the prescribed zero potential boundary condition assigned to the bottom line of the core. Figure 4.7 below shows that for the magneto-static analysis case the top 50 percent value of the magnetic flux lines exist within the upper half of the core.

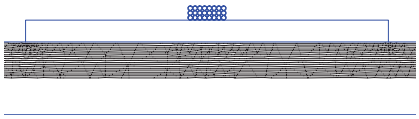

Figure 4.7: Zoomed-in post-processor views of magneto-static FEMM analysis, showing the top 50% of magnetic field flux lines

From sub-figure 4.5a to 4.5f we note that in the magneto-static case and also at "low" frequencies, the iron core acts as an attractive medium for the magnetic field flux lines to pass through, in order to complete their path, linking the current-carrying conductor to the core. This is due to the high permeability of the ferro-magnetic core at low frequencies, and the lamination thickness being smaller than the corresponding penetration depth. This contributes to higher values of inductance at low frequencies.

As frequency increases for AC time-harmonic magnetic problems, the ferro-magnetic iron core tends to loose this attractive feature of containing all the magnetic field flux lines within. This is due to the associated core losses and the nonlinear behaviour of the iron magnetic permeability (μ_r) that affects the penetrtaion depth of the magnetic field in iron at higher frequencies. This will cause the inductance to decrease with the frequency increase as inductance is magnetic flux divided by current as:

$$L = \frac{\phi}{i} \tag{4.6}$$

Due to skin depth effect, the higher the frequency the less magnetic flux lines tend to penetrate the core laminations. So the challenge is to predict, on a case-by-case basis, at which point/range the frequency starts to influence the inductance value and to quantify how much that would be compared to the dc or "low" frequency value for a certain geometry and material characteristics. Here the ferro-magnetic core plays a very important role since iron generally has the lowest penetration depth among other elements and metals, as can be seen in figure 4.1, due to the fact that it has high magnetic permeability (μ_r) values and the penetration depth is inversely proportional to the magnetic permeability as per equation 4.1.

This explains why iron cores of high permeability values are effective only in dc and "low" frequency range, while their characteristics degrade substantially when considering "high" frequency operation. In our case of the winding-on-core prototype and according to the FEMM analysis, a substantial decrease of the inductance value to 15% lower than its corresponding dc value, can be observed within the range of 300-400 Hz.

This frequency range can vary for different lamination thicknesses and for iron additives and composites forming the lamination, but can still be expected to fall within a frequency range of few 100's of Hz to few kHz. One of the thinnest iron core laminations observed is 100 [μm] and the range of relative permeability (μ_r) values considered are from 1000 to 9000 [11].

Flux lines inside the core will gradually decrease beyond this critical frequency range or "knee frequency" untill eventually at very high frequencies they tend to close their paths in the air without the need to pass through the iron core. Iron will effectively behave like air for very high frequency magnetic fields.

4.1 How the *Inductive Coupling Matrix* is Created?

For a given frequency, the FEMM model of the winding-on-core prototype has been run number of times equal to the number of conductors in the wiring

arrangement. The reason being is that the stimulus current has been assigned to one conductor at a time to find the self-inductance and the mutual-inductances due to that stimulus, then, in the next run, the stimulus current is shifted to the neighbouring conductor in the multi-conductor system. For each run this gives a number of results equal to the number of conductors in the system, i.e. 24 results in our case (1 self-inductance and 23 mutual-inductance values). This is repeated automatically until eventually creating a matrix system of 24×24 result values, in which the main diagonal elements represent the self-inductance and the off-diagonal elements represent the mutual-inductance values with symmetry and redundancy around the main diagonal.

The self-inductance for the conductor of stimulus is calculated for each analysis run, according to the formula:

$$\mathbf{L}_{self} = \frac{\int(\mathbf{A} \cdot \mathbf{J}) \cdot \mathrm{d}V}{i^2} \tag{4.7}$$

Where "$\mathbf{A}$" is the magnetic vector potential in [Wb/m](or can also be regarded as magnetic flux ($\mathbf{\Phi}$ in [Wb]), "$\mathbf{J}$" is the current density in $[A/m^2]$, "dV" is a volumetric differential element in $[m^3]$ and "i" is the stimulus current through the conductor in [A]. The integrand part in equation 4.7 is configured as a block integral which can be carried over a selection area in the FEMM post-processor. This makes it possible to calculate the self-inductance for known values of current [23].

Mutual inductance between the conductor of stimulus and every other conductor in the system is calculated according to the relation:

$$\mathbf{L}_{mutual} = \frac{\int(\mathbf{A_1} \cdot \mathbf{J_2}) \cdot \mathrm{d}V_2}{i_1 \cdot i_2} \tag{4.8}$$

Where "$\mathbf{A_1}$" is the magnetic vector potential produced by the conductor of stimulus (the source conductor), "$\mathbf{J_2}$" is the current density resulted in the other conductor in the system (passive conductor with no stimulus), "$\mathrm{d}V_2$" is a volumetric differential element of the other conductor in $[m^3]$, "i_1" is the current of stimulus in the source conductor, and "i_2" is the resulting induced current in the other conductor in the system.

Considering that the total current in any coil is represented by the number of turns times the current in a single turn of the coil, which is also equivalent

to the current density times the coil's cross-sectional area. This is expressed, in mathematical notation, for the other conductor in our system as:

$$n_2 \cdot i_2 = J_2 \cdot a_2$$

Solving for the other conductor's current density over current ($\frac{J_2}{i_2}$) in equation 4.8, we have:

$$L_{mutual} = (\frac{n_2}{a_2 \cdot i_1}) \cdot \int \mathbf{A_1} \cdot \mathrm{d}V_2 \tag{4.9}$$

The integrand part in equation 4.9 is defined as a block integral that can be carried over a selection area in the FEMM post-processor. This enables the calculation of mutual-inductance for known values of source current, number of turns and cross-sectional area over which the integration is performed [23].

Figures 4.8 to 4.16 below show 3D plots and 2D images for the *Inductive Coupling Matrix* resulted from the FEMM analysis under different frequency values ranging from dc (0 Hz) up to 2 kHz. For AC analysis the resulting value for the inductance will be a complex number. The imaginary component is expressing the core losses. In the above mentioned plots the absolute values of the complex-numbered inductance have been considered.

4.2 Complex-Numbered Inductance Concept

From the relationship in 4.6 when the magnetic flux lags the current in time-harmonic problems, due to core losses of eddy currents and hysteresis, it will result in complex-numbered inductance of which the imaginary part is a lumped representation of the core losses.

When L is the complex-numbered inductance, it is represented as:

$$L = L_r - jL_i \tag{4.10}$$

where L_r is the real part of the inductance, L_i is the imaginary part and j=$\sqrt{-1}$ is the imaginary operator.

Considering the impedance of inductance to be: $Z(\omega) = j\omega L$, where ω is the angular frequency in [radians/second]. We will have:

$$Z(\omega) = j\omega L_r + \omega L_i \tag{4.11}$$

The imaginary part of complex-numbered inductance contributes to a real part of the frequency-dependent impedance Z(ω), associated with core losses. One could interpret the (ωL_i) term as a frequency-dependent resistance which will be used later to develop a circuit model for the core losses along a frequency sweep. The real part of the inductance contributes to the imaginary part of Z(ω) which is associated with inductive energy storage.

Table 4.2 show some key results out of the *Inductive Coupling Matrices* run at various frequencies. It shows the maximum, the minimum and the mean value of the matrix elements. It also shows the difference in absolute value between the maximum and minimum inductance in the matrix, for each frequency. As well it shows the coupling factor for each run which is defined as the average inductance value divided by the maximum (self-inductance) value.

f [Hz]	$L_{max}[\mu H]$	$L_{min}[\mu H]$	$L_{average}[\mu H]$	ΔL [nH]	coupling factor
DC (0 Hz)	26.76	26.67	26.71	93	0.9978
10 Hz	26.76	26.66	26.70	93	0.9978
100 Hz	26.15	26.06	26.09	92	0.9978
200 Hz	24.54	24.45	24.49	88	0.9978
300 Hz	22.46	22.38	22.41	83	0.9977
400 Hz	20.33	20.25	20.28	79	0.9976
500 Hz	18.38	18.31	18.34	75	0.9975
1 kHz	12.24	12.17	12.20	66	0.9966
2 kHz	8.12	8.05	8.08	66	0.9949

Table 4.2: Key results out of *Inductive Coupling Matrices* for different frequency values

By investigating figures 4.8 to 4.16, and table 4.2 above, we observe the following:

(i.) The matrix elements maintain the same behaviour and have similar patterns in all frequency runs, i.e. the highest values are for self-inductances which lie in the main diagonal and then followed by mutual inductances between adjacent conductors on the same layer or at different layers; First off-diagonal elements above and below the main diagonal represent adjacency on the same layer (symmetry and redundancy around the main

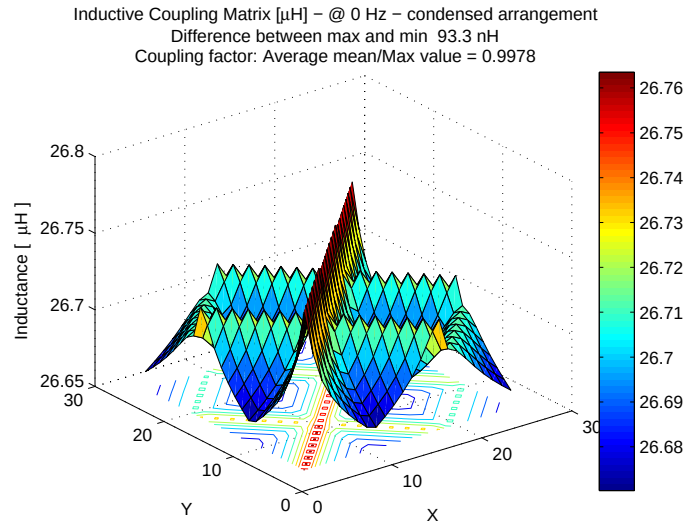

(a) 3D plot of the *Inductive Coupling Matrix* at DC (0 Hz)

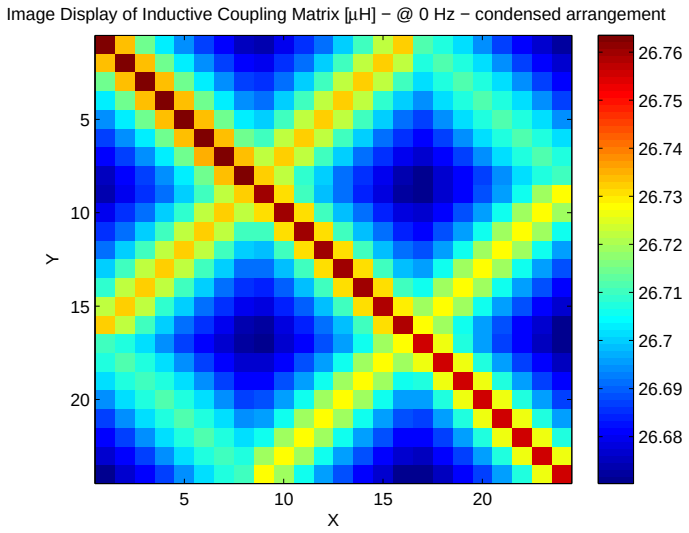

(b) 2D image of the *Inductive Coupling Matrix* at 0 Hz

Figure 4.8: Linear scale representation of *Inductive Coupling Matrix* run at 0 Hz frequency for the system of 24 conductors on iron core - condensed arrangement

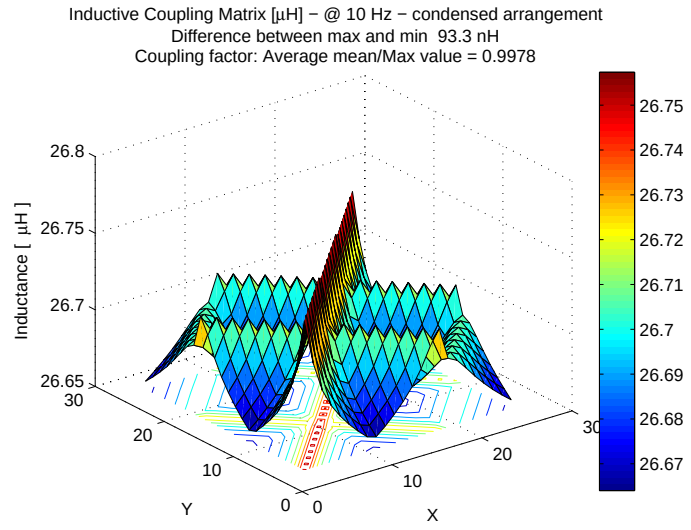

(a) 3D plot of the *Inductive Coupling Matrix* at 10 Hz

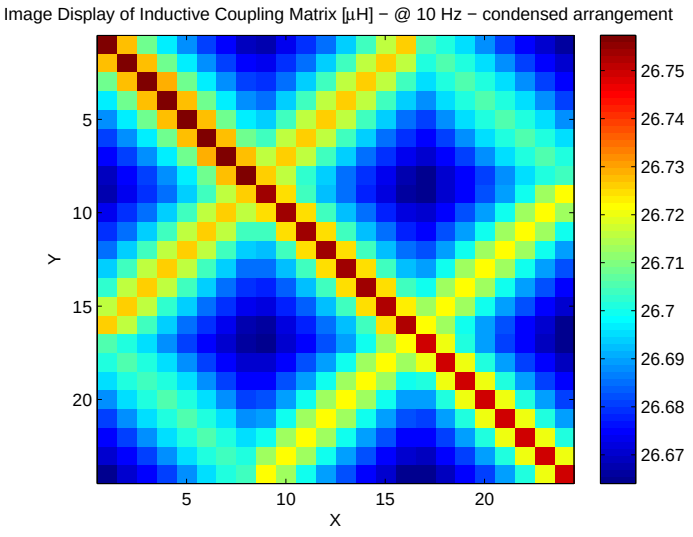

(b) 2D image of the *Inductive Coupling Matrix* at 10 Hz

Figure 4.9: Linear scale representation of *Inductive Coupling Matrix* run at 10 Hz frequency for the system of 24 conductors on iron core - condensed arrangement

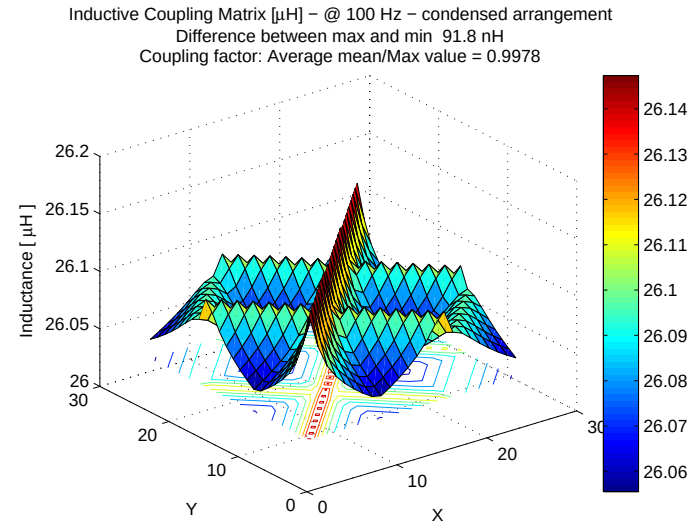

(a) 3D plot of the *Inductive Coupling Matrix* at 100 Hz

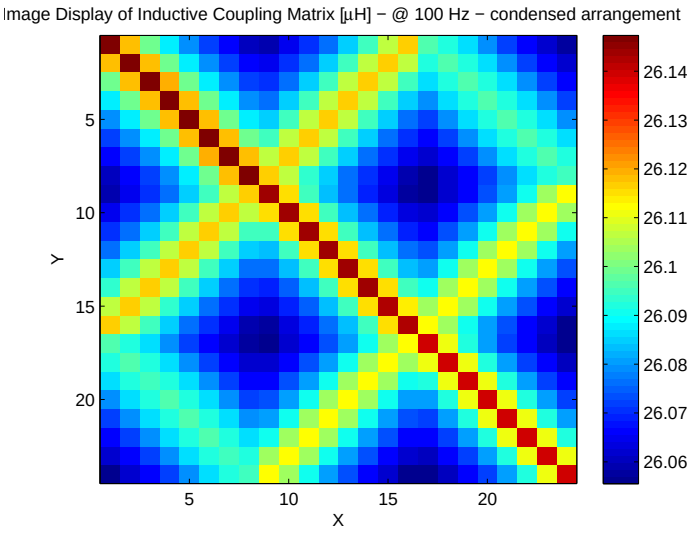

(b) 2D image of the *Inductive Coupling Matrix* at 100 Hz

Figure 4.10: Linear scale representation of *Inductive Coupling Matrix* run at 100 Hz frequency for the system of 24 conductors on iron core - condensed arrangement

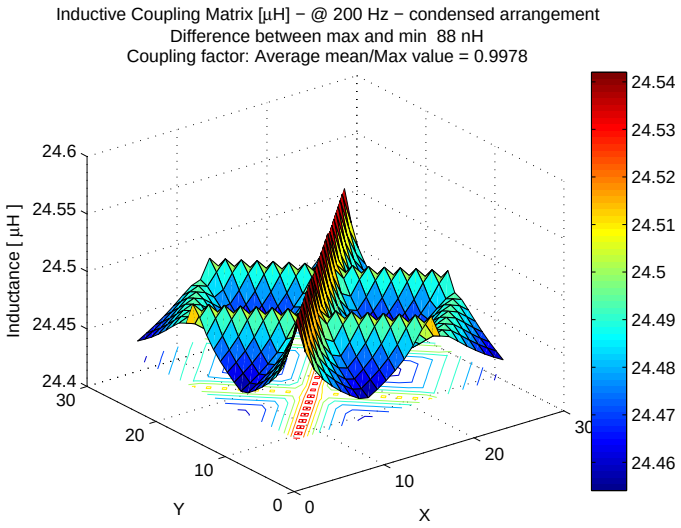

(a) 3D plot of the *Inductive Coupling Matrix* at 200 Hz

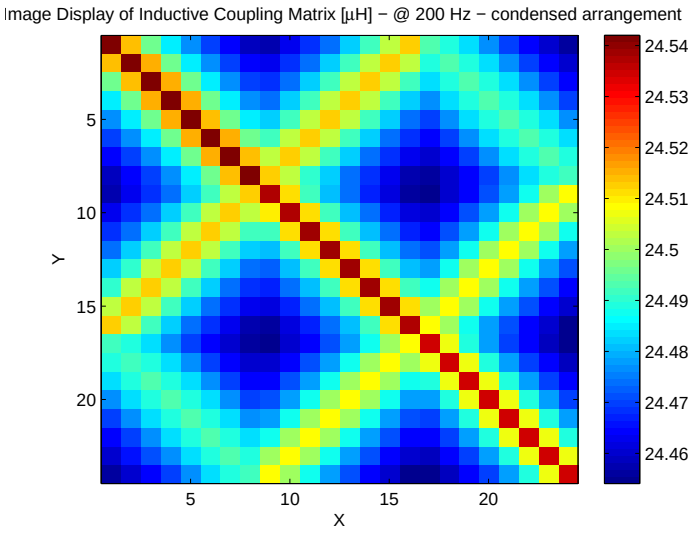

(b) 2D image of the *Inductive Coupling Matrix* at 200 Hz

Figure 4.11: Linear scale representation of *Inductive Coupling Matrix* run at 200 Hz frequency for the system of 24 conductors on iron core - condensed arrangement

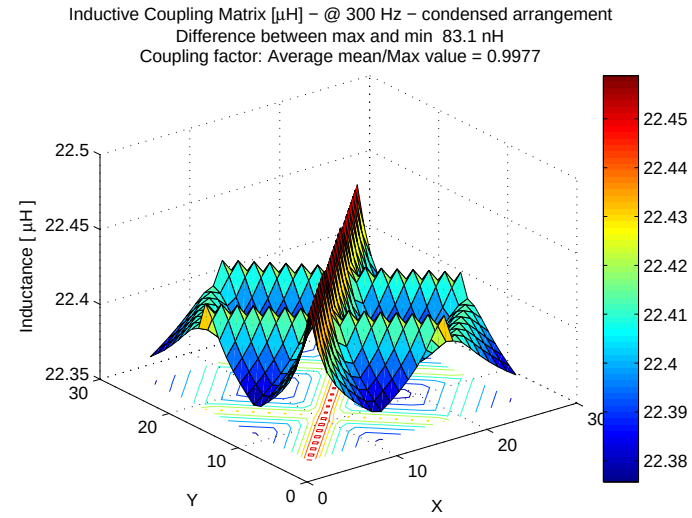

(a) 3D plot of the *Inductive Coupling Matrix* at 300 Hz

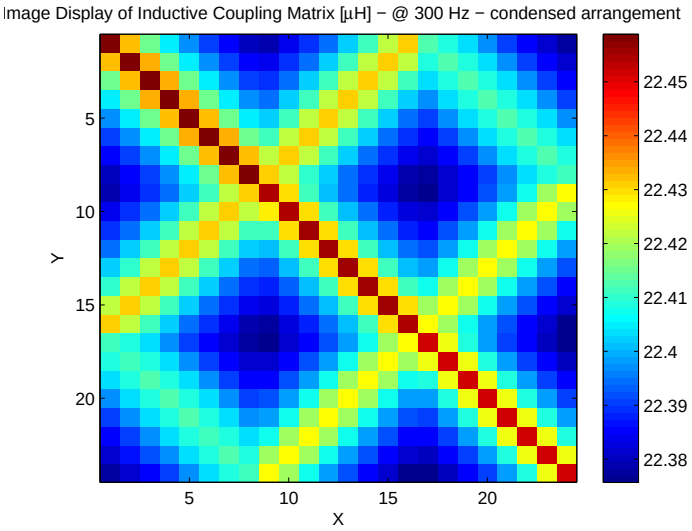

(b) 2D image of the *Inductive Coupling Matrix* at 300 Hz

Figure 4.12: Linear scale representation of *Inductive Coupling Matrix* run at 300 Hz frequency for the system of 24 conductors on iron core - condensed arrangement

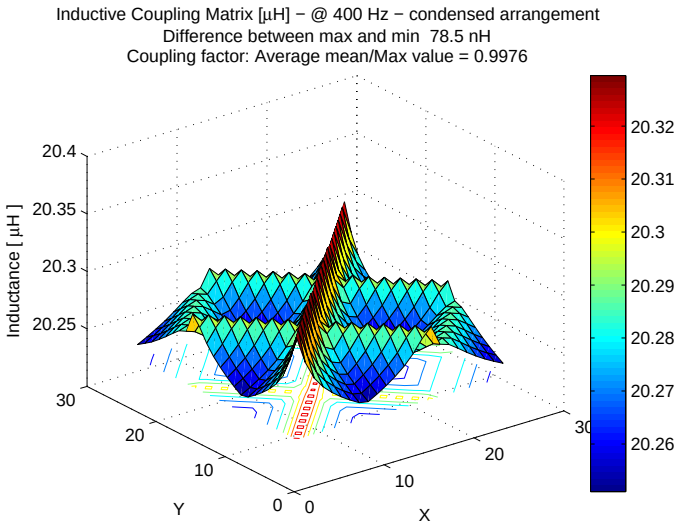

(a) 3D plot of the *Inductive Coupling Matrix* at 400 Hz

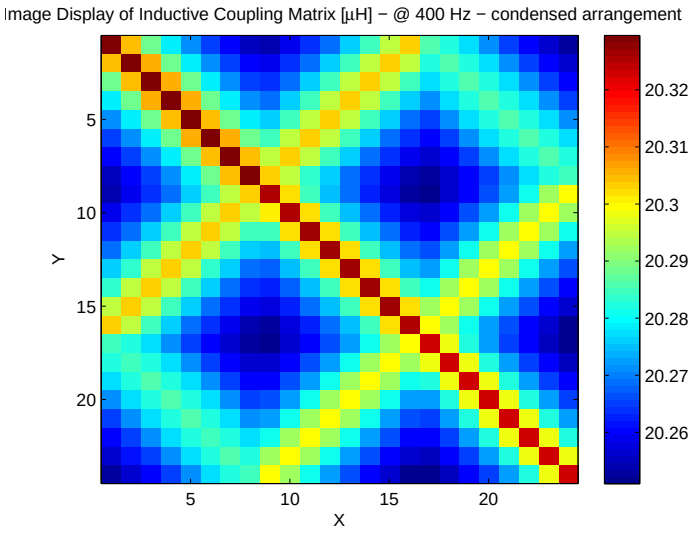

(b) 2D image of the *Inductive Coupling Matrix* at 400 Hz

Figure 4.13: Linear scale representation of *Inductive Coupling Matrix* run at 400 Hz frequency for the system of 24 conductors on iron core - condensed arrangement

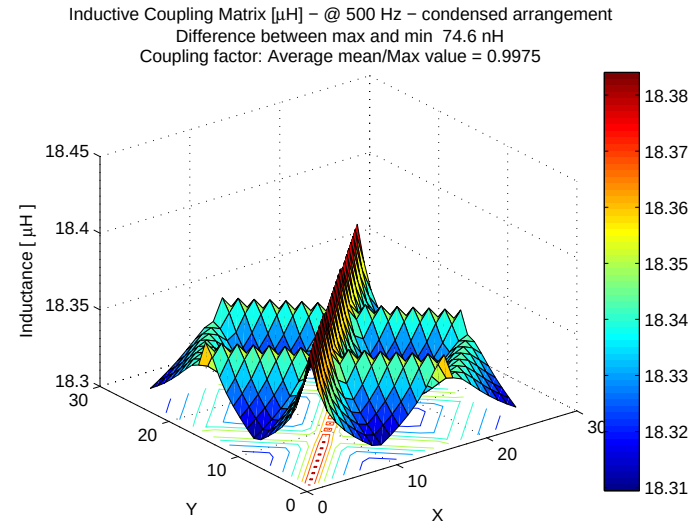

(a) 3D plot of the *Inductive Coupling Matrix* at 500 Hz

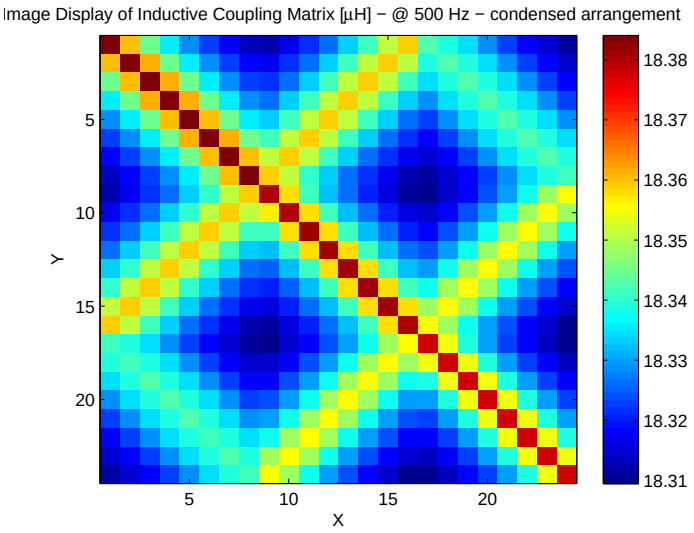

(b) 2D image of the *Inductive Coupling Matrix* at 500 Hz

Figure 4.14: Linear scale representation of *Inductive Coupling Matrix* run at 500 Hz frequency for the system of 24 conductors on iron core - condensed arrangement

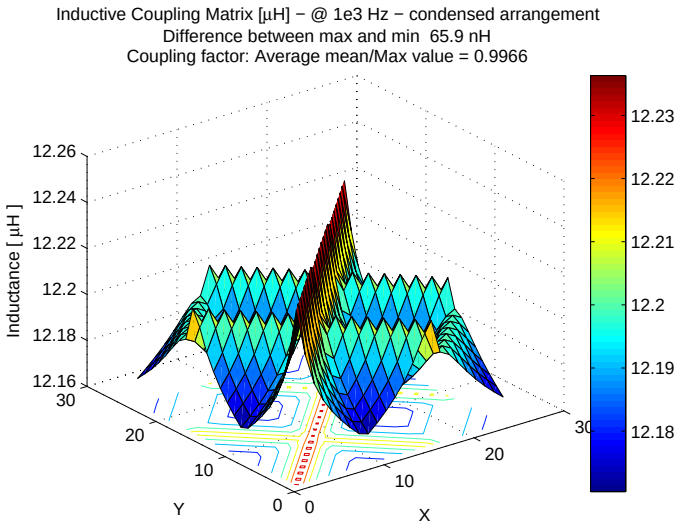

(a) 3D plot of the *Inductive Coupling Matrix* at 1 kHz

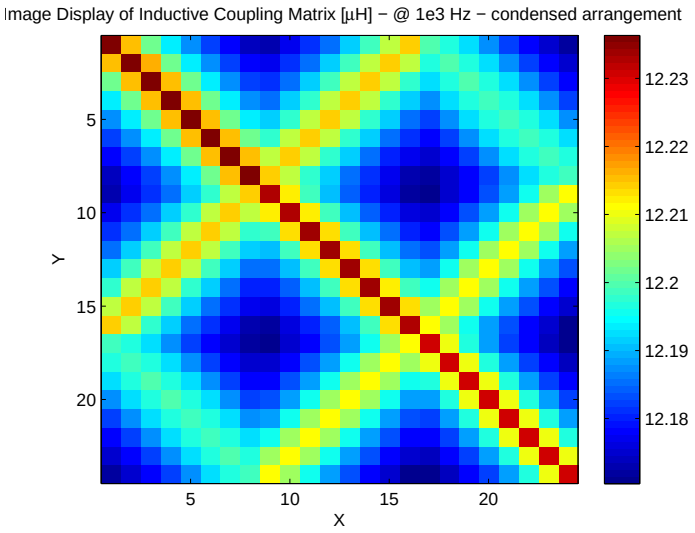

(b) 2D image of the *Inductive Coupling Matrix* at 1 kHz

Figure 4.15: Linear scale representation of *Inductive Coupling Matrix* run at 1 kHz frequency for the system of 24 conductors on iron core - condensed arrangement

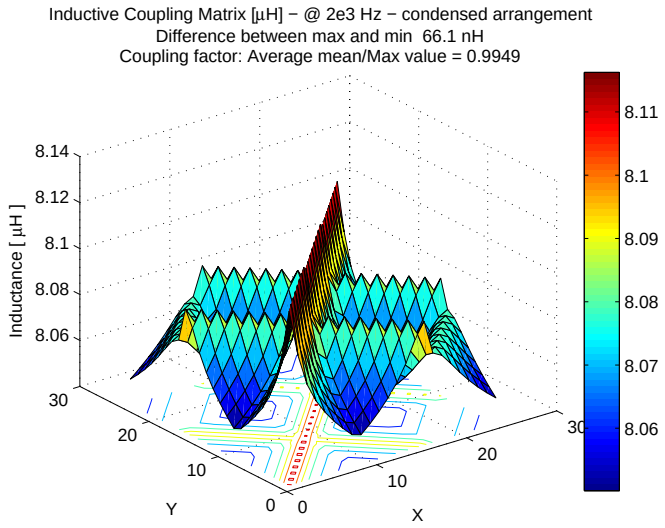

(a) 3D plot of the *Inductive Coupling Matrix* at 2 kHz

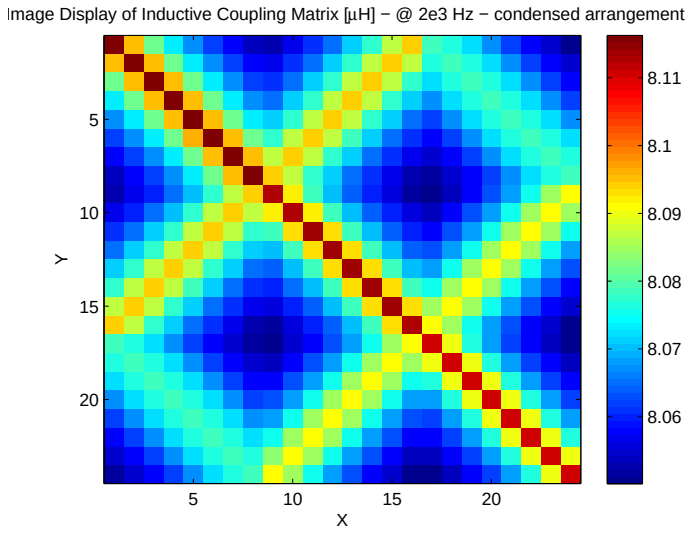

(b) 2D image of the *Inductive Coupling Matrix* at 2 kHz

Figure 4.16: Linear scale representation of *Inductive Coupling Matrix* run at 2 kHz frequency for the system of 24 conductors on iron core - condensed arrangement

diagonal) while the two lines perpendicular to the main diagonal represent adjacancy between first and second layers for one line, and between second and third layers for the other.

(ii.) Unlike the previously studied *Capacitive Coupling Matrix*, the *Inductive Coupling Matrix* has a smooth transition concerning the absolute values of adjacent elements.

(iii.) The coupling factor for all frequency runs was high and averaged to 0.9973 which makes it fair to conclude a very high coupling factor for an orderly-wound condensed wiring arrangement.

(iv.) An interesting obesrvation was the substantial decrease in absolute values of the *Inductive Coupling Matrix* elements when going from dc analysis to 2 kHz, compared to the difference between maximum and minimum elements in the matrix (ΔL); As it can be seen, for example, for $L_{average}$ which has dropped from 26.71 [μH] at dc to 8.08 [μH] at 2 kHz, with a 70% decrease, while the correponding (ΔL) has dropped from 93 [nH] to 66 [nH] with a 29% decrease.

From the above, and despite the limitation of running only time-harmonic magnetic field analysis with no account for electromagnetic fields, we conclude that for simplification purposes it is sufficient to calculate the inductance of a single conductor in the arrangement, and then consider a high coupling factor between the conductors of the orderly-wound condensed wiring arrangement.

4.3 Single Turn Analysis

As per the observations and conclusions obtained from the *Inductive Coupling Matrix* by studying self-inductance and mutual inductances for each conductor in the multi-conductor system, the attennttion is focused now on studying the inductance and resistance behaviour of a single turn, in the 24-turn winding-on-core prototype, along a frequency sweep.

The objective is to make use of the results found in the previous section in order to have a clearer picture about the frequency impact on basic properties on the turn level, to simplify the calculations with fair assumptions and develop a corresponding circuit model covering the frequency range of interest. A circuit model representing the turn's frequency-dependent inductance and re-

sistance can be used later, along with the capacitance network (see figure 3.12) for building up the transmission line model of the winding. Transmission line model will be extended to the machine case for studying conducted emissions in the electric drive.

The same FEMM model which has been used previously to generate the *Inductive Coupling Matrix* is used here along the conducted-emission frequency range. The simplification of extracting the properties of only one conductor from the model has been implemented. These properties include self inductance with its magnitude, loss angle, real and imaginary parts as the inductance becomes a complex number for time-harmonic magnetic analyses. As well resistive, hysteresis and eddy current losses in the copper conductor, the iron core and the dielectric Bobbin. Figure 4.17 below show some key results out of this simplified analysis.

By comparing the loss angle and the imaginary inductance behaviour along the frequency sweep, we notice that the loss angle starts from zero at dc and increases with the frequency until it reaches a maximum peak of 45° at 1 kHz, after which it starts to decrease again, while the imaginary inductance part has a similar behaviour, however the peak of 11 [μH] occurs earlier at 500 Hz. This is due to the decrease in magnitude of the complex-numbered inductance after what is known as "knee frequency" which is in our case falls between 300 and 500 Hz. This can be seen clearly in the logarithmic scale plot of the inductance magnitude against frequency in figure 4.18.

Magnitude decrease of inductance is related to lower skin/penetration depth compared to "half" the given dimension of a lamination sheet in the iron core. For a thickness of 250 μm for one lamination, a change in the magnetic field flux pattern is expected to happen when the penetration depth becomes less than half the dimension, as magnetic field is expected to penetrate the lamination from both sides. A change of the flux pattern will affect mainly the inductance.

For the given 250 μm thickness of an iron lamination, and for several common permeability values (μ_r), the penetration depth corresponding to 125 μm occurs at following frequencies as per Table 4.3

Figure 4.19 show different types of losses associated with a single turn in the 24-turn wiring arrangement. For the iron core, sub-figure 4.19a, we notice that the dominant type of losses along the frequency sweep are hysteresis and eddy current losses which will reflect on the inductance value. The resistive losses in the iron are negligible. Losses in the iron core are generally negligible

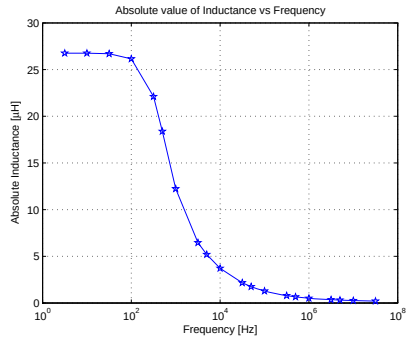

(a) Absolute value of inductance vs frequency

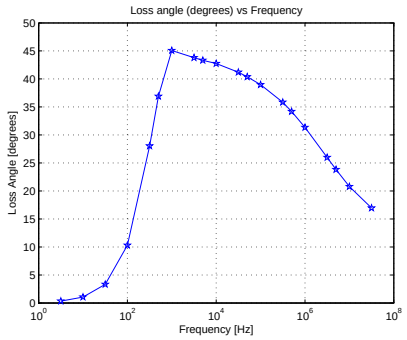

(b) Loss angle vs frequency

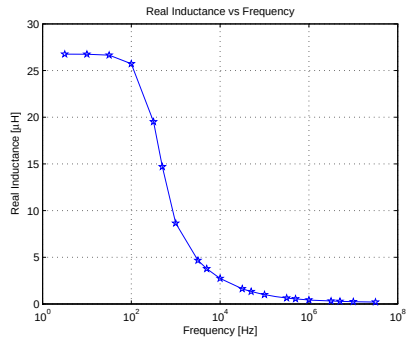

(c) Real inductance part vs frequency

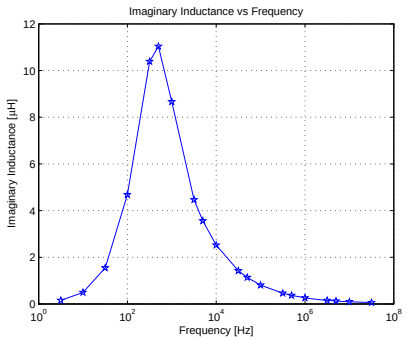

(d) Imaginary inductance part vs frequency

Figure 4.17: Complex inductance components along the frequency sweep extracted from the FEMM model of a single conductor in a 24-conductor winding-on-core prototype

Iron relative permeability (μ_r)	Penetration depth [μm]	Frequency [Hz]
1000	126	1600
3000	125	540
5000	126	320

Table 4.3: Frequency occurrence of a penetration depth corresponding to "half" the lamination thickness for different relative permeability values μ_r

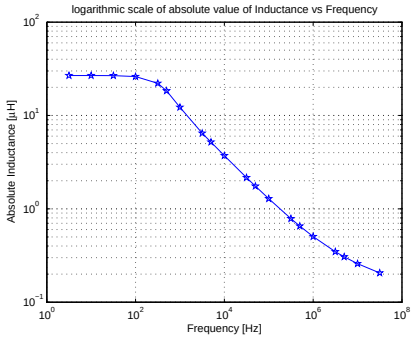

Figure 4.18: A logarithmic scale of absolute value of the complex-numbered inductance in [μH] vs frequency in [Hz]

at dc and very low frequency until they exceed the 20 [mW] limit around 316 [Hz] according to our analysis, as can be seen clearly in figure 4.20.

For copper conductor losses 4.19b we notice that resistive losses are the dominant ones while hysteresis and eddy current losses are negligible. This is mainly due to relatively high electrical conductivity and diamagnetic properties of the copper. Copper losses are significant at DC level with a value of 8.7 [mW] in the copper conductor and maintains constant level along low frequency up to the limit where skin depth in the copper becomes significant, where they will increase substantially. This is observed to be around 50 [kHz] where losses in one conductor reach the limit of 9 [mW] as can be seen in figure 4.21. At 50 [kHz] the penetration depth in copper is equivalent to 0.296 [mm], as per equation 4.1, which roughly accounts for half the copper conductor dimension of 0.589 [mm] in diameter.

4.4 Single Turn Model along a Frequency Sweep

In order to develop a circuit model for a single turn along a frequency sweep of interest, three main quantities need to be investigated:

(i.) The inductance value of the winding at dc and very low frequencies, when and how its magnitude will be substantially affected by frequency increase.

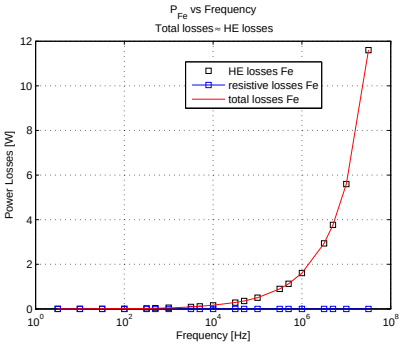

(a) Iron core losses vs frequency

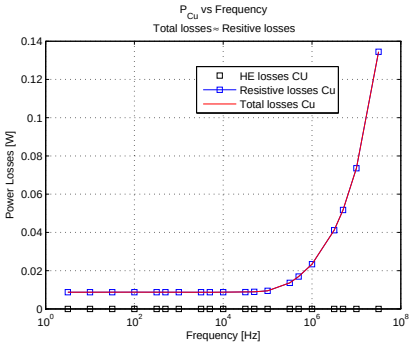

(b) Copper conductor losses vs frequency

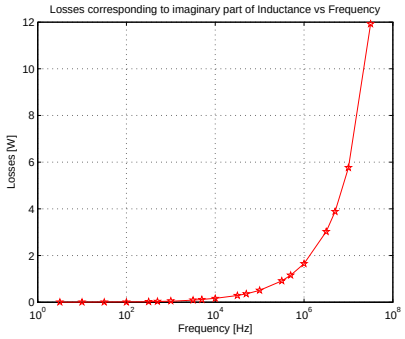

(c) Losses corresponding to imaginary inductance part (ωL_i) vs frequency

Figure 4.19: Different types of losses associated with a single turn in a 24-turn winding-on-core prototype, along a frequency sweep

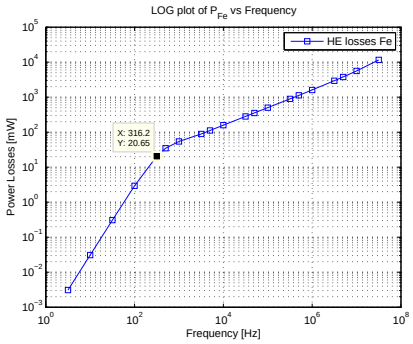

Figure 4.20: A logarithmic scale of hysteresis and eddy current iron core losses in [mW] vs frequency in [Hz]

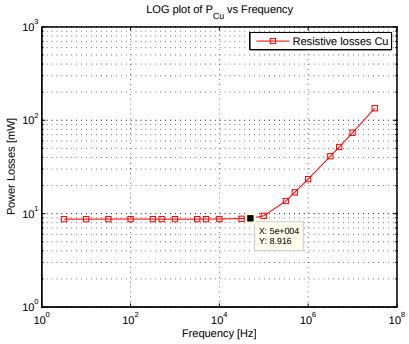

Figure 4.21: A logarithmic scale of the resistive losses in the copper conductor in [mW] vs frequency in [Hz]

(ii.) The resistive copper losses at dc and low frequencies and then at which frequency theses losses increase significantly.

(iii.) Core losses and at which frequency they become significant and how would they develop with the frequency increase.

In order to do that we make a table, and record the above mentioned quantities for dc and very low frequency, and then for each decade of frequency increase as it shows in table 4.4.

f	r_{Cu} [mΩ]	r_{core} [mΩ]	L [μH]
DC (0 Hz)	8.7	0	26.76
10 Hz	8.7	$3 \cdot 10^{-2}$	26.76
316 Hz	8.7	21	22.11
1 kHz	8.7	54	12.24
10 kHz	8.7	159	3.72
100 kHz	9.5	508	1.28
1 MHz	23.4	1648	0.50
10 MHz	73.6	5767	0.26
30 MHz	134.5	11 925	0.21

Table 4.4: Key results out of a single turn analysis along a frequency sweep

To quantify the change and relate it to the frequency increase, two critical frequencies are observed; one is related to both core losses and inductance magnitude, and the other is related to resistive copper losses.

The frequency related to the resistive copper losses is determined by the skin depth in the material compared to half the given dimension of the copper conductor, and also the resolution of frequency points taken to develop the model. In our case the frequency corresponding to the skin depth in copper is 50 kHz but since the resolution is taken every one decade after the 1 kHz limit, the critical frequency corresponding to copper losses becomes 100 kHz for the sake of developing the model.

The frequency related to both inductance magnitude and core losses (f_{cr1}) is determined by the skin depth in the fundamental magnetic core unit in comparison to "half" its dimension. In our case $f_{cr1} = 316$ Hz corresponding to half an iron lamination sheet of a thickness 250 [μm] and a relative magnetic permeability ($\mu_r = 5000$). Obviously this frequency can be shifted according to the geometrical dimensions and material characteristics of the basic core unit

used; whether it is a bulk iron core, an iron lamination sheet or even a small tiny magnetic particle of magnetic powder used in SMC and SM^2C. The general trend would be the smaller the dimension of the basic core unit, the higher the critical frequency (f_{cr1}) would be.

The selection of the first critical frequency (f_{cr1}) is chosen as per the maximum core losses for the minimum change in the inductance value. Referring to equation 4.10 defining the complex inductance concept, f_{cr1} is chosen according to the relation:

$$f_{cr1} = max(\frac{R_{core}}{\mid L \mid}) = max(\frac{\omega L_i}{L_r}) \tag{4.12}$$

where L_r is the real part & L_i is the imaginary part of the complex-numbered inductance resulting from the FEMM analysis. f_{cr1} is physically related to the magnetic field penetration of the iron core.

For the sake of developing the model, it is recommended to choose (f_{cr1}), as close as possible to the penetration depth frequency in the basic core unit, and not to be governed by the frequency resolution considered when developing the model, even if it falls beyond the 1 kHz limit. Unlike resistive copper losses, which will occur further in the frequency scale and will be offset by the core losses, critical frequency related to inductance and core losses (f_{cr1}) tends to occur in low frequency range, i.e. between few 100's Hz to few kHz.

Later we quantify the factors contributing to the magnitude change of the three basic quantities when stepping from each key frequency to the next. we make table 4.5.

Starting from the third frequency step at the critical frequency (f_{cr1}), the complex-numbered inductance will be represented by two passive elements in the circuit model; an inductance and a resistance (see figure 4.22). The real part of the complex-numbered inductance (L_r) is expressed by an inductive energy storage element of inductance 22.11 μH, while the core losses are lumped and expressed by a resistive element of a 21 mΩ resistance corresponding to ωL_i, where L_i is the imaginary part of the complex-numbered inductance as was shown in equations 4.10 and 4.11.

Then from the next decade point in the frequency scale and up to the highest (1 kHz – 10 MHz), we relate the real inductance part and core losses to their corresponding values at (f_{cr1}), our starting limit. This is done by

Frequency steps	Factors for (r_{cu}) change	Factors for (r_{core}) change	Factors for (L) change
DC (0 Hz) – 10 Hz	1	∞	1
10 Hz – 316 Hz	1	700	0.8262
316 Hz – 1 kHz	1	2.5714	0.5536
1 kHz – 10 kHz	1	2.9444	0.3039
10 kHz – 100 kHz	1.0920	3.1950	0.3441
100 kHz – 1 MHz	2.4632	3.2441	0.3906
1 MHz – 10 MHz	3.1453	3.4994	0.5200
10 MHz – 30 MHz	1.8274	2.0678	0.8077

Table 4.5: Quantification factors of key parameters corresponding to frequency steps - single turn analysis

proposing two constants “a” and “b”; “a” to be multiplied by the resistive part expressing core losses magnitude increase, and “b” to be divided by the inductive part expressing the inductance magnitude decrease for each decade increase in frequency. Constants “a” and “b” are shown in table 4.6.

Frequency-decades	Factors for (r_{core}) increase	Factors for (L) decrease	Reciprocal of (L) decrease factors
316 Hz – 1 kHz	2.5714	0.5536	1.8064
1 kHz – 10 kHz	2.9444	0.3039	3.2906
10 kHz – 100 kHz	3.1950	0.3441	2.9061
100 kHz – 1 MHz	3.2441	0.3906	2.5602
1 MHz – 10 MHz	3.4994	0.5200	1.9231

Table 4.6: Quantification factors for core losses increase and inductance magnitude decrease for 5 decades of frequency - single turn analysis

Factor “a” is then taken to be the average of all (r_{core})-icrease factors for successive frequency decade shifts (a = 3.10 in our case). Factor “b” is chosen according to the relation:

$$b = \frac{10}{a} \tag{4.13}$$

So that we can add one additional RL branch for each decade of frequency. Factor "b" from equation 4.13 = 3.23, which is not far from the reciprocal average of FEMM result for inductance decrease (2.50). The deviation in inductance magnitude decrease will be compensated by the frequency term in the impedance which will be relatively high.

The next step will be to multiply the resistive part representing the core losses with the factor "a", and to divide the inductive part by the factor "b", in the circuit model for each successive branch. The resulting model will be a ladder of RL parallel-connected branches where the number of branches indicates how many frequency decades the model covers. The model acts like concentric shells in which the inner most represents the lowest frequency and the outer most the highest. The model is shown in figure 4.22 below:

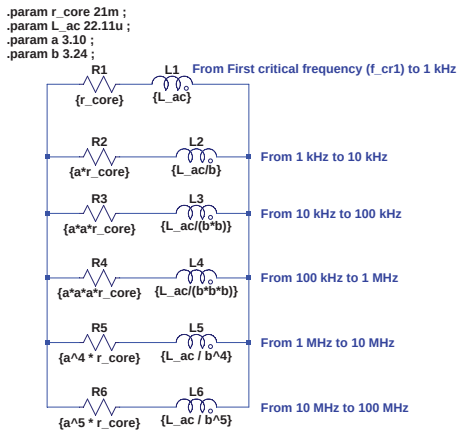

Figure 4.22: A ladder model for a single turn's ac inductance and core losses covering a frequency sweep starting from first critical frequency ($f_{cr1} = 316$ Hz) up to 100 MHz

The reason why we have used equation 4.13 in deriving factor "b" from "a" is that we are interested in having the *corner frequency* ω_k for each RL branch to

be one decade, in the frequency scale, further from the previous one, according to the relation:

$$\omega_k = \frac{R_k}{L_k} = 10 \cdot \omega_{k-1} \tag{4.14}$$

where ω_k is the *corner frequency* in [rad/sec] for the k^{th} RL-branch in the system, and represents a *zero* of that branch in the pole-zero plot. k=1,2,...,n where n is the number of RL-branches. Figure 4.23 and 4.24 show the pole-zero plot and the bode plot, respectively, for the six RL parallel-connected branches of the system. Please note that for bode plot the decibel calculation for magnitude on the y-axis is calculated according to the relation $20 \cdot log_{10} \mid Z(jw) \mid$, where $\mid Z(jw) \mid$ is the frequency response for the branch.

Notice the occurrence of corner frequency for each successive branch further in the frequency than its preceding one. The higher resistance value contributes to higher low-frequency response and the lower inductance value for lower high-frequency response. The response of the equivalent combination of all the branches besides the response of the branches themselves are shown in figures 4.25 and 4.26

We notice that the equiuvalent combination of the 6 branches is in a good agreement with the high-frequency behaviour for each branch after its corresponding *corner frequency*. In the highest frequency range it agrees with the behaviour of the outer most RL branch, the purple line representing $\mathbf{Z}_{\{\mathbf{10\ MHz \leftrightarrow 100\ MHz}\}}$. However, we see that there is a clear difference between the equivalent system of branches and the original branch $\mathbf{Z}_{\{\mathbf{316\ Hz \leftrightarrow 1\ kHz}\}}$ at the low frequency range before its *corner frequency*.

A need to compensate for that rises, by introducing compensation factors for the resistance and inductance parts in the first RL branch $\mathbf{Z}_{\{\mathbf{316\ Hz \leftrightarrow 1\ kHz}\}}$ to account for the deviation of the equivalent branch system in the dc and low-frequency region [12].

Following the approach presented in [30], for modelling skin effect in air-surrounded conductors using passive circuit elements, and extending that to our case for the frequency range of interest, we can represent each branch in the prallel combination as:

$$\mathbf{Z_k} = R_k + j \cdot X_k \tag{4.15}$$

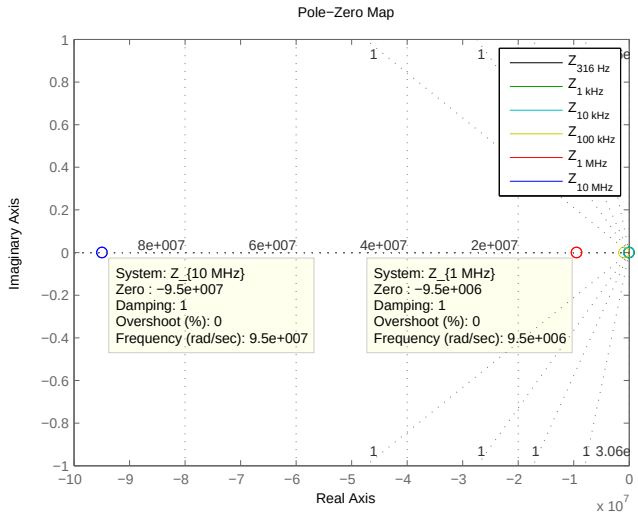

(a) A general view of the pole-zero map showing all the zeros for the system of RL branches, separately

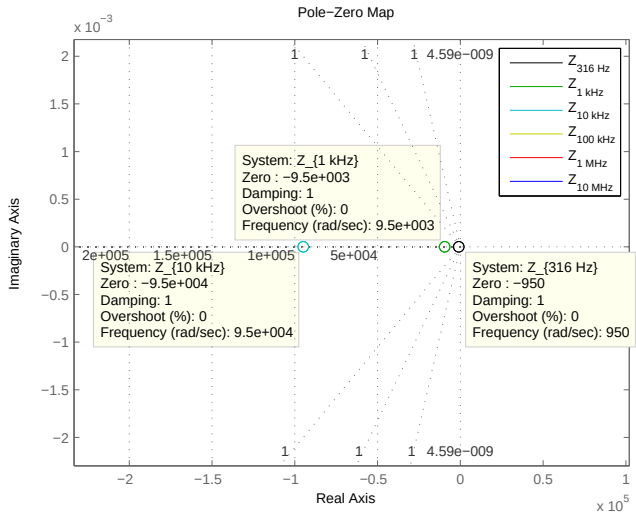

(b) A zoomed-in view of the pole-zero map showing the first three zeros for the system of RL branches

Figure 4.23: Pole-zero plots for the RL-branch ladder representing a single turn's inductance and core losses, and covering a frequency sweep starting from 1 kHz up to 100 MHz - Labels in the legend indicate the start of the decade

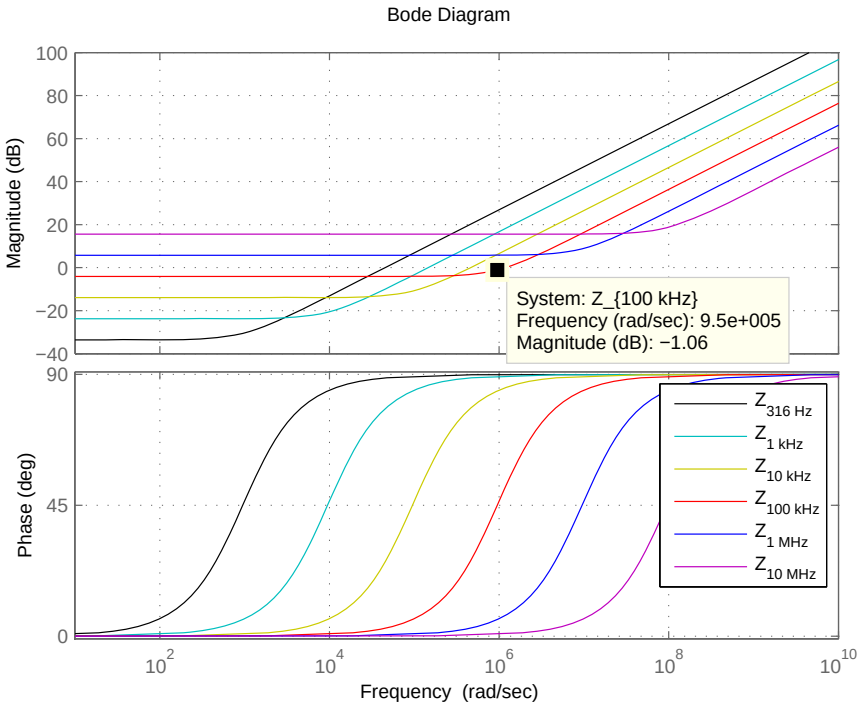

Figure 4.24: Bode plot for the system of RL-branch ladder representing a single turn's inductance and core losses, and covering a frequency sweep starting from 1 kHz up to 100 MHz - Labels in the legend indicate the start of the decade

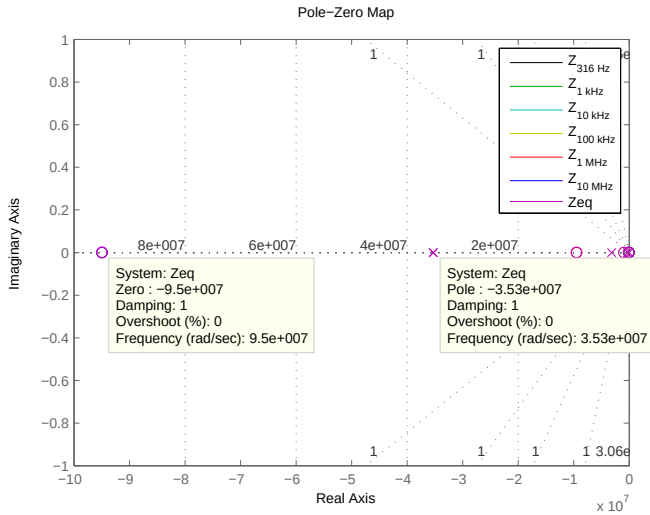

(a) A general view of the pole-zero map showing all the poles and zeros for the system of RL branches and their equivalence

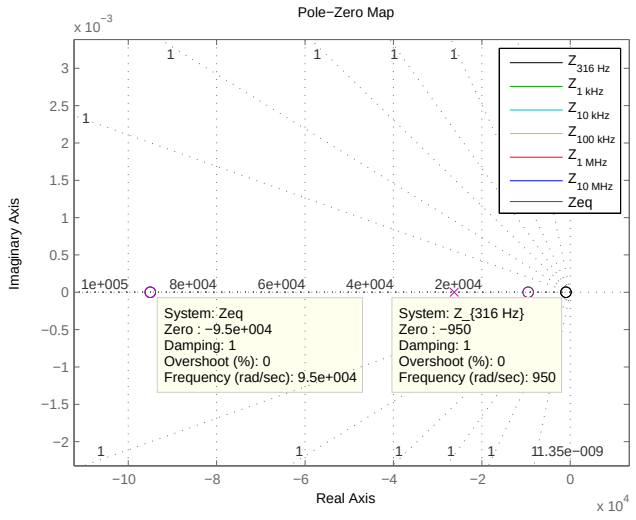

(b) A zoomed-in view of the pole-zero map showing the first three zeros (circles) and the first pole (x) for RL branches and their equivalence

Figure 4.25: Pole-zero plots for the system of RL branches and their equivalence representing a single turn's inductance and core losses, and covering a frequency sweep of 5 decades starting from 1 kHz up to 100 MHz

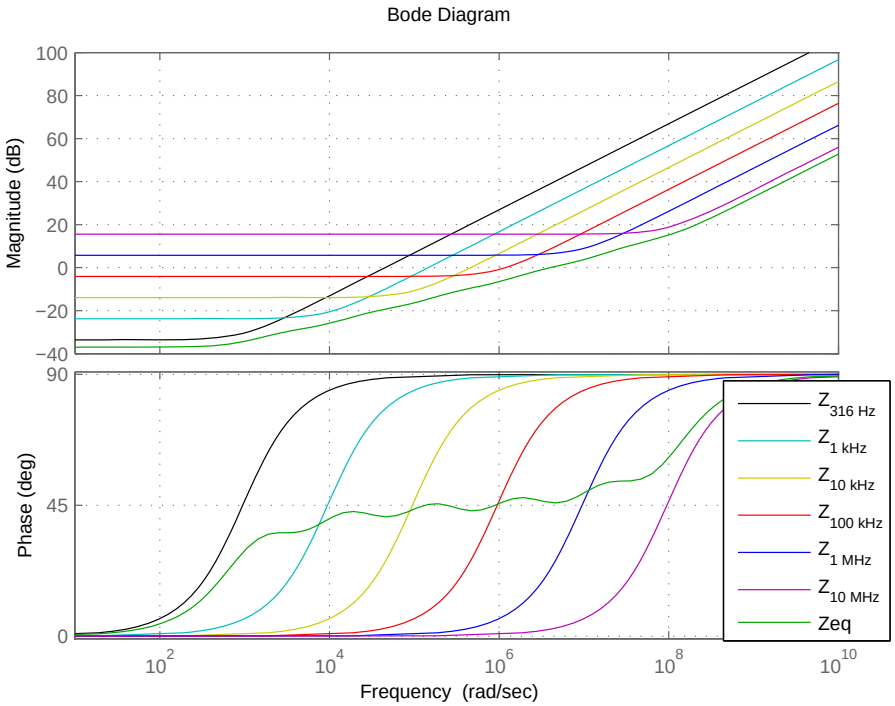

Figure 4.26: Bode plot for the system of RL branches and their equivalence, representing a single turn's inductance and core losses, and covering a frequency sweep of 5 decades starting from 1 kHz up to 100 MHz

where k = 1,2,..n, is the branch number, and n=6 is the number of branches in the system for the frequency sweep of interest

$$\begin{aligned} \mathbf{Y_k} &= \frac{1}{R_k + j \cdot X_k} \\ &= \frac{R_k - j \cdot X_k}{{R_k}^2 + {X_k}^2} \\ For\ X_k &\ll R_k \\ \mathbf{Y_k} &\simeq \frac{1}{R_k} - j \cdot \frac{X_k}{{R_k}^2} \end{aligned} \tag{4.16}$$

As we are interested in the low frequency range just before the *corner frequency* of the first original branch $\mathbf{Z}_{\{\mathbf{316\ Hz \leftrightarrow 1\ kHz}\}}$, then it is fair to assume that $X_k \ll R_k$ in equation 4.16. Adding all the real parts of admittances (conductances) for the branch system to give the conductance of the first original branch with compensation factor, we have:

$$(\mathbf{Y_1 + Y_2 + Y_3 + Y_4 + Y_5 + Y_6})_{\{\mathbf{316\ Hz \leftrightarrow 1\ kHz}\}} \equiv \mathbf{Y}_{\mathbf{1\ \{316\ Hz \leftrightarrow 1\ kHz\}}}$$

For the real parts we have:

$$(\frac{1}{R_1} + \frac{1}{R_2} + \frac{1}{R_3} + \frac{1}{R_4} + \frac{1}{R_5} + \frac{1}{R_6}) \equiv \frac{1}{R_1}$$

$Considering\ R_k = a^{k-1} \cdot R_1,\ where\ (k = 1, 2, ..., 6)$

$$(\frac{1}{R_1} + \frac{1}{a \cdot R_1} + \frac{1}{a^2 \cdot R_1} + \frac{1}{a^3 \cdot R_1} + \frac{1}{a^4 \cdot R_1} + \frac{1}{a^5 \cdot R_1}) \equiv \frac{1}{R_1}$$

Introducing "c_1" as a constant to be multiplied with the resistive part of the first RL branch in the parallel combination, so that the branch system behaves like the original first branch at low frequency. Expressing $R_1 = R_{fcr}$, the core loss equivalent resistance at the first critical frequency, we have:

$$\begin{aligned}\frac{1}{c_1 \cdot R_{fcr}}(1+\frac{1}{a}+\frac{1}{a^2}+\frac{1}{a^3}+\frac{1}{a^4}+\frac{1}{a^5}) &= \frac{1}{R_{fcr}} \\ c_1 &= 1+\frac{1}{a}+\frac{1}{a^2}+\frac{1}{a^3}+\frac{1}{a^4}+\frac{1}{a^5} \\ c_1 &= \sum_{k=0}^{n-1}\frac{1}{a^k} \end{aligned} \tag{4.17}$$

where n = 6 is the number of branches in the system. Given that $a = 3.10 \Rightarrow c_1 = 1.4745$

From equation 4.17, we observe that the compensation factor for the resistive part is dependent on factor "a", the resistance increase factor which reflects core losses increase. The resistance part (r_{core}) in the branch system of figure 4.22 shall be updated to $c_1 \cdot r_{core} = 1.4745 \cdot r_{core}$.

For the imaginary parts we have:

$$(\frac{X_1}{{R_1}^2}+\frac{X_2}{{R_2}^2}+\frac{X_3}{{R_3}^2}+\frac{X_4}{{R_4}^2}+\frac{X_5}{{R_5}^2}+\frac{X_6}{{R_6}^2}) \equiv \frac{X_1}{{R_1}^2}$$

Considering that $R_k = a^{k-1} \cdot R_1$ & $X_k = \frac{X_1}{b^{k-1}}$, where (k=1,2,...,6) and putting in the constant "c_1" we just found from equation 4.17, we have:

$$\frac{1}{{c_1}^2} \cdot (\frac{X_1}{{R_1}^2}+\frac{\frac{X_1}{b}}{(a \cdot R_1)^2}+\frac{\frac{X_1}{b^2}}{(a^2 \cdot R_1)^2}+\frac{\frac{X_1}{b^3}}{(a^3 \cdot R_1)^2}+\frac{\frac{X_1}{b^4}}{(a^4 \cdot R_1)^2}+\frac{\frac{X_1}{b^5}}{(a^5 \cdot R_1)^2}) \equiv \frac{X_1}{{R_1}^2}$$

Introducing "c_2" as a constant to multiply the left-hand side with, so that we get the right-hand side equivalence. Taking note that ($R_1 = R_{fcr}$), we have:

$$(c_2 \cdot \frac{X_1}{{c_1}^2 \cdot R_{fcr}^2}) \cdot (1+\frac{1}{(a^2 \cdot b)}+\frac{1}{(a^2 \cdot b)^2}+\frac{1}{(a^2 \cdot b)^3}+\frac{1}{(a^2 \cdot b)^4}+\frac{1}{(a^2 \cdot b)^5}) = \frac{X_1}{{R_{fcr}}^2}$$

$$c_2 = \frac{{c_1}^2}{1+\frac{1}{(a^2 \cdot b)}+\frac{1}{(a^2 \cdot b)^2}+\frac{1}{(a^2 \cdot b)^3}+\frac{1}{(a^2 \cdot b)^4}+\frac{1}{(a^2 \cdot b)^5}}$$

$$c_2 = \frac{{c_1}^2}{\sum_{k=0}^{n-1} \frac{1}{(a^2 \cdot b)^k}} = \frac{(\sum_{k=0}^{n-1} \frac{1}{a^k})^2}{\sum_{k=0}^{n-1} \frac{1}{(a^2 \cdot b)^k}} \tag{4.18}$$

where n is the number of branches in the system, "a" is the increase factor of resistance & "b" is the decrease factor of inductance in each successive branch, and "c_1" is the compensation factor for the resistive part in the first branch. Given that $a = 3.10,\ b = 3.23$ & $c_1 = 1.4745 \ \Rightarrow \ c_2 = 2.1041$

From the relation 4.18 we observe that the compensation factor for the inductive part is not only dependent on the inductance decrease factor "b", but also the resistance increase factor "a".

Generating bode plot for the branch system with compensated factors in the first branch, along with the original fisrt branch we have:

So from figure 4.27 we can see an accomplishment of a satisfactory high-frequency behaviour for the system of parallel branches expressing the inductance decrease and core losses, meanwhile we see a very good agreement between the equivalent branch system and the original branch representing the first critical frequency, f_{cr1}, (i.e. the first branch before introducing the compensation factors) in the low-frequency range.

We also notice that the high frequency behaviour is even lower than the response of the outer most branch (see figure 4.28). This makes sense as we parallel-connect all the branches in the system and the resulting equivalent impedance/response will be lower than the response for any branch.

We observe that the high frequency behaviour of the branch system over 10^7 [rad/sec] has been reduced from about 60 dB to 12 dB compared to the case of the originial branch expressing (f_{cr1}). On the other hand the low-frequency behaviour has a mismatch of 1.3 dB compared to the same branch. From the fourth decade up to the eighth (10^4 up to 10^8), the mismatch has been between 4–6 dB with less than 4 dB difference in the high frequency range above the 8th decade [rad/sec]. This is not the complete model as we will continue developing the model to include the phenomena at dc and very low frequency.

The next and final step in developing the complete model for the single turn along a frequency sweep, is to add the resistive copper losses to the model along with the ac part that was developed earlier. At very low frequency close to dc the resistive copper losses are dominant and the inductance effect is negligible.

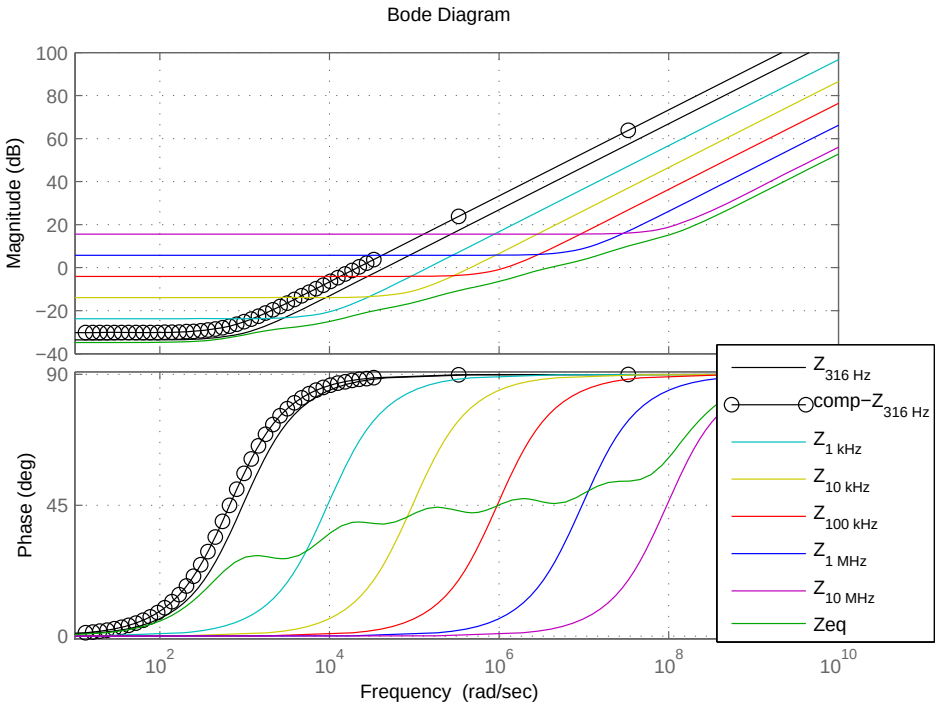

Figure 4.27: Bode plot for the system of RL branches and their equivalence after inserting compensation factors in the first branch

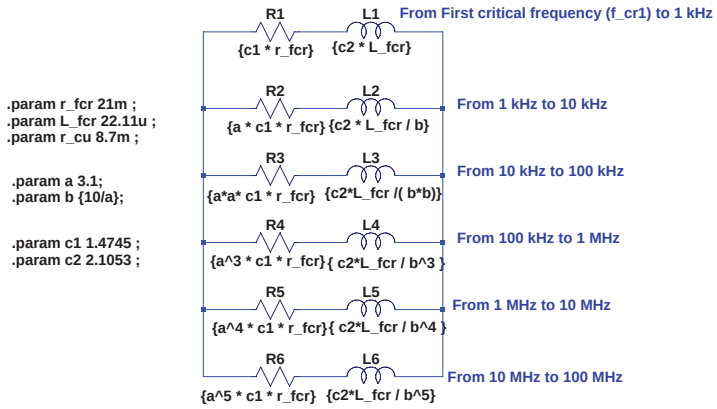

Figure 4.28: An improved ladder model for a single turn's ac inductance and core losses covering a frequency sweep including and starting from 1 kHz up to 100 MHz

The inductance at low frequency will be taken care of by the first branch in the proposed ladder model. A mismatch between the proposed model and the FEMM/measurement data could rise for the frequency range where the inductance is not associated with significant core losses, which is usually limited along the frequency band. In that case a simple RL model with no compensation factor can fill the gap, in which the resistance expresses the dc copper resistive losses (R_{Cu}), and the inductance is the FEMM magnetostatic inductance value.

The challenge is to mainatin the dc and low frequency behaviour of the whole combination, meanwhile not affecting the accomplished high-frequency behaviour. This is the reason why we will introduce a third and final compensation factor "c_3" for the resistive copper losses (R_{Cu}) in the model.

Following the same approach in the system equations 4.17 & 4.18, and this time for the real part of the whole combination, we have:

$$R_{Cu} + R_{eq} \equiv R_{Cu}$$

$$c_3 \cdot R_{Cu} + R_{eq} = R_{Cu}$$

$$c_3 = 1 - \frac{R_{eq}}{R_{Cu}}$$

but

$$R_{eq} = \frac{1}{\frac{1}{c_1 \cdot R_{fcr}} + \frac{1}{R_2} + \frac{1}{R_3} + \frac{1}{R_4} + \frac{1}{R_5} + \frac{1}{R_6}}$$

Considering that $R_k = a^{k-1} \cdot c_1 \cdot R_{fcr}$, where (k = 1,2,...,n & n = 6)

$$R_{eq} = \frac{1}{\frac{1}{c_1 \cdot R_{fcr}} + \frac{1}{a \cdot c_1 \cdot R_{fcr}} + \frac{1}{a^2 \cdot c_1 \cdot R_{fcr}} + \frac{1}{a^3 \cdot c_1 \cdot R_{fcr}} + \frac{1}{a^4 \cdot c_1 \cdot R_{fcr}} + \frac{1}{a^5 \cdot c_1 \cdot R_{fcr}}}$$

$$= \frac{1}{\frac{1}{c_1 \cdot R_{fcr}} \cdot c_1} = R_{fcr}$$

$\Longrightarrow$

$$c_3 = 1 - \frac{R_{fcr}}{R_{Cu}} \tag{4.19}$$

From equation 4.19, we observe that the compensation factor for the resistive copper losses "c_3" is dependent on:

- The resistive copper losses value itself (R_{cu}).
- The resistance of the first branch of the ac inductance model (R_{fcr}), which stands for the maximum core loss corresponding to minimum change in ac inductance.
- Compensation factor "c_1" introduced to the first branch resistance.

So the compensation factors "a" and "b" along with "c_1", "c_2", and "c_3", which are needed to cover the whole frequency sweep for a single turn model, are summarized in the following table:

The complete model for a single turn of copper winding on an iron core, after including the core loss model and introducing the three compensation factors

Constant	Formula	Value
a	fromm FEMM analysis	3.10
b	$b = \frac{10}{a}$	3.23
c_1	$\sum_{k=0}^{n-1} \frac{1}{a^k}$	1.4745
c_2	$\frac{c_1^2}{\sum_{k=0}^{n-1} \frac{1}{(a^2 \cdot b)^k}}$	2.1053
c_3	$1 - \frac{R_{fcr}}{R_{Cu}}$	-1.5414

Table 4.7: Summary of the compensation factors for a single turn's complete model along a frequency sweep from dc up to 100 MHz

to cover the whole frequency sweep, will look like:

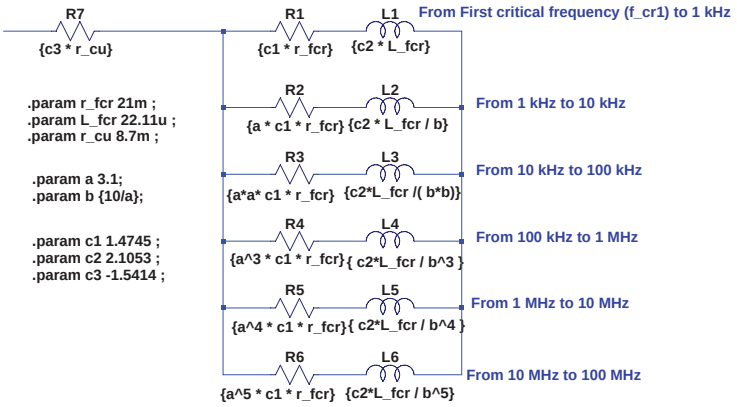

Figure 4.29: A single turn of copper winding on an iron core model covering a frequency sweep from dc up to 100 MHz

As can be seen from figure 4.29, we need 3 fundamental quantities to be fed from the FEMM analysis to the circuit model, which are; the resistive copper losses in the copper conductor (R_{cu}), the maximum core losses corresponding to minimum change in inductance value (R_{fcr}), and the inductance value at that frequency point (L_{fcr}). In addition to the constant "a" that indicates the increase of core losses for each successive decade of frequency, 3 more secondary

constants will be needed. Constants "c_1", "c_2" and "c_3" are derived from the fundamental quantities as per equations 4.17, 4.18 & 4.19, respectively.

Plotting Bode-plot for the complete turn's model reposnse (red curve) along with the response of the dc ($R_{Cu}L_{dc}$) branch (yellow stars), the first critical frequency ($R_{fcr}L_{fcr}$) branch (black) , and the ac model for inductance and core losses (green) will give:

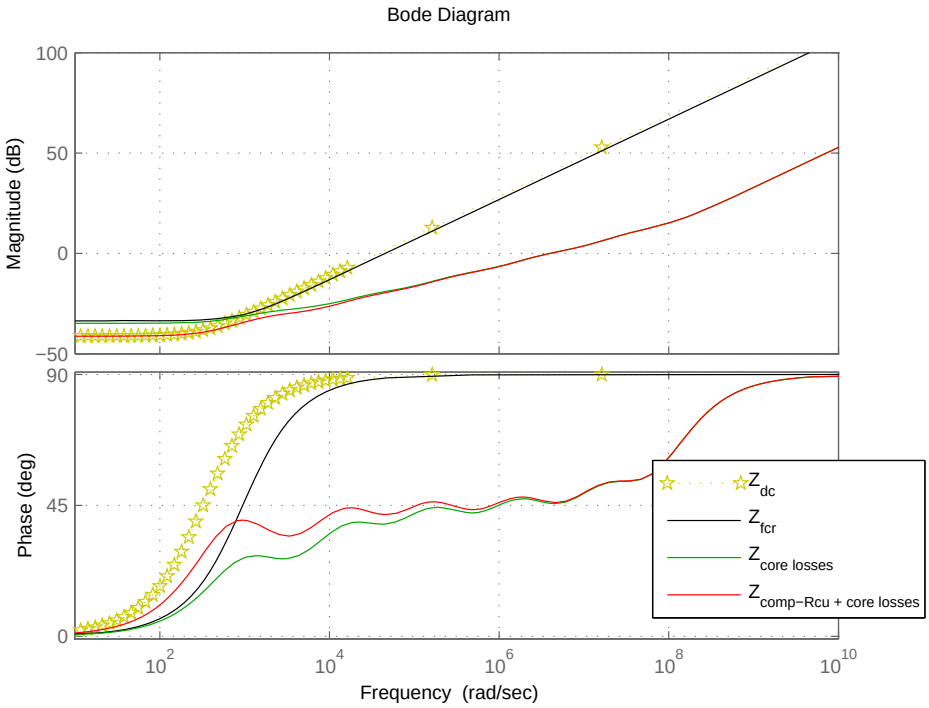

Figure 4.30: Bode plot for the system of RL branches and their equivalence after inserting compensation factors in the first branch

Notice the very good agreement both in low and high frequencies. Observe that the high frequency behaviour reflecting core losses is now not directly proportional to the frequency, rather it counts for high frequency losses.

Chapter 5

Model Validation

Different measurements have been taken for the winding-on-core prototype shown in figure 2.8 by the hp impedance analyzer 4194A. Measurements of impedance frequency response along a frequency band from dc up to 40 MHz for different acces points of the prototype have been performed. The following measurements have been recorded:

(1.) Excitation of the measurement device was set between the winding input at the 1^{st} access point, and the winding output at the 4^{th} access point measuring the three conductor layers response.(see table 2.1)

(2.) Excitation was set between the winding input at the 1^{st} access point, and the second layer input at the 2^{nd} access point measuring the first layer response.

(3.) Excitation was set between the winding second layer input at the 2^{nd} access point, and third layer input at the 3^{rd} access point measuring the second layer response.

(4.) Excitation was set between the winding third layer input at the 3^{rd} access point, and the winding output at the 4^{th} access point measuring the third layer response.

(5.) Excitation was set between the winding input at the 1^{st} access point, and the winding third layer input at the 3^{rd} access point measuring the first two layers response.

(6.) Excitation was set between the winding second layer input at the 2^{nd} access point, and the winding output at the 4^{th} access point measuring the last two layers response.

(7.) Excitation was set between the winding input at the 1^{st} access point, and the magnetic iron core at the 5^{th} access point measuring the winding input-to-ground response.

(8.) Excitation was set between the winding second layer input at the 2^{nd} access point, and the magnetic iron core at the 5^{th} access point measuring the winding first layer-to-ground response.

(9.) Excitation was set between the winding third layer input at the 3^{rd} access point, and the magnetic iron core at the 5^{th} access point measuring the winding first and second layer-to-ground response.

(10.) Excitation was set between the winding third layer output (winding output) at the 4^{th} access point, and the magnetic iron core at the 5^{th} access point measuring the winding first,second and third layer-to-ground response.

(11.) Short-circuiting the winding input at the 1^{st} access point, and output at the 4^{th} access point and then setting the excitation between the common short circuit point and the magnetic iron core at the 5^{th} access point in order to cancel the inter-winding capacitances and highlight the lumped sum of all capacitances to ground contributed by each turn in the winding.

(12.) Short-circuiting the winding input at the 1^{st} access point, second layer input at the 2^{nd} access point, third layer input at the 3^{rd} access point, and winding output at the 4^{th} access point and then setting the excitation between the common short circuit point and the magnetic iron core at the 5^{th} access point in order to further cancel any inter-winding capacitances and parasitic capacitances due to acces points conductors. This measurement also highlights the lumped sum of all capacitances to ground contributed by each turn in the winding.

Figures 5.1 and 5.2 show the response for different layers in the wiring arrangement where excitation was set between different access points of the winding. The behaviour is inductive in all the measurements up until the first resonance frequency at 5-6 MHz. An interesting observation when scaling a single layer measurement to fit a double layer's as in figure 5.2 or a tripple layer's as in figure 5.1; is that there's very good agreement between the scaled measurement and the actual one up to the first resonance frequency. The capacitive

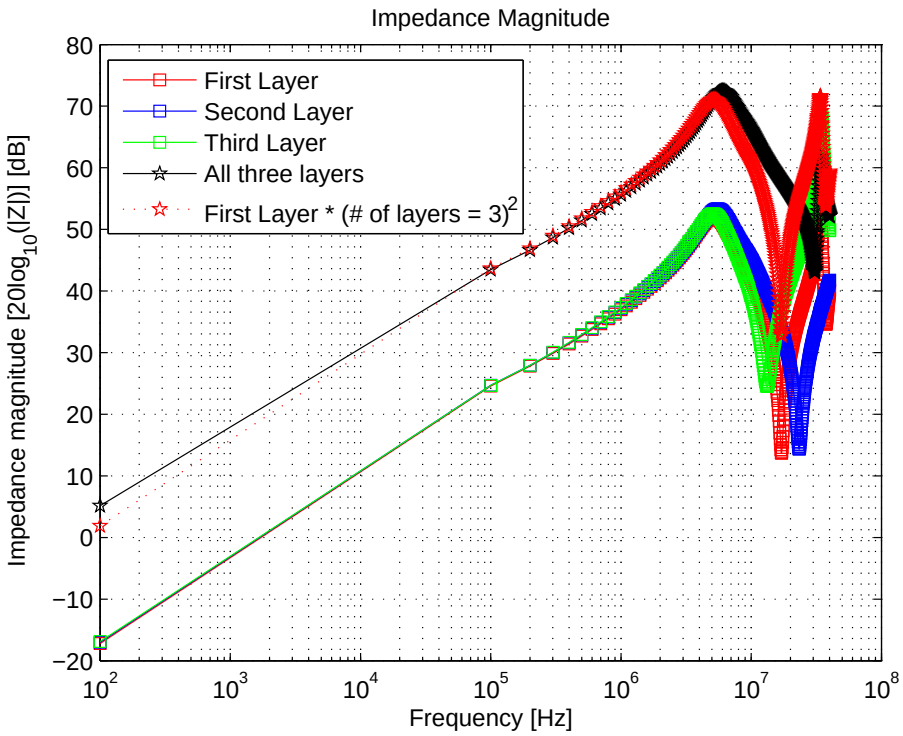

Figure 5.1: Measurements of impedance magnitude for the winding-on-core prototype along a frequency band from 0 Hz up to 40 MHz - single and tripple layers

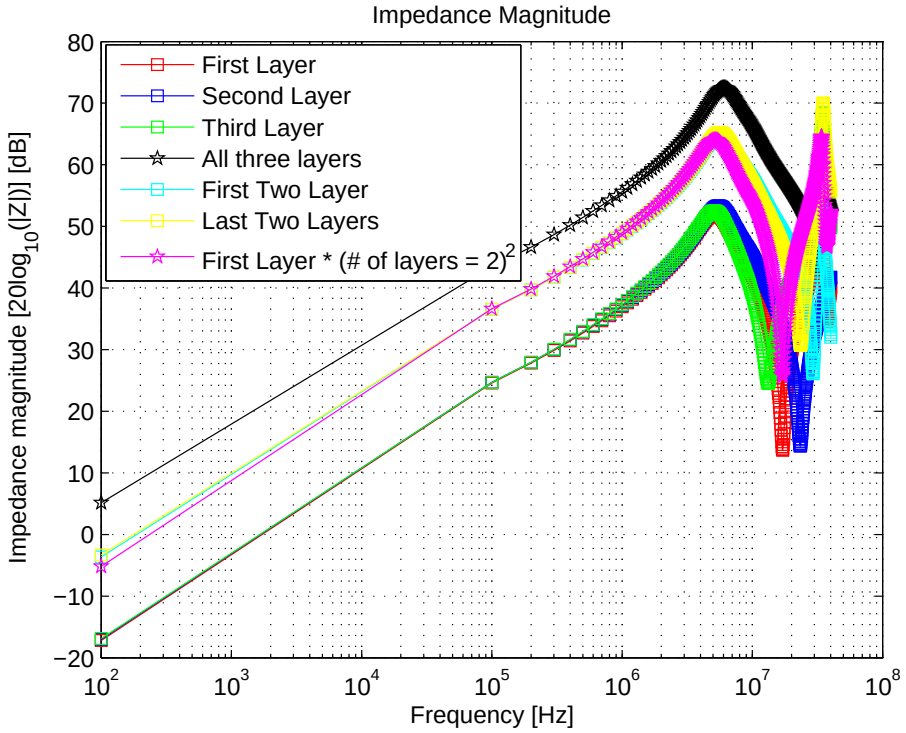

Figure 5.2: Measurements of impedance magnitude for the winding-on-core prototype along a frequency band from 0 Hz up to 40 MHz - single layer, two layers and three layers

behaviour occuring after the first resonance has significantly increased (3 dB difference on average). This can be seen by the lower negative slope line on the logarithmic impedance-frequency scale which indicates higher capacitance value as we are plotting ($X_c = \frac{1}{\omega C}$) vs. frequency.

This is partly due to the fact that capacitances associated with a single layer are not scaled as the inductance by multiplying with the number of layers squared. The other reason is that considering the higher value of turn-to-turn capacitance (C_{tt}) compared to the turn to ground's (C_{tg}) as it was found in the capacitive coupling analysis earlier; having fewer turns will result in higher lumped equivalent capacitance especially when viewing the turn-to-turn capacitances to be series-connected between the ends of the layer. The equivalent capacitance for series-connected capacitances is given by:

$$C_{eq} = \frac{1}{\sum_{k=0}^{n} \frac{1}{c_k}} \tag{5.1}$$

where n is the number of series-connected capacitances.

In the experimental verification of the model two model versions were used, one optimized towards capacitively coupled model, and the other optimized towards the inductively coupled model.

5.1 Capacitively Coupled Optimized Validation

In the case of the model optimized towards capacitive coupling, 3 versions of the model were used where the capacitance network on the turn level, generated in chapter 3 has been used in all of them. The three versions of the model are:

(1.) The capacitance network is used to represent turn-to-turn capacitances (C_{tt}) and turn-to-ground capacitances (C_{tg}). The turn resistance and inductance are chosen to be the dc quantities of the analysis in section 4.

(2.) In addition to the capacitance network in the model, the turn inductance is represented by the the first 2 decades of the ac inductance and core loss model developed in section 4.4.

(3.) In addition to the capacitance network in the model, the turn inductance is represented by the the first 3 decades of the ac inductance and core loss

model developed in section 4.4.

Measurement for a single layer containing 8 turns is taken as the measurement reference in the validation process, since it represents the minimum section measured within the wiring arrangement. As we have noticed earlier in figure 5.2, single, double and tripple layers have identical behaviour (given the proper scaling factor) up until the first resonance frequency, and similar behaviour after the first resonance.

The simulation model has been subjected to the same exitation which was set in the measurement, i.e. for the first layer to be between the winding input at the 1^{st} access point, and the second layer input at the 2^{nd} access point. The model measuremenet layout and measurement results are shown in the figures below:

From figure 5.3 we observe that there is a significant gain differenece between the two curves in the range of (20 - 30 dB) during the inductive behaviour of the simulation model, as no core loss effect is represented; however the resonance frequency occurence of the simulation model is at 4.3 MHz which is very close to the measurement's at 5.2 MHz.

From figures 5.4 and 5.5, we see a tendency to reduce the gain difference between the two curves as we include more decades of the core loss model. This is done on the expense of shifting the difference between the first resonance ocurrences of the two curves further.

In figure 5.4 we see a difference in the range of (12 - 15 dB) between the two curves during the inductive behaviour, indicating a relative reduction in the difference since a core loss representation covering two decades of frequency on the turn level has been inserted; however the first resonance frequency of the simulation model has become 9 MHz, increasing the difference in first resonance frequency occurrence to be almost 4 MHz.

On the other hand we notice a very good agreement in figure 5.5 between the simulation model output and measurements during the inductive behaviour, when a core loss model of 3 branches representing three frequency decades has been inserted; however this comes with the expense of even further distance between the first resonance frequency occurrences for the two curves as it becomes more than 12 MHz.

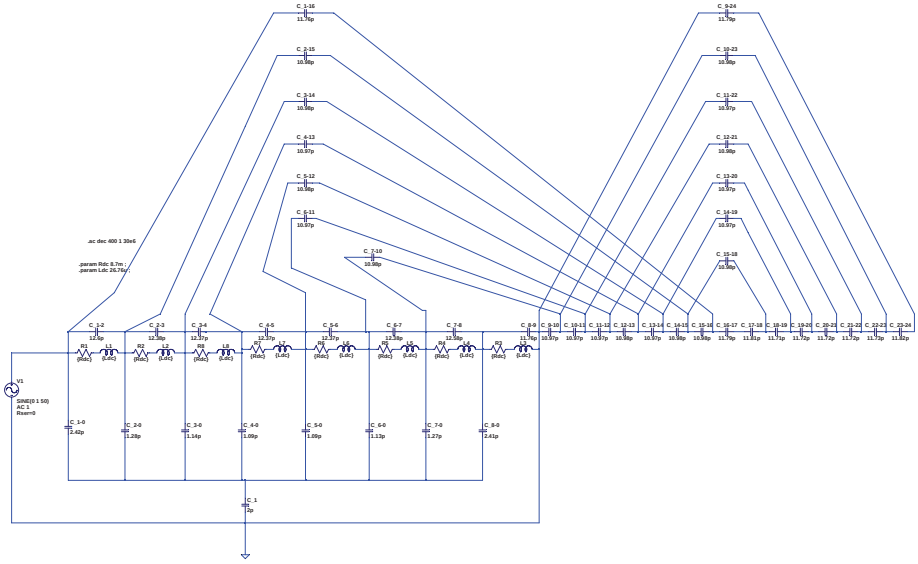

(a) Layout of the simulation model optimized towards capacitive coupling where turn resistance and inductance are the dc quantities

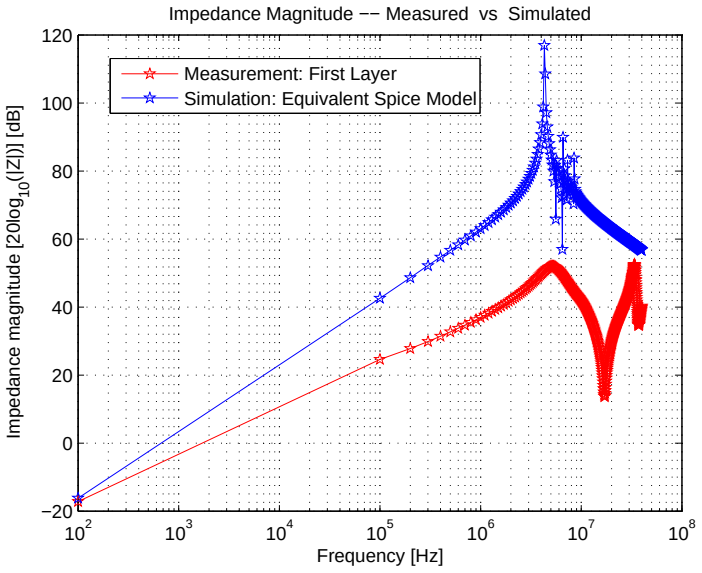

(b) Agreement between measurement data and simulation model output - Capacitively coupled optimized model version-1

Figure 5.3: Layout of simulation model optimized towards capacitive coupling version-1 and its agreement with measurement data

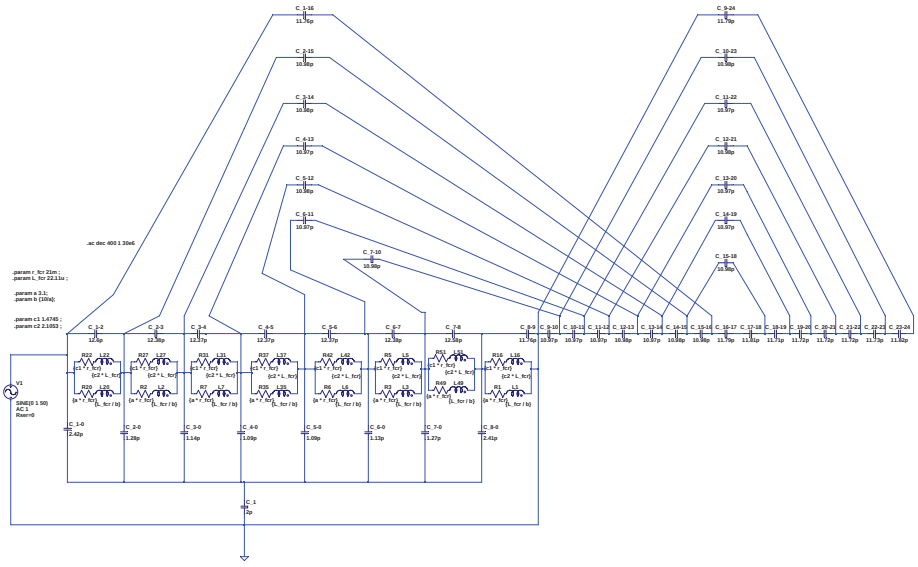

(a) Layout of the simulation model optimized towards capacitive coupling where a core loss model covering 2 decades on the turn level has been inserted

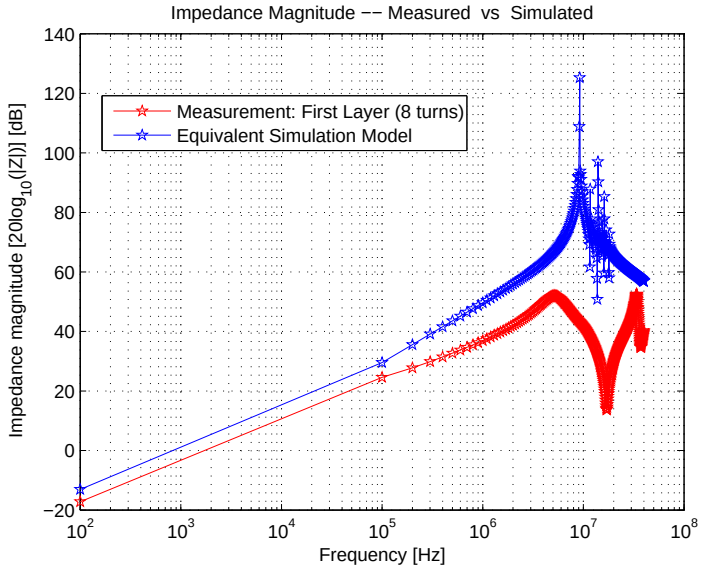

(b) Agreement between measurement data and simulation model output - Capacitively coupled optimized model version-2

Figure 5.4: Layout of simulation model optimized towards capacitive coupling version-2 and its agreement with measurement data

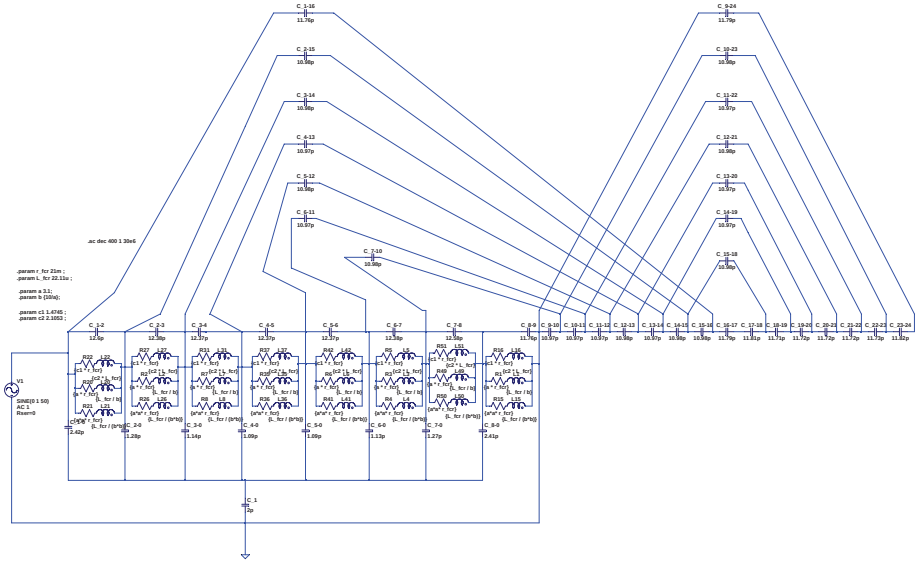

(a) Layout of the simulation model optimized towards capacitive coupling where a core loss model covering 3 decades of frequency has been inserted

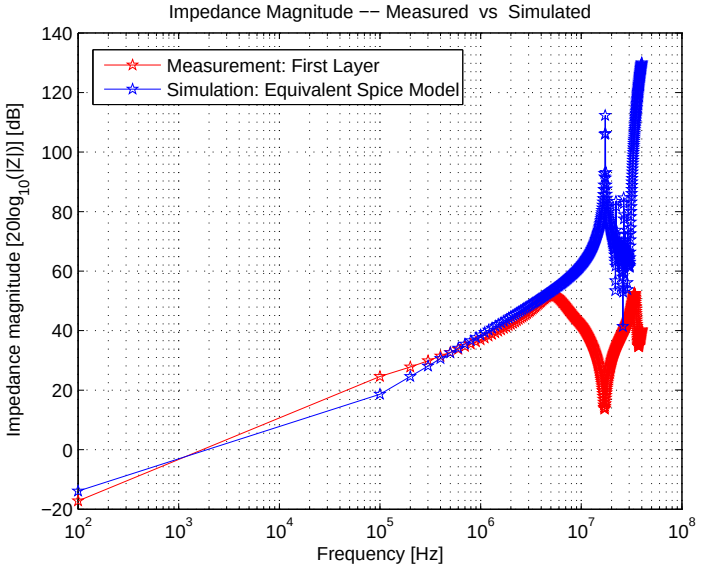

(b) Agreement between measurement data and simulation model output - Capacitively coupled optimized model version-3

Figure 5.5: Layout of simulation model optimized towards capacitive coupling version-3 and its agreement with measurement data

5.2 Inductively Coupled Optimized Validation

For the single turn simulation model with core loss representation which is optimized towards inductive coupling, the model has two capacitances to ground (C_{tg}) connected on each end of the model and a one turn-to-turn capacitance (C_{tt}) connected across the model, since the turn is considered to be in the first layer. The model layout and the comparison between simulation outcome and measurement is shown below.

In figure 5.6b the measurement data representing 8 turns is compared against the simulation model output of one turn. The model output is scaled as per the number of turns in the first layer, and also as per the number of turns giving the best fit to the measurements. The following observations can be noticed:

(1.) Inductively optimized turn model has no indication of any resonance frequency behaviour despite the representation of capacitances to ground (C_{tg}) and turn-to-turn capacitance (C_{tt}) in the model.

(2.) The single turn model doesnt scale to the 8-turn-layer measurement, in the inductive part of the measurement data. The best fit in our case indicates 5 turns instead of 8. This strongly suggests that capacitive coupling has prominent effect resulting in effectively bypassing 3 turns out of 8 in order to get the best fit within the inductive region.

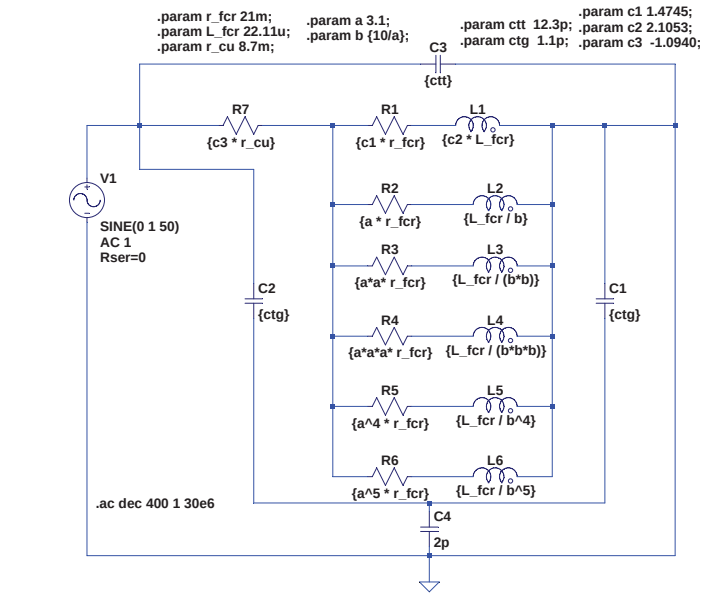

(a) Layout of the simulation model of a single turn with core loss model and optimized towards inductive coupling

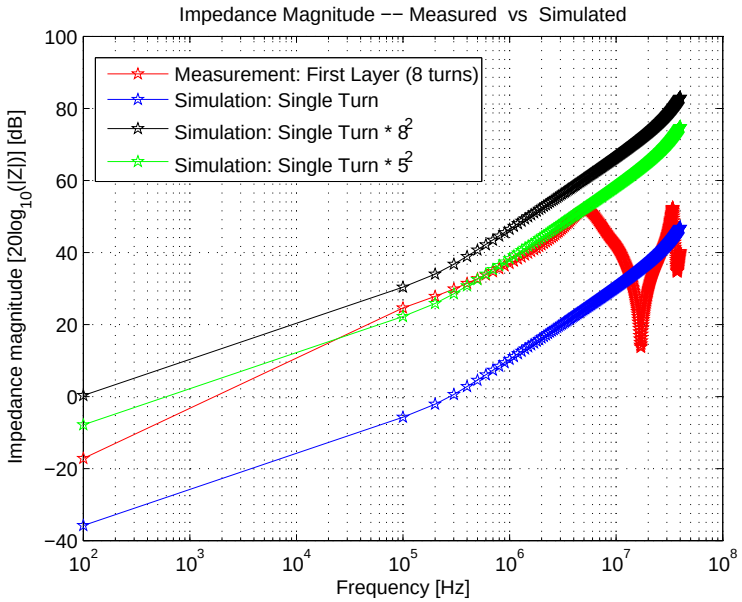

(b) Agreement between measurement data and simulation model output

Figure 5.6: Layout of simulation model optimized towards inductive coupling and its agreement with measurement data

Chapter 6

Conclusions and Future Work

Given the possibility of representing high frequency phenomena with SPICE circuit models and the methodology followed throughout this thesis in proposing the circuit model elements, the following conclusions are observed:

- The number of branches representing the frequency decades in the core loss model on the turn level seems to be oversized when including it with the capacitance network in the capacitively coupled model (subsection 5.1) for model version-2 (sub-figure 5.4a) and version-3 (sub-figure 5.5a). It appears that due to capacitive coupling among turns, 2 or 3 branches of the core loss model is adequate in representing the frequency dependence of the core loss and consequently the inductance along the frequency sweep of interest.

- Capacitive coupling among the winding layers are more influential in having a very good agreement both for the resonance behaviour of the winding and the gain difference within the inductive region.

- When scaling one turn model to fit a single layer measurement of a certain number of turns, the study suggests only portion of the number of turns may be considered. In our case $\frac{5}{8} \approx 63\%$ of the actual turns. This suggests that capacitive coupling between the turns effectively bypass some turns and so affecting the gain within the inductive region of the model.

There is no clear cut single model when it comes to representing the high frequency behaviour of a winding under SPICE. We could optimize the model representation towards capacitive or inductive coupling.

When optimized towards capacitive coupling, only dc quantities of the turn resistance and inductance seems to be adequate in telling the resonance frequency behaviour of the model. For having good agreement within the inductive region of the measurement, three branches of the core loss model on the turn level is enough when inserted in the capacitance network of the capacitively coupled model.

When optimized towards inductive coupling, we can only have agreement within the inductive region of the measurement data, as there is no indication about the frequency resonance behaviour of the simulation model output. In order to get good agreement in that region, only portion of the turns may be considered as capacitive coupling between the turns is effectively bypassing some of them.

Further investigation about the best methodology of combining capacitive and inductive coupling outcomes of the model, in an automated way and introducing desired thresholds and accuracy levels, may be needed. Capacitive or inductive coupling by itself can not be calculated from first principles as we have noticed throughout this thesis. We have seen the need of using simulation software package like FEMM to perform these analyses. So the combination process would rather account for similar accuracy and complexity levels in order to produce narrow and more specific conclusions.

Future work may also include the extension of the winding-on-core study to the stator machine case, since more details about the ferromagnetic material of the laminations could be available from the manufacturer. Magnetic characteristics of the lamination proved to be crucial in the inductive coupling behaviour of the winding and the machine generally. Analysis on the turn level of a winding inside a machine stator slots, and the comparison to measurements on numbered and pre-determined access points, can give more insights about the high-frequency behaviour of a winding inside machine slots.

Glossary

Bobbin A cylinder or spindle on which the wire, thread or film is wound. It can be with or without flanges and can be typically found in wire rolls, sewing machines, cameras, and within electronic equipment. 39

End Turn The winding portion which lies outside the active length of the machine stator. It does not contribute to torque production while it contributes to the losses. It can extend up to $\frac{1}{3}$ of the active axial length on each side of the stator especially for small machines. iii, 11, 12, 14

Integral Slot The number of slots per pole per phase is an integer. iii, 10–12

Pole Pitch The mechanical angular distance between consecutive (electro)magnetic poles expressed in mechanical units; For an electric machine of N-poles, the pole pitch τ_p in mechanical degrees will be $\frac{360^\circ}{N}$. 12

Single Layer Winding a winding configuration where one side of the winding totally occupies one slot. iii, 10, 11, 13

Acronyms

ANSI American National Standards Institute. 101

CISPR International Special Committee on Radio Interference. 101

CM Common-Mode. 4, 6

dB Decibel. viii, 27, 105–108

DM Differential-Mode. 2

DSO Digital Storage Oscilloscope. 9

EDM Electric Discharge Machining. 6

ELP Earth Leakage Protection. 5

EMC ElectroMagnetic Compatibility. 1, 2, 6, 8, 10, 12, 100, 103

EMI ElectroMagnetic Interference. i, 2, 6, 8, 101

ESS Energy Storage System. 1, 2, 6, 7, 9

F Farad. 3, 4

FEM Finite Element Method. 9, 19

hp Hewlett Packard. i, 7, 9, 17, 83

IEC International Electrotechnical Commission. 101

IGBT Insulated Gate Bipolar Transistor. 4

n nano. 4

p pico. 3

PWM Pulse-Width Modulation. 2, 8–10, 100–102

q Slots per Pole per Phase. iii, 10–13

struct structure array. 9

VCC Volvo Car Corporation. 8, 100

References

[1] J. Adabi, F. Zare, G. Ledwich, and A. Ghosh. Leakage current and common mode voltage issues in modern ac drive systems. In *Power Engineering Conference, 2007. AUPEC 2007. Australasian Universities*, pages 1 –6, December 2007. 2, 5

[2] M. Alaküla, April 2009. A professor in industrial electrical engineering at Lund Institute of Technology (LTH) - Lund University, and also a Senior Scientific Advisor at Volvo AB with emphasis on hybrid vehicles. 2

[3] M. Alaküla and P. Karlsson. *Power Electronics Devices, Converters, Control and Applications*. Department of Industrial Electrical Engineering and Automation, Lund University, 2003. 2

[4] S. Alexandersson, M. Alaküla, and H. Bängtsson. Prediction of parasitic components in an automotive environment. In *Electromagnetic Compatibility, 2008. EMC 2008. IEEE International Symposium on*, pages 1 –7, August 2008. 2

[5] S. Alexandersson and H. Bängtsson. Analytic prediction of electromagnetic behaviour. In *International Symposium on Power Electronics, Electrical Drives, Automation and Motion, 2008. SPEEDAM 2008*, pages 338 –343, June 2008. 2

[6] H. Berg, May 2009. Electronic Engineer at VCC with a focus on EMC in cars. 2, 8

[7] P. A. Chatterton and M. A. Houlden. *EMC: Electromagnetic Theory to Practical Design*. Wiley, Chichester, 1992. 43

[8] S. Chen, T.A. Lipo, and D. Fitzgerald. Source of induction motor bearing currents caused by PWM inverters. *Energy Conversion, IEEE Transactions on*, 11(1):25 –32, March 1996. 5

[9] Sh. Chen and T.A. Lipo. Bearing currents and shaft voltages of an induction motor under hard and soft switching inverter excitation. In *Industry Applications Conference, 1997. Thirty-Second IAS Annual Meeting, IAS '97., Conference Record of the 1997 IEEE*, volume 1, pages 167 –173 vol.1, October 1997. 5

[10] D. K. Cheng. *Field and Wave Electromagnetics*. Addison-Wesley series in electrical engineering. Addison-Wesley, 1989. 15, 25, 41, 43, 48

[11] Cogent Typical Data. Non oriented electrical steel, June 2012. Surahammars Bruks AB, PO Box 201, SE-735 23 Surahammar, Sweden. 52

[12] K. R. Demarest. *Engineering Electromagnetics*. Prentice-Hall International, London, 1998. 41, 43, 75

[13] J.M. Erdman, R.J. Kerkman, D.W. Schlegel, and G.L. Skibinski. Effect of PWM inverters on ac motor bearing currents and shaft voltages. *Industry Applications, IEEE Transactions on*, 32(2):250 –259, March/April 1996. 5

[14] O. Henze, Z. Cay, O. Magdun, H. De Gersem, T. Weiland, and A. Binder. A stator coil model for studying high-frequency effects in induction motors. In *International Symposium on Power Electronics, Electrical Drives, Automation and Motion, 2008. SPEEDAM 2008*, pages 609 –613, June 2008. 17

[15] Specifications in ANSI C63.2 and/or CISPR 16-1-1:2006. American National Standards Institute (ANSI), International Special Committee on Radio Interference (CISPR) - International Electrotechnical Commission (IEC). 5, 9, 43

[16] DASOL Product Information. Round enamelled winding wire of copper, solderable, class 155, April 2011. AB DAHRNTRÅD, Jonslund, SE-465 80 Nossebro, Sweden. 23

[17] J. Luszcz. Motor cable effect on the converter fed ac motor common-mode current. In *Compatibility and Power Electronics (CPE), 2011 7th International Conference-Workshop*, pages 445 –450, June 2011. 43

[18] J. Luszcz and K. Iwan. Modelling conducted EMI in inverter-fed ac motor. In *Compatibility in Power Electronics, 2005. IEEE*, pages 209 – 212, January 2005. 2

[19] J. Luszcz and K. Iwan. Conducted EMI propagation in inverter-fed ac motor. In *Electrical Power Quality and Utilisation Magazine, Vol II, No. 1*, pages 47 – 51, 2006. 2

[20] O. Magdun, A. Binder, C. Purcarea, and A. Rocks. High-frequency induction machine models for calculation and prediction of common-mode stator ground currents in electric drive systems. In *Power Electronics and Applications, 2009. EPE '09. 13th European Conference on*, pages 1 –8, September 2009. 18

[21] O. Magdun, A. Binder, A. Rocks, and O. Henze. Prediction of common-mode ground current in motors of inverter-based drive systems. In *Electrical Machines and Power Electronics, 2007. ACEMP '07. International Aegean Conference on*, pages 806 –811, September 2007. 18

[22] P. Maki-Ontto, H. Kinnunen, and J. Luomi. Three-phase model for the circuit simulation of common-mode phenomena and shaft voltages in ac motor drive systems. In *Electric Machines and Drives, 2005 IEEE International Conference on*, pages 437 –443, May 2005. 5

[23] D. Meeker. *Finite Element Method Magnetics - User's Manual, Version 4.2*. dmeeker@ieee.org, October 2010. 24, 45, 53, 54

[24] V. Mihaila, S. Duchesne, and D. Roger. A simulation method to predict the turn-to-turn voltage spikes in a PWM fed motor winding. *Dielectrics and Electrical Insulation, IEEE Transactions on*, 18(5):1609 –1615, October 2011. 18

[25] N. Mohan, T. M. Undeland, and W. P. Robbins. *Power Electronics: Converters, Applications and Design*. Wiley, New York, 1995. 2

[26] B. Muralidhara, A. Ramachandran, R. Srinivasan, and M.C. Reddy. Experimental measurement of shaft voltage and bearing current in an inverter fed three phase induction motor drive. In *Electronics Computer Technology (ICECT), 2011 3rd International Conference on*, volume 2, pages 37 –41, April 2011. 2

[27] R. Naik, T.A. Nondahl, M.J. Melfi, R. Schiferl, and Jian-She Wang. Circuit model for shaft voltage prediction in induction motors fed by PWM-based

ac drives. *Industry Applications, IEEE Transactions on*, 39(5):1294 – 1299, September-October 2003. 5

[28] S. Ogasawara and H. Akagi. Modeling and damping of high-frequency leakage currents in PWM inverter-fed ac motor drive systems. *Industry Applications, IEEE Transactions on*, 32(5):1105 –1114, September-October 1996. 2, 3

[29] T. Rybak and M. Steffka. *Automotive Electromagnetic Compatibility (EMC)*. Kluwer Academic Publishers, 2004. 43

[30] B.K. Sen and R.L. Wheeler. Skin effects models for transmission line structures using generic spice circuit simulators. In *Electrical Performance of Electronic Packaging, 1998. IEEE 7th Topical Meeting on*, pages 128 –131, October 1998. 75

[31] J. Welinder, January 2011. A Deputy Manager at SP Technical Research Institute of Sweden, with background and 24+ years of experience in EMC laboratory measurements and testing. 20

[32] B.W. Williams. *Principles and Elements of Power Electronics: Devices, Drivers, Applications, and Passive Components*. Barry W Williams, 2006. 2

[33] T. Williams. *EMC for Product Designers*. Newnes, Oxford, 2007. 5

[34] R.A. Witte. *Spectrum and Network Measurements*. Prentice Hall, 1993. 31, 117

[35] M.T. Wright, S.J. Yang, and K. McLeay. General theory of fast-fronted interturn voltage distribution in electrical machine windings. *Electric Power Applications, IEE Proceedings B*, 130(4):245 –256, July 1983. 18

Appendices

Appendix A

Decibel

dB is a logarithmic unit expressing a ratio. The ratio can describe two power quantities, currents or voltages. The difference in dBs between two power quantities is defined as ten times the logarithm to base 10 for the ratio of the two power quantities.

In mathemetical notation:

$$10 * \log(\frac{P_2}{P_1}) \tag{A.1}$$

Note the factor of 10 in the definition which explains the term "deci" in "decibel", so a "decibel" is one-tenth of a "bel" which is in turn a rarely-used unit.

If the power quantity P_2 is twice as P_1, the difference in dBs would be

$$10 * \log(\frac{P_2}{P_1}) = 10 * \log(2) = 3dB \tag{A.2}$$

If P_2 is the same as P_1, the difference in dBs would be

$$10 * \log(1) = 0dB \tag{A.3}$$

If P_2 is 10 times larger than P_1, the difference in dBs would be

$$10 * \log(10) = 10dB \tag{A.4}$$

Besides power, dBs can also describe current and voltage quantities.

Since $P \propto I^2, V^2$, then:

$$dB\ for\ current = 10 * \log(\frac{P_2}{P_1}) = 10 * \log(\frac{{I_2}^2}{{I_1}^2}) = 20 * \log(\frac{I_2}{I_1}) \tag{A.5}$$

$$dB\ for\ voltage = 10 * \log(\frac{P_2}{P_1}) = 10 * \log(\frac{{V_2}^2}{{V_1}^2}) = 20 * \log(\frac{V_2}{V_1}) \tag{A.6}$$

This can be seen for different values of power and current/voltage ratios as in table A.1 below, as well for different values of power ratios as shown in figure A.1.

dB	Power ratio	Current/Voltage ratio
100	10 000 000 000	100 000
90	1 000 000 000	31 620
80	100 000 000	10 000
70	10 000 000	3 162
60	1 000 000	1 000
50	100 000	316.2
40	10 000	100
30	1 000	31.62
20	100	10
10	10	3 .162
0	1	1
-10	0 .1	0 .316 2
-20	0 .01	0 .1
-30	0 .001	0 .031 62
-40	0 .000 1	0 .01
-50	0 .000 01	0 .003 162
-60	0 .000 001	0 .001
-70	0 .000 000 1	0 .000 316 2
-80	0 .000 000 01	0 .000 1
-90	0 .000 000 001	0 .000 031 62
-100	0 .000 000 000 1	0 .000 01

Table A.1: Power ratios and voltage/current amplitude ratios and their corresponding dBs

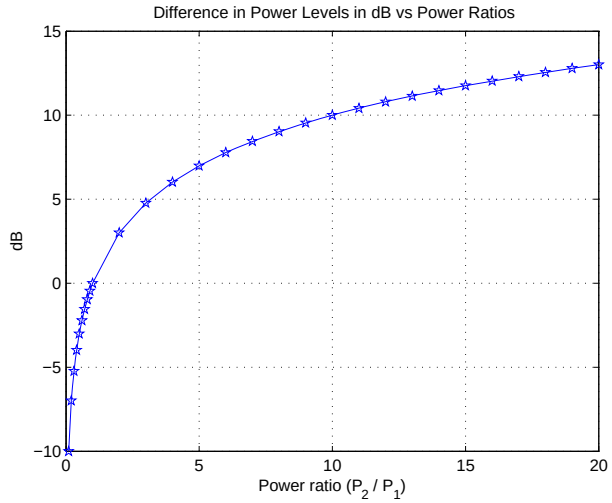

Figure A.1: Difference in power levels (dB) versus power ratios

dBs may also describe absolute quantities above or below a certain reference, which makes it necessary to know the reference value used. Examples for commonly used absolute quantities and their corresponding reference values are shown in table A.2 below

Unit Symbol	Unit Type	Reference Value
dB	Power	1 W
dBm	Power	1 mW
dBV	Voltage	1 V
dBmV	Voltage	1 mV
dBμV	Voltage	1 μV

Table A.2: dB units describing absolute quantities and their corresponding reference values

The advantage of using dBs can be summarized in the following points:

- dB plots are best in describing very large windows which yet contain small variations. As one can see from table A.1 above, a 1 volt signal and a 10

microvolt signal can be both represented on a plot with a range of 100 dBs.[34]

- dBs can represent very large or very small ratios in moderate size numbers. It is easier for the mind to compare 2-3 digit numbers than comparing up to 10 digit numbers.
- Gain and loss calculation is simpler with dBs; Power ratios expressed in dBs are simply additive. For example, if we have a system with a gain of 13 dBs (corresponding to a power ratio of 20 times) followed by another with a loss of 3 dBs (power ratio of $\frac{1}{2}$ times), the overall gain/loss would be simply 13+(-3) = 10 dBs which corresponds to a gain with a power ratio of 10.